VILNIUS UNIVERSITY
CENTER FOR PHYSICAL SCIENCES AND TECHNOLOGY

Dovilė
BAZIULYTĖ-PAULAVIČIENĖ

Lanthanide-doped upconversion inorganic materials: new insights as luminescent probes

DOCTORAL DISSERTATION

Natural sciences,
Chemistry N 003

VILNIUS 2019

This dissertation was carried out from 2014 to 2018 at Vilnius University.

The research was supported by Research Council of Lithuania (Grant No. MIP-030/2014, also scholarship to attend conference/internship) and EU Framework Programme “Horizon 2020”, COST action CM1403.

Academic supervisor – Prof. Dr. Simas Šakirzanovas (Vilnius University, Natural sciences, Chemistry – N 003).

VILNIAUS UNIVERSITETAS
FIZINIŲ IR TECHNOLOGIJOS MOKSLŲ CENTRAS

Dovilė
BAZIULYTĖ-PAULAVIČIENĖ

Lantanoidais legiruotos apkonvertuojančios neorganinės medžiagos: naujos liuminescencinių žymenų įžvalgos

DAKTARO DISERTACIJA

Gamtos mokslai,
Chemija N 003

VILNIUS 2019

Disertacija rengta 2014 – 2018 metais Vilniaus universitete.

Mokslinius tyrimus rėmė Lietuvos mokslo taryba (Projektas Nr. MIP-030/2014, taip pat parama mokslinėms išvykoms) ir ES bendroji mokslinių tyrimų ir inovacijų programa „Horizontas 2020“, COST CM-1403.

Mokslinis vadovas – prof. dr. Simas Šakirzanovas (Vilniaus universitetas, gamtos mokslai, chemija – N 003).

TABLE OF CONTENTS

LIST OF ABBREVIATIONS

BET	Back-energy transfer
CIE	Commission Internationale de l'Eclairage
CR	Cross-relaxation
CW	Continuous-wave
DCL	Down-conversion luminescence
DI	Deionized
ESA	Excited state absorption
ETU	Energy transfer upconversion
FIR	Fluorescence intensity ratio
FTIR	Fourier-transform infrared spectroscopy
GSA	Ground state absorption
JCPDS	Joint Committee on Powder Diffraction Standard
MPs	Microparticles
MRI	Magnetic resonance imaging
NIR	Near-infrared
NPs	Nanoparticles
OA	Oleic acid
ODE	1-octadecene
PAA	Poly acrylic acid
QDs	Quantum dots
QR	Quick response
RE	Rare earth
RGB	Red, green, and blue
SEM	Scanning electron microscopy
SI	Signal intensity
S_R	Relative temperature sensitivity
TEM	Transmission electron microscopy
UC	Upconversion
UCL	Upconversion luminescence
UCNPs	Upconverting nanoparticles
UV	Ultraviolet
XRD	Powder X-ray diffraction

Chapter 1. Introduction

During the past decade, lanthanide-doped upconverting nanoparticles (UCNPs) have been extensively investigated due to the advantages associated with their unique luminescent properties [1]. In general, these nanoparticles can convert near-infrared (NIR) excitation light into the ultraviolet (UV), visible and NIR emission light *via* a multiphoton process known as upconversion (UC) [2]. This non-linear optical process is commonly observed in lanthanide-doped inorganic materials [3]. The emission intensities and wavelengths of UCNPs are important performance characteristics, which offers a wide range of applications, including sensing, imaging, diagnostics and therapy, as well as photovoltaic, security and display technology [4]. Compared with traditional semiconductor quantum dots (QDs) or organic fluorophores, UCNPs show superior features such as sharp emission peaks, long emission lifetime, high chemical stability, high resistance to photobleaching and low toxicity [5]. Driven by these factors, UCNPs could serve as excellent candidates for numerous biomedical applications [6-8]. Followed by combination with biologically active molecules, UCNPs could be multifunctional in both therapy and diagnostics (theranostics) [9, 10].

Despite many promising advantages of UCNPs, a number of limitations still need to be addressed. First of all, the small size, rational design and appropriate co-doping strategy are typically required to construct high-efficient UCNPs for biomedical applications. One of the major methods to enhance the upconversion luminescence (UCL) intensity is to use a core–shell structure, where the non-active shell protects the luminescent rare earth (RE) ions in the core from quenching caused by surface defects and organic ligands [11]. At the same time, nanoscale lanthanide-doped upconversion materials with core-shell structure open up new avenues for the modulation of upconversion properties, e.g., through combining UC luminescence and magnetic resonance imaging (MRI) modalities into a single structure [12]. Another effective way to improve upconversion efficiency is increasing the amount of emitters, however, high doping concentration leads to increased occurrence of energy transfer process between the dopants, resulting in quenching of excitation energy [13]. Designing a core-shell structure, where high content of lanthanide ions is incorporated into the core and the inert shell blocks the way of energy migration to surface quenching sites, is a rational and convenient route to overcome these obstacles [14]. It can be concluded, that traditional synthesis methods hardly fulfil the growing requirements for

practical uses, revealing an emerging need for more complex fabrication approaches [15].

As a unique class of luminescent materials, UCNPs also show great promise in thermal sensing and security applications [16, 17]. The previous studies have shown that Er^{3+} ions suit well as an effective temperature sensing unit [18, 19]. One of the sensing techniques, fluorescence intensity ratio (FIR), involves monitoring of temperature-induced changes of specific thermally coupled energy level emission intensity ratios. Owing to its high spatial and thermal resolutions, wide measurement ranges and affordability, this non-contact technique is one of the most promising for temperature determination at the sub-micrometer and nanometer scale [20, 21]. Apart from the biomedical and thermal sensing application, the unique optical properties of lanthanide-doped upconversion materials have potential in security applications [22]. UCNPs have been suggested as the basis for the next generation of luminescent inks for anti-counterfeit labelling. Placing a printed area under a beam of NIR light, under specific excitation power densities or temperature, initiates the conversion of the covert inks into the correct colour rendering. Thus, a predetermined read condition becomes a security feature itself [4].

The main aim of this work was to synthesize multifunctional lanthanide-doped (Yb^{3+} and/or Er^{3+}) nano and micro size $NaGd(Yb)F_4$ particles and to investigate their optical properties, as well as to explore their potential use in various applications. The single ($NaGdF_4$) and double ($NaYbF_4$@$NaGdF_4$) shell coating was applied in order to tune and enhance the upconversion luminescence. In addition, the concentration of the activator (Er^{3+}) was optimized and the effect of the sensitizer and activator separation on the optical properties was also investigated. Furthermore, the thermochromic features of microparticles are presented. Finally, the temperature-sensing properties and cellular metabolic activities as well as the distribution of nanoparticles in human breast cancer cells were evaluated. The tasks of the present thesis were formulated as follows:

1. To synthesize lanthanide-doped upconversion nano- and microparticles, as well as to epitaxially grow a shell layer on as-prepared particles surface *via* thermal decomposition synthesis method.

2. To investigate the upconversion luminescence and decay dynamics properties of the obtained materials as well as to improve these features by growing single or double epitaxial shell layers.

3. To investigate the influence of separation of activator and sensitizer in different layers, as well as to determine the optimal activator concentration for optical properties.

4. To examine the temperature-sensing and thermochromic properties of nano- and micro-size particles

5. To evaluate the potential use of UCNPs for imaging and detection with focus on cancer diseases.

Chapter 2. Upconversion

2.1 The Phenomenon of Upconversion

Upconversion (UC) is a nonlinear optical process, where a sequential absorption of two or more low energy photons leads to the emission of photons with higher energy. The emission of light at a shorter wavelength than the excitation wavelength is also known as anti-Stokes photoluminescence. This general concept was first introduced by Francois Auzel and Nicolaas Bloembergen in the 1960s [23, 24]. Since then, the UC process has been extensively studied and widely applied in optical devices.

2.2 Upconversion Luminescence Mechanisms

The upconversion process proceeds by different mechanisms, however the two major mechanisms can be distinguished: excited state absorption (ESA), and energy transfer upconversion (ETU) (Figure 2.1 a, b). These processes are frequently accompanied by cross-relaxation (CR) (Figure 2.1 c). ESA and ETU mechanisms are based on the sequential absorption of two or more photons by metastable, long-lived energy states. This sequential absorption leads to the population of a higher excited state from which upconversion emission occurs.

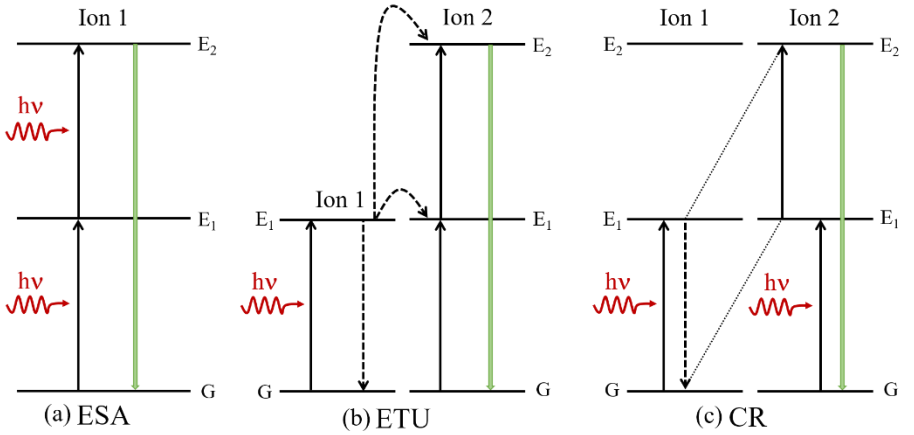

Figure 2.1 Schematic representation of the: (a) excited-state absorption (ESA), (b) energy transfer upconversion (ETU), and (c) cross relaxation (CR) process.

ESA is an upconversion process, in which the sequential absorption of two photons *via* a single ion occurs. As shown in the Figure 2.1 a, if an incoming photon is of a wavelength resonant with the energy gap separating ground and excited states, it will bring the ion to an intermediate excited level (E_1) from the ground state (G), which is known as the ground state absorption (GSA). Subsequently, second absorbed photon promotes this ion from E_1 level to the upper emitting level (E_2) and results in UC emission of a photon having higher energy than either of the photons absorbed. This is the least efficient upconversion mechanism [1, 25].

Energy transfer upconversion (ETU) mechanism can be derived from the ESA by including a second ion in the excitation stage (Figure 2.1 b). ETU process involves the successive energy transfer from ion 1 (sensitizer or donor) to second ion (activator or acceptor). Usually, the sensitizer has a large absorption cross-section in the NIR region. In this upconversion process, each of two neighbouring ions can absorb a pump photon of the same energy and populate to their intermediate states (E_1) *via* GSA. Then, a non-radiative energy transfer from ion 1 to the ion 2 results in the promotion of the latter to its upper emitting state (E_2), while the ion 1 relaxes back to ground state G. ETU is by far the most efficient upconversion process [1, 26].

Similar to ETU mechanism, the cross relaxation (CR) process involves energy transfer between two neighbouring ions in close proximity where one ion acts as a donor of energy (ion 1), while the second acts as an acceptor of energy (ion 2). In this upconversion process, two identical ions in close proximity are both excited from the ground state (G) to intermediate excited state (E_1) by GSA, then energy transfer occurs through a non-radiative process in which one ion returns to the ground state while another is promoted to the upper emitting level (E_2) (Figure 2.1 c). However, CR can also depopulate the excited state by partial energy transfer to a neighbouring ion. This directly quenches the excited states and shortens the decay time [27]. The CR process is a fundamental result of ion-ion interaction and its efficiency is in close relation with the dopant concentration [1, 9].

Crucial requirements for photon upconversion, such as long lifetimes of the excited states and a ladder-like arrangement of the energy levels with similar spacings, are met by certain ions of the *d* and *f* elements [2]. The most efficient photon UC process is demonstrated by the lanthanides [3].

2.3 Upconversion Process Efficiency and Quenching

One of the most important parameters in the upconversion process is upconversion efficiency, which is often referred to as an upconversion quantum yield. UC quantum yield is defined as the ratio of the number of emitted upconverted photons to the number of absorbed photons. This value will always be lower than 0.5 because the emission of one photon in the upconversion process requires the absorption of at least two photons [28]. However, the UC luminescence efficiency is attenuated by a few deleterious energy migration processes, including non-radiative decay, cross-relaxation, energy back-transfer and energy dissipation due to the high-energy vibrations of surface ligands [29, 30]. Any process that lowers the number of metastable excited states without giving off upconverted radiation is referred to as quenching. For example, phonons provide a competing energy transfer route to radiative emission through multi-phonon transitions to lower energy levels, and therefore ions with closely spaced energy levels are susceptible to quenching. Multiple phonons are required to bridge the same energy gap compared to a single photon in radiative process; therefore, the probability of phonon quenching decreases exponentially as the energy gap between levels increases. Quenching can also occur in case the sublevel exists between the excited state and the ground state, so emission may proceed in two steps rather than one. Another quenching mechanism occurs *via* cross-relaxation to impurities or other lanthanide ions in the material [31].

The optical efficiency of lanthanide-based upconversion is related to the choice of crystalline host lattice, nanoparticle size, as well as the concentrations of optically active dopants. Fischer *et al.* investigated six distinct alkaline-earth rare-earth fluoride host materials and benchmarked their upconversion quantum yield [32]. They found that the host material SrLuF is the most efficient, with UC quantum yield values of 0.53 % at 80 W/cm^2 excitation. Resch-Genger's group assessed the influence of dopant concentration on the quantum yield and their results showed that optimal sensitizer and activator concentration is 14 % and 1 %, respectively [33]. Furthermore, it was reported that the upconversion efficiency of UCNPs decreases significantly with decreasing nanoparticle diameter [34]. Interestingly, the upconversion efficiency of UCNPs with exactly the same size depends on the surface ligand coating and dispersion medium [35, 36]. These findings suggest that there are many factors that contribute to the low upconversion luminescence efficiency of UCNPs. The recent effort to boost

the upconversion luminescence efficiency comprises of introducing inert shells coating [37], high concentration of activators doping [38], organic dyes modification [39] and so on. Up to date, the maximum reached upconversion quantum yield is approximately 9 % for the 45 nm core−shell UCNPs [37], which approaches the quantum yield of micron-sized crystals with the same composition.

2.4 Upconversion Luminescence Decay Kinetics

Upconversion luminescence decay kinetics is an important aspect of its temporal characteristics. In contrast to QDs and organic dyes, lanthanide-doped upconversion materials demonstrate distinct photoluminescence lifetimes from microseconds to even milliseconds. The long-lived intermediate energy states in lanthanide ions can be attributed to the parity-forbidden nature of the 4*f*-4*f* transition, which results in low transition probabilities but these rules are relaxed by several mechanisms [40]. The interactions between sensitizer and activator, i.e. ETU, makes it to operate as an integral unit, leading to the complex luminescence kinetics of the individual nanoparticle [41, 42]. The upconversion luminescence profile, recorded after a short-pulsed NIR laser beam excitation, typically features a delayed rather than immediate time trace maximum, reflecting both rise and decay behaviour. Such luminescence kinetics can generally adequately fit the following equation [43]:

$$I(t) = A\left[exp\left(-\frac{t}{\tau_d}\right) - exp\left(-\frac{t}{\tau_r}\right)\right] \qquad \textit{(Eq. 2.1)}$$

where *I(t)* is the intensity of emission at time *t*, *A* is a scaling constant, τ_d and τ_r are the rise and decay time constants, which describe the time scales of the population and depopulation for corresponding energy levels, respectively. The function can be simplified to an exponential decay only:

$$I(t) = I_0 exp\left(-\frac{t}{\tau}\right) \qquad \textit{(Eq. 2.2)}$$

where I_0 is the intensity of emission at time $t = 0$, and τ is the mean lifetime of the emission. The decay lifetime (τ) is defined as the required time for transient emission intensity to decay from its maximum value to its 1/*e* value.

Usually, after the exponential fitting of the decay profile data, the decay time constant is extracted and interpreted as the intrinsic lifetime of the UC luminescence emitting state [42].

Recent studies showed that the luminescence lifetime is influenced by several factors, including particle shape and size, surface passivation and dopant concentration. Regarding the effect of particle shape, the aspect ratio of UCNPs has been demonstrated to affect the lifetimes, which has been attributed to anisotropic multi-phonon relaxation processes due to different ion-ion distances and lattice energies along different crystal planes within a single nanoparticle [44]. Further, it was reported that UCL lifetime of the excited states of lanthanide ions in nanostructures exhibit strong size-dependence [45, 46]. In addition to the effects of size and shape, Würth et al. investigated the surface passivation effects on ultra-small UCNPs and it was found that by variation of the shell thickness results in tuning the luminescence lifetimes [47]. Moreover, Dayong Jin group developed an approach to precisely tune the microsecond-to-millisecond luminescent decays and produce individual populations of rare-earth doped nanocrystals with distinct lifetimes by stepwise variation of lanthanide ions concentration in the UCNPs [48].

Upconversion luminescence dynamics has long been believed to be determined solely by the emitting ions and their interactions with neighbouring sensitizing ions. However, recent studies showed that the luminescence time behaviour in the nanomaterials is also affected by the migration processes of the excitation energy. Yet, for the most efficient UC mechanism – energy transfer upconversion (ETU) – the proper luminescence dynamics is still not well disentangled due to the complexity of interactions between multiple excited lanthanide ions [49]. It is important to analyse the luminescence decay profile as it can help to understand specific physical mechanisms responsible for non-radiative decay processes.

2.5 Design of Upconverting Materials

The development of highly efficient upconverting materials requires precise selection of appropriate host material, the dopant ions (usually lanthanide ions) and the dopant concentration. The ideal host material should be transparent in the spectral range of interest, have high optical damage threshold and be chemically stable, while the dopants suitability is defined by

its type and concentration, which determine the emission wavelengths and the efficiency of the upconversion process.

2.5.1 Host Matrices

Host matrices with low lattice phonon energies are required to minimize the non-radiative loss and maximize the radiative UC emission [50]. Various inorganic crystals, for example such as the oxides and phosphates, have been studied for use in upconversion; however, the associated phonon energies are usually quite high (usually >500–1000 cm^{-1}) [9], resulting in lower upconversion efficiencies due to the enhancement of non-radiative pathways. Although, heavy-halide hosts such as chlorides, bromides, and iodides normally exhibit low phonon energies (< 300 cm^{-1}), but their use is limited because their hygroscopic nature. Among investigated host materials, fluorides have been proven to be ideal host candidates for UC because of the low phonon energies (ca. 350 cm^{-1}) of the crystal lattice and relatively high chemical stability.

Trivalent lanthanide ions-based inorganic compounds are excellent host materials for upconversion materials because all trivalent lanthanide ions exhibit similar ionic size and chemical properties. In addition, host lattices based on cations such as Na^+, Ca^{2+}, Sr^{2+}, and Ba^{2+} with ionic radii close to those of the lanthanide dopant ions prevent the lattice mismatch and consequent lattice stress. Thus, the best host materials for upconversion are considered to be Na^+-, Ca^{2+}-, and Y^{3+}-based fluorides [1]. For example, the upconversion efficiency of $NaYF_4$:Yb^{3+},Er^{3+} compared to La_2O_3:Yb^{3+},Er^{3+} and $La_2(MoO_4)_3$:Yb^{3+},$Er^{3+}$is 20 and 6 times stronger, respectively [2].

Another important parameter for UC material choice is the crystallographic host symmetry. The local crystal symmetry surrounding a lanthanide ion influences its optical properties [9]. One of the most studied fluoride host material is $NaYF_4$ [51-54], which has two different crystal structures – hexagonal and cubic. As shown in Figure 2.2, the cubic structure (α-$NaREF_4$) creates a dopant environment with high symmetry, while the hexagonal structure (β-$NaREF_4$) consists of an ordered array of F^- ions with two types of relatively low-symmetry cation sites selectively occupied by Na^+ and RE^{3+} ions [18]. Low-symmetry hosts typically exert a less symmetrical crystal field around the dopant ion in the lattice matrix compared to high-symmetry counterparts. The phase-dependent optical properties can be ascribed directly to the low-symmetry enhanced electronic coupling between 4*f* energy levels,

which results in greater probability of *f-f* transition of the optically active dopants [1]. It was reported, that the UC efficiency of the green emission in hexagonal-phase $NaYF_4$:Yb^{3+}/Er^{3+} is approximately one order of magnitude stronger than that in cubic $NaYF_4$:Yb^{3+}/Er^{3+} [55].

Selection of an appropriate host lattice with a low phonon energy, less symmetrical crystal structure and small lattice mismatch for the dopant ions is therefore essential for development of an efficient UC process.

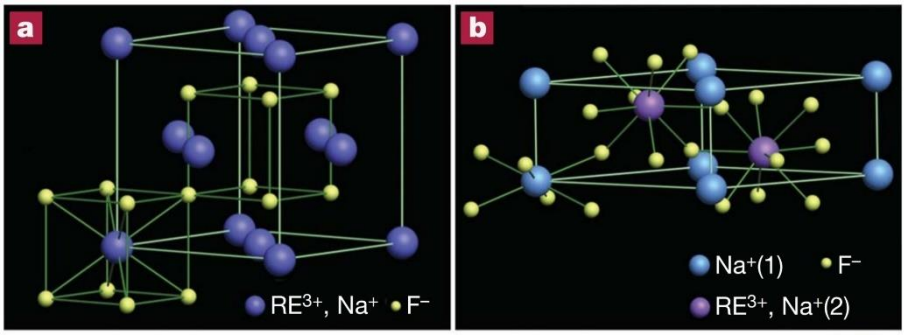

Figure 2.2 Schematic representation of (a) cubic and (b) hexagonal phase $NaREF_4$ structures (RE - rare earth ions). In the cubic phase, fluorite structure are formed, with the cation sites randomly occupied by either Na^+ or RE^{3+} ions. In the hexagonal phase, an ordered array of F^- ions contains two types of cation sites: one occupied by Na^+ and the other occupied randomly by RE^{3+} or Na^+ [18].

2.5.2 Dopant Selection Criteria

The dopant ions are usually present in the form of localized luminescence centres. In the case of the energy transfer upconversion, the dopant ion radiates upon its excitation to a higher energetic state obtained from the non-radiative transfer of the energy from another dopant ion (see section *2.2 Upconversion Luminescence Mechanisms*). The ion that emits the radiation is called an *activator*, while the donor of the energy is the *sensitizer*. Although UC can in principle be expected from most lanthanide-doped crystalline host materials, efficient UC only occurs in a small number of well selected dopant–host combinations [25]. The main requirements for efficient photon upconversion are: the long lifetimes of the excited states and a ladder-like arrangement of the energy levels with similar energy spacings [2].

Almost all the trivalent lanthanides fulfil these requirements when the appropriate excitation energy is applied. The lanthanides, which are associated with the filling of the 4*f*-shell, commence with the element lanthanum (La) and end with the element lutetium (Lu). They essentially exist in their most stable oxidation state as trivalent ions (Ln^{3+}). The shielding of the 4*f* electrons in Ln^{3+} by the completely filled $5s^2$ and $5p^6$ sub-shells results in weak electron–phonon coupling that is responsible for important phenomena such as sharp and narrow *f*–*f* transition bands. In addition, the *f*–*f* transitions are Laporte forbidden, resulting in low transition probabilities and substantially long-lived (up to 0.1 s) excited states. With the exception of La^{3+}, Ce^{3+}, Yb^{3+}, and Lu^{3+}, the lanthanide ions commonly have more than one excited 4*f* energy level [1, 25], and a large number of close energy levels, which can therefore facilitate multiple types of upconversion processes. The energy states of Ln^{3+} ions are specified in terms of the orbital (*L*), total angular momentum (*J*) and spin (*S*) of each of their *f* electrons, and denoted in the Russell–Saunders notation as $^{2S+1}L_J$ [56]. The energy level structure of lanthanide ions is usually called a *Dieke* chart (or *Dieke* diagram) which is presented in Figure 2.3.

2.5.3 Activators

The luminescent centre in the upconverting material, which emits the output photon, is called the activator. Er^{3+}, Tm^{3+}, and Ho^{3+} typically feature desirable ladder-like arranged energy levels and are thus frequently used activators. The upconversion efficiency of Er^{3+} is particularly high due to the similar energy gap in different energy levels (Figure 2.3). For example, the energy difference in Er^{3+} (~10 350 cm^{-1}) between the $^4I_{11/2}$ and $^4I_{15/2}$ levels is similar to that (~10 370 cm^{-1}) between the $^4F_{7/2}$ and $^4I_{11/2}$ levels. Thus, the energy levels of $^4I_{15/2}$, $^4I_{11/2}$, and $^4F_{7/2}$ can be used to generate UC emission using ~970 nm laser excitation. Instead of being directly excited to the $^4F_{7/2}$ state, Er^{3+} ion in the $^4I_{11/2}$ state can relax to the $^4I_{13/2}$ state, followed by excitation to the $^4F_{7/2}$ state with phonon-assisted energy transfer [1, 2, 25].

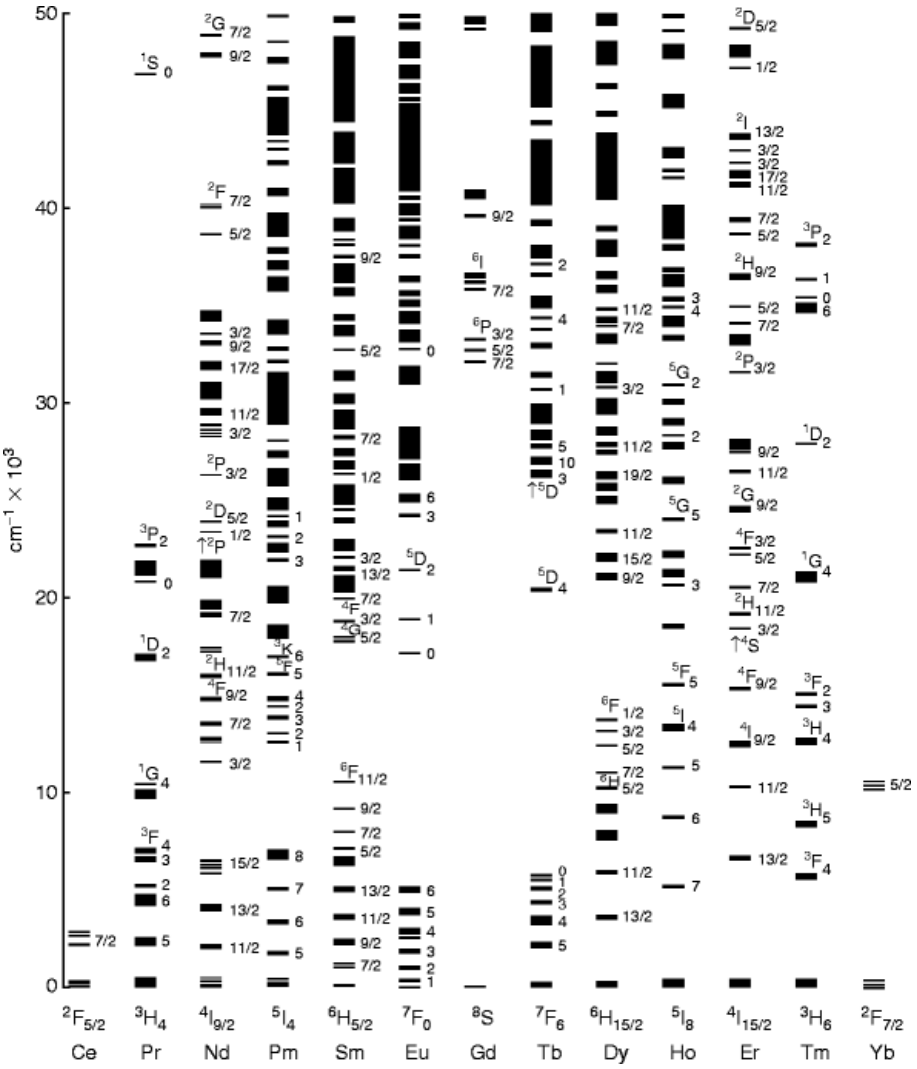

Figure 2.3 The lower 4*f* levels of trivalent lanthanide ions in a $LaCl_3$ crystal [57].

Since 4*f*–4*f* transitions are Laporte-forbidden, inefficient absorption of the exciting light can be an obstacle for efficient UC emission. Generally, the absorption can be improved by increasing the concentration of the lanthanide dopant in the material. However, non-radiative multi-phonon relaxation can occur, and the process of cross-relaxation severely limits the range of efficient dopant concentrations [1, 2]. The upper limit of concentration depends on the exact distance between the lattice sites occupied by lanthanide ions, but in

most upconversion materials the concentration of Er^{3+} does not exceed 3% [2, 58]. However, new studies showed that growing a *core-shell* structure while using high content of lanthanide ions could help to overcome above-mentioned obstacles and result in improved UC luminescence intensity, but these findings will be discussed in *chapter 3.3 Core-shell Concept*.

2.5.4 Sensitizers

The co-doping with another lanthanide, a so-called sensitizer, can greatly enhance the upconversion efficiency. According to ETU mechanism (see section *2.2. Upconversion Luminescence Mechanisms*), the ideal sensitizers should possess relatively large absorption cross-section and energy levels matching with those of activators. The most widely used sensitizer for Er^{3+} is the Yb^{3+} ion. Yb^{3+} possesses an extremely simple energy level scheme with only one excited 4*f* level of $^2F_{5/2}$ (Figures 2.3 and 2.4). As shown in Figure 2.4, the energy separation of the $^2F_{7/2}$ ground state of Yb^{3+} and its $^2F_{5/2}$ excited state matches well the transition energy between the $^4I_{11/2}$ and $^4I_{15/2}$ and the $^4F_{7/2}$ and $^4I_{11/2}$ states of Er^{3+} [1]. This feature allows a highly efficient energy transfer to the activator and thus greatly strengthens the probability of the ETU process. Abovementioned optical characteristics make Yb^{3+} particularly suitable for use as a sensitizer for upconversion, thus, in this thesis the Yb^{3+} and Er^{3+} co-doping system is adopted.

In contrast to activator, the concentration of the sensitizer can be higher (18–20 mol%). Intriguing, new studies showed that heavily doped with Yb^{3+} (even up to 100 %) materials results in both overall and red UC luminescence intensity increase and might be the cause of recently introduced effect of negative thermal quenching [59]. Higher concentrations of Yb^{3+} increase absorption cross-section per nanoparticle and enhance energy transfer rates between Yb^{3+} and Er^{3+} ions [60]. On the over hand, high Yb^{3+} content could decrease the Yb···Yb interatomic distance, and thus, facilitating energy hopping in the Yb^{3+} sub-lattice and excitation energy would be transferred from interior to the peripheral region of the nanoparticle, leading to an enhanced surface-quenching effect [61]. Again, these obstacles could be eliminated by growing a passivation layer and will be discussed in details in *chapter 3.3 Core-shell Concept.*

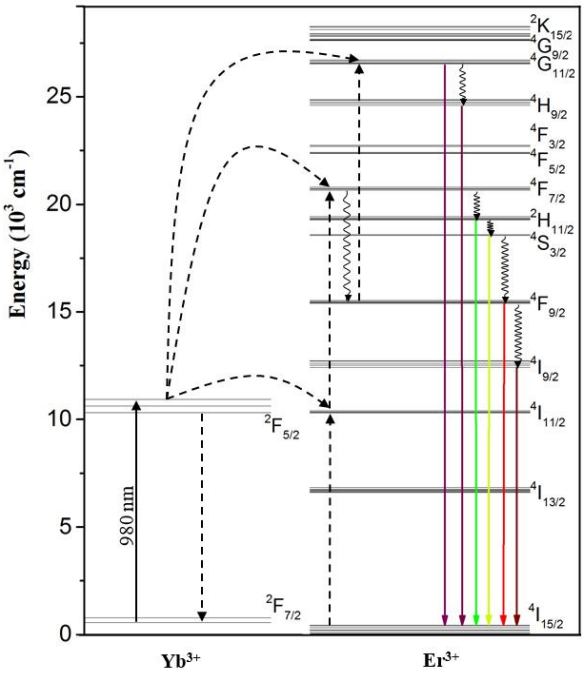

Figure 2.4 The energy level diagram of Yb^{3+} and Er^{3+} ions.

Chapter 3. Lanthanide-doped Upconversion Nanomaterials

The research in the field of photon upconversion has been devoted almost exclusively to bulk materials in form of films, glasses or fibers. Its application was the main focus of investigation especially in regard of optical devices including infrared quantum counter detectors, temperature sensors, and compact solid state lasers [25]. From the late 1990s, when nanoparticles research became prevalent, the UC became more prominent in the fields of biological assays and medical imaging [62]. Compared with conventional luminescent markers (organic dye molecules, QDs , and dye-doped silica/gold nanomaterials), which are excited in the ultraviolet (UV) or visible light, excitation in the near-infrared (i.e. 808 or 980 nm) has the great advantages such as low photodamage to biological specimens, high resistance to photobleaching, and low auto-fluorescence [5]. These advantages prompted the development of a new type of high-quality and well-shaped nanomaterials known as upconversion nanoparticles (UCNPs). Nanoscale manipulation of UCNPs also leads to important modification of their optical

properties in excited-state dynamics, emission profiles and UC efficiency. For example, the reduction in particle size provides the ability to modify the lifetime of intermediate states of the doped rare earth ions. The control of spatial confinement of dopant ions within a nanoscopic region can lead to remarkable enhancement of a particular wavelength emission as well as generation of new types of emissions [25].

Thereafter, finally an urge for the development of efficient synthesis routes to obtain upconverting materials in the micro- or nano- meter range emerged. During the past decade, several methods including co-precipitation [63], thermal decomposition [53], hydrothermal [64] and microwave [65] have been developed to synthesize these materials. The material characteristics including size, monodispersity, shape, surface functionality, or phase modification strongly depend on the type of synthesis and its conditions. Among all these methods, the thermal decomposition synthesis route (see *chapter below 3.1 Thermal Decomposition Synthesis Method*), which is carried out in high-boiling organic solvents, is most successful and widely used one.

After the synthesis, the lanthanide-doped upconversion nanoparticles usually possess a hydrophobic surface, thus subsequent modification step is required to create a hydrophilic surface for bioanalysis. Several methods including surface silanization [66], ligand exchange [67], ligand oxidation [68], ligand removal [69], and amphiphilic polymer coating [70] have been developed in order to transfer nanoparticles with hydrophobic surfaces into aqueous media. Water soluble UCNPs were widely applied for determination of biocompatibility, bioimaging and therapy [71, 72].

3.1 Thermal Decomposition Synthesis Method

Thermal decomposition method was first used for synthesis of highly monodisperse LaF_3 nanoplates in 2005 [73]. This approach was later modified and extended as a common route to the synthesis of high quality UC $NaYF_4$ nanoparticles [53]. The conventional thermal decomposition method involves the decomposition of trifluoroacetate precursors in high boiling point organic solvents in the presence of long alkyl chain surfactants. The mixture of solvents is composed of both the coordinating solvent and non-coordinating solvent. 1-octadecene (ODE) with a high boiling point (315 °C) is used as the non-coordinating solvent which provides medium for a high temperature synthesis. Oleic acid (OA) acts as the coordinating solvent which caps the

surface of NPs to prevent agglomeration [50, 74]. Although, the process is suitable for high quality UCNPs synthesis, it is not environmentally friendly as the use of metal trifluoroacetates produces fluorinated and oxy-fluorinated carbon species which are considered to be toxic [50]. Chen *et. al.* reported a non-toxic thermal decomposition method for the preparation of $NaYF_4$ and $NaGdF_4$ nanoparticles by using lanthanoid-oleate complex and NaF as the precursors [75, 76]. Another synthesis modification was introduced, where methanol solutions of NH_4F and NaOH is added to the homogeneous solution of rare earth chlorides, OA and ODE [77-79]. Advantages of the thermal decomposition synthesis includes narrow particle size distribution, high luminescence efficiency and high phase purity of the obtained particles [2]. In this thesis, based on the above-mentioned features, thermal decomposition method was chosen for the synthesis of UCNPs.

3.2 Control of Size, Phase and Morphology

Size, phase and morphology of UCNPs are the major concerns in many applications. For example, the biomedical application requires material to be in the range of 4-30 nm, in order to trace biological activity on the subcellular level. Yan *et. al.* reported that nanocrystal phase, shape, and size can be manipulated by tuning the reaction time, the ratio of Na/RE and solvent composition in OA/oleylamine/ODE [80]. Another group determined that, Na^+ promotes the transformation from α-$NaGdF_4$ into β-$NaGdF_4$ and the reaction temperature plays a key role in the morphology evolution process of self-assembled nanoparticles [81]. Besides crystal phase and morphology, the monodispersity and precisely controllable size are another important factors. Johnson *et al.* showed that ultra-small (less than 10 nm), monodisperse $NaGdF_4$ NPs can be obtained by optimizing the reaction parameters associated with both nucleation and growth phases. In their study, the nucleation was controlled by the concentration of the coordinating ligand (i.e., oleic acid), while the growth phase was tuned by the reaction time and temperature [82].

3.3 Core-shell Concept

The nanoscale size of the upconversion luminescence particles is favoured in many applications, however, nanoparticles have lower luminescence efficiency compared to of the corresponding bulk materials, owing to the large surface-to-volume ratio of nanoparticles [2]. In the case of lanthanide-doped

upconversion materials, the presence of surface defects and solvent interactions with the surface of UCNPs can lead to quenching of the excited lanthanide states by enhanced multi-phonon relaxation processes. The design of core–shell structures can minimize the surface quenching effects and thus strongly enhances the luminescence intensity. Growing a shell on the surface of the nanoparticles both increases the distance between lanthanide ions and surface ligands of high vibrational states as well as reduces the non-radiative energy transfer of the dopants from the core to the nanoparticle surface (Fig 3.1). It should be kept in mind, that the luminescence or upconversion efficiency is significantly increased only if the interface between the particle core and the shell is of high quality, that is, if the interface contains a much smaller number of quenching sites than the surface of the core particle before coating. In such core-shell structures, the dopants are confined in the interior core of the nanocrystals. The shell can effectively suppress energy loss on the crystal surface, leading to enhanced luminescence efficiency [1, 11, 15].

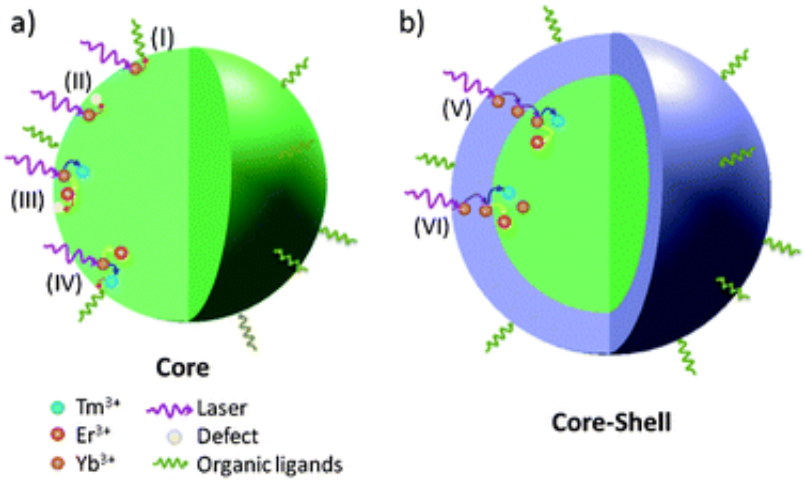

Figure 3.1 Schematic illustration of (a) possible energy losses in core only lanthanide-doped nanoparticles and (b) the proposed core–shell structure design for improving UC emission. Processes (I)–(IV) in (a) stand for the excitation energy losses due to organic ligands (I), defect (II), and the UC luminescence quenching by defects (III) and organic ligands (IV), respectively; (V) and (VI) in (b) show the typical energy transfer pathways from the shell to the core [83].

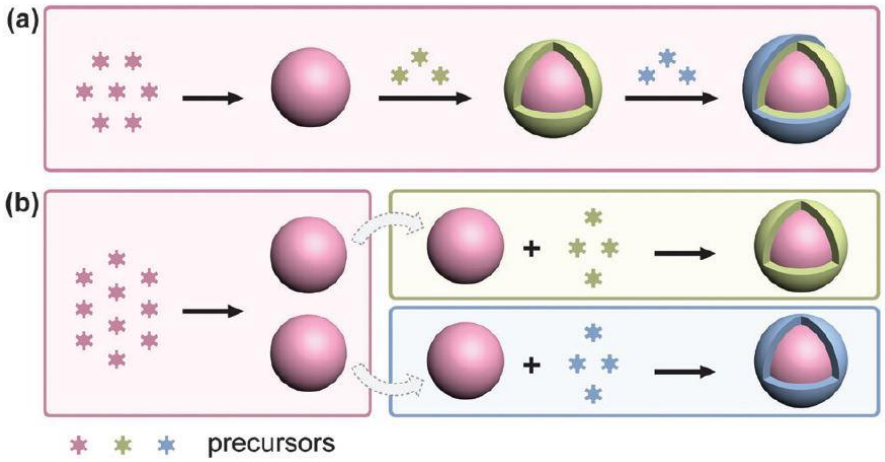

Figure 3.2 Main strategies for core-shell nanoparticles fabrication: (a) synthesis of multi-shelled nanoparticles through serial hot-injections of diverse shell precursors; (b) facile tuning of the shell composition through a parallel heat-up of pre-synthesized core nanoparticles with varying shell precursors [11].

The first demonstration of the core-shell structured UCNPs was reported by Lezhnina *et al.* in 2005 [84]. Since then, several strategies have been adopted to construct UCNPs with core-shell structures, for example, hot-injection (one pot successive layer-by-layer), and heat-up strategies (Fig. 3.2). In the case of hot-injection procedure, the epitaxial deposition of shell layers is achieved by injecting shell precursors into a proceeding reaction, thus this strategy allows the one-pot synthesis of multi-shelled nanostructures (Fig 3.2 a) [11]. The shell thickness and morphology can be precisely controlled by changing the injection rate and tuning the amounts of shell precursors [85, 86]. However, only small amounts of samples from different steps could be obtained. The heat-up method is one of the most widely used approaches to prepare high quality core-shell UCNPs with a relatively uniform morphology and size. Contrary to hot-injection strategy, in heat-up procedure the core of UCNPs must be obtained first and is subsequently utilized as seed nuclei for the epitaxial growth of the outer shell layer (Fig 3.2 b). The concentration of shell precursor needs to be low in regard to the concentration of the core of UCNPs to prevent the homogeneous nucleation of the shell host material alone rather than formation of the core-shell UCNPs [15]. Zhang *et al.* demonstrated

that the shell thickness can be precisely controlled by adjusting the molar ratio of core to shell precursor [87]. Several groups showed that the size and morphology of core-shell structures are also affected by the heating rate, reaction temperature, time and precursor concentration [88-91]. This method was chosen for current work on the basis of the listed advantages as well as the fact that the pre-synthesized core nanoparticles can be used as a standard starting material for fabrication of high-quality epitaxial core–shell structures.

It was reported that continuous shell growth gradually increases the UC emission intensity and decay lifetimes [87]. The core–shell structure is also used to elucidate the surface quenching effect associated with the size-dependent luminescence of NPs, as presented in Wang *et al.* work [89]. In this study, they showed that the inert thin-shell coating preserves the optical integrity of the nanoparticles and significantly minimizes surface quenching-induced emission losses. Several other reports claimed considerably different enhancement factors ranging from several to hundreds of folds, which depends on core particle size and composition as well as the excitation power density involved in different studies [92, 93].

The most effective way to improve upconversion efficiency is by increasing the number of emitters, however, high-doping concentration leads to increased occurrence of energy transfer process between the dopants, resulting in quenching of excitation energy, known as concentration quenching [58]. Moreover, the high-doping concentration facilitates the energy migration of excited levels to the surface quenchers as well as the inter-dopant cross-relaxation that causes emission intensity losses [14]. Recently, great efforts have been made to overcome concentration quenching in heavily-doped luminescent nanoparticles by using core-shell structure. For example, Johnson *et al.* showed, that after an inert epitaxial shell growth, erbium (Er^{3+}) concentrations as high as 100 mol% in $NaY(Er)F_4@NaLuF_4$ core-shell nanocrystals enhanced the emission intensity (Fig 3.3 a), with negligible concentration quenching effect [13]. Aside from high-doping concentration of activator ion, it is engaging to further increase Yb^{3+} concentration to enlarge absorption capability as well as UC luminescence intensity. Several groups have showed that heavy doping with Yb^{3+} ions can dramatically enhance the upconversion emission in the presence of an inert shell coating, (Fig 3.3 b) [94-97]. Furthermore, Qui *et al.* reported a significant enhancement of UC luminescence (~240 times) in α-$NaYF_4$:Yb^{3+},Tm^{3+}@$NaYbF_4$@$NaYF_4$ active core–active shell–inert shell nanoparticles, attributed to the directed energy migration in the second shell layer [98]. Their investigation showed that the

significant UC enhancement in UCNPs arises from directed energy transfer from the Yb^{3+} ions-contained in the active-shell to the dopant ions in the core and the outer inert shell blocks the way of energy migration to surface quenching sites.

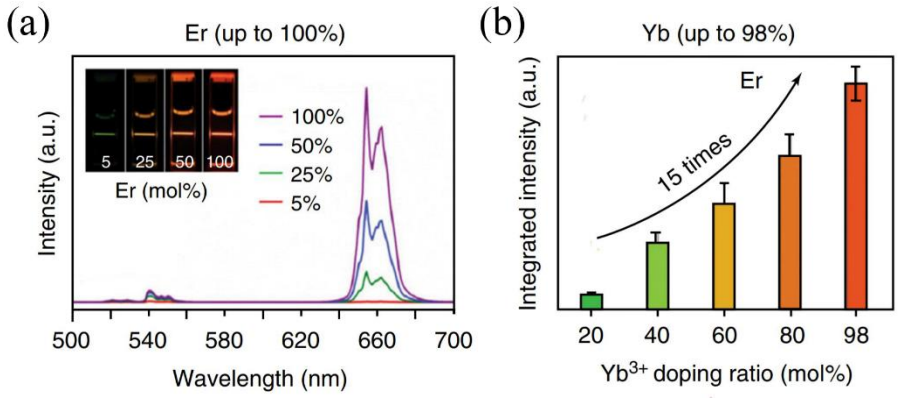

Figure 3.3 Upconversion luminescence enhancement in heavily-doped core-shell UCNPs: (a) Luminescence spectra of colloidal dispersion of $NaYF_4$:x%Er@$NaLuF_4$ NPs (x = 5, 25, 50, 100); Inset: luminescence images of $NaYF_4$:x%Er@$NaLuF_4$ in cyclohexane excited with a 980 nm laser [13]; (b) Integrated upconversion luminescence intensity of α-$NaY_{0.98-x}Yb_xF_4$:2%Er@CaF_2 (x = 0.2, 0.4, 0.6, 0.8, 0.98) core-shell NPs [97].

In addition to luminescent lanthanide ions, ionic dopants exhibiting various functionalities can be simultaneously included in the core–shell nanostructures. This offers the possibility to bring together multimodal imaging capabilities into a single nanoplatform, which provides rapid and precise monitoring of biological activity. For example, dual-functional probes for magnetic resonance imaging (MRI) and upconversion luminescence (UCL) microscopy were obtained through incorporating Gd^{3+} ions, which display outstanding magnetic properties [11]. Several groups showed that the Gd^{3+} ions containing core–shell UCNPs ($NaYF_4$:Yb,Er@$NaGdF_4$ [99], $NaYF_4$:Yb,Tm@$NaGdF_4$ [100], and $NaYbF_4$:Tm@$NaGdF_4$ [101]) exhibits both T_1 MR relaxivity and UC luminescence.

The core–shell design of UCNPs offers a facile way to decently engineer the distribution of lanthanide ions spatially, thus providing unprecedented opportunities to manipulate the electronic excitation, energy transfer and upconverted emissions. Moreover, it provides a convenient platform for

integrating multiple functionalities that offer new opportunities for various applications [11, 15, 102]. All in all, the core-shell concept has proven to be a powerful method to enhance the luminescence intensity and overcome the concentration quenching effect in lanthanide doped upconversion luminescence nanomaterials.

Chapter 4. Upconversion Material Applications

The development of a new type of high-quality and well-shaped upconversion nano- and micro- particles has enabled many promising applications ranging from security and anti-counterfeiting [16, 22, 103], 3D display [104, 105], solar cells [74, 106], drug release and gene delivery [107], molecular and thermal sensing [108-110], bioimaging [111-113], to therapeutics [10, 114]. This thesis focuses on the use of lanthanide-doped materials in thermal sensing, biological and security applications.

4.1 Thermal Sensing

During the last several centuries, the technological advancement has prompted thermometry to evolve from contact to non-contact. With the development of nanotechnology, it becomes possible to use nanothermometry to detect the temperature within a single cell. Upconversion lanthanide-doped materials are one of the most promising candidates for development of non-contact nanothermometry [1, 115-118]. The unique aspect of these materials is that their narrow luminescent emission bands are highly responsive to temperature changes, thus enabling temperature monitoring.

Optical temperature sensing based on the fluorescence intensity ratio technique (FIR) has received considerable attention in the past decades since it allows non-contact thermal reading with a great resolution. The main advantage of FIR technique is the fact that one single emission spectrum contains all the information needed to compute the absolute temperature. The FIR is based on a Boltzmann distribution of electrons between adjacent emitting energy levels that is a function of temperature and is manifested as a temperature-dependent intensity ratio between emissions from two distinct lines in the spectrum [20, 119, 120]. One of the conventional dopant ions in lanthanide-based thermometers is Er^{3+}, which possess relatively narrow (~780 cm^{-1}) energy gap between the $^2H_{11/2}$ and $^4S_{3/2}$ levels, where the lower energy $^4S_{3/2}$ state easily thermally populates the higher $^2H_{11/2}$ state [121, 122].

Consequently, Er^{3+}-activated luminescent materials have been used as probes for thermometry applications [19, 110, 123-125]. For example, Vetrone *et al.* measured the internal temperature in *HeLa* cancer cells from 25 °C to its thermally induced apoptosis at 45 °C using $NaYF_4:Yb^{3+},Er^{3+}$ UCNPs [110]. In addition, Wolfbeis *et al*. systematically investigated the ratiometric temperature response of core-shell UCNPs and found that these NPs have the ability to resolve temperature differences of less than 0.5 °C in the physiological temperature range [126]. In order to evaluate the thermometer's performance, among different samples and thermometers it is well agreed to compare their relative thermal sensitivity (S_R) values. Skripka *et al.* presented multi-layered UCNPs operating in aqueous media as NIR-to-NIR nanothermometers with relative thermal sensitivity around 1.1% $°C^{-1}$ [118]. Recently, Brites *et al.* reported self-calibrated double luminescent thermometers, which show a maximum relative sensitivity of 2.96% K^{-1} with a minimum temperature uncertainty of 0.07 K [127]. Hence, the current thermometer design based on lanthanide UCNPs has shown high thermal sensitivity.

4.2 Biomedical Applications

Over the past decade, tremendous progress in research on lanthanide-doped upconversion nanoparticles has been made, particularly in the field of biomedical applications, such as imaging, sensing and cancer therapy. Their outstanding merits, such as multicolour emission capability under single-wavelength excitation (i.e. NIR), high signal-to-noise ratio, low cytotoxicity, and high chemical- and photo-stability are unquestionable [4]. Furthermore, NIR excitation matches the biological transparency window (700–1870 nm) and sets the basis for deeper penetration depth into biological tissues due to less absorption, higher resolution as a result of reduced scattering, and improved imaging contrast due to tissue autofluorescence minimization [6].

Biomedical imaging, which plays a highly significant role in cancer diagnostics, is a technique where ultrasound, X-rays, electromagnetic fields, etc. is used to interact with human tissues and organs, consequently capturing specific signals and then converting them to detectable signals. After they are imported to a computer, the structure and density of the tissues and organs is visualized in an imaging mode, thereby providing diagnostic information. In recent decades, a number of imaging techniques have been invented and used in clinical diagnostics, such as magnetic resonance imaging (MRI), computed

tomography (CT), positron emission tomography (PET) and fluorescence imaging [128]. Among these techniques, the fluorescence, especially NIR fluorescence, imaging has attracted extensive attention in biomedical studies for both *in vitro* and *in vivo* imaging due to its low cost, quick feedback, high sensitivity and non-hazardous radiation [8, 129, 130]. More recently, UCNPs have gained widespread attention and showed huge potential in NIR optical imaging [7]. The possibility of using UCNPs as *in vivo* NIR contrast agents was first demonstrated by Prasad's group, where they monitored the biodistribution of NPs after intravenous injection into mice [131]. After these early demonstrations of UCNPs as *in vivo* contrast agents, they have been used as fluorescent probes in multiple biomedical applications [132-134].

To combine the merits of UCNPs bioimaging modalities, multimodal imaging has been developed and utilized as nanoprobes for *in vitro* and *in vivo* dual-modal luminescence imaging and MRI. Gd^{3+} ion-based materials are promising for use as MRI contrast agents due to seven unpaired inner 4*f* electrons, which can efficiently change the spin–lattice relaxation of the protons of coordinated and/or nearby water for T1-weighted MRI imaging [9]. A large variety of UCNPs on the basis of Gd^{3+}-doped nanoprobes have been reported and used for *in vitro* and *in vivo* dual modal UCL/MRI imaging [135-137]. Apart from dual-modality, UCNPs could also be used as a flexible multimodal platform. Sun *et al.* presented a lanthanide-doped core–shell nanocomposite with radioactive, magnetic, X-ray attenuation, and UCL properties, which they applied in four-modality bioimaging of CT, MRI, SPECT, and UCL imaging *in vivo* [138].

The potential toxicity and biocompatibility of UCNPs are of a great importance for their biomedical applications. Similar to many other inorganic nanocrystals, UCNPs should not easily degrade in biological environment. Thus, understanding the behaviours of UCNPs in biological systems as well as their toxicological profiles is a critical fundamental question to be addressed in order to use this class of nanomaterials in medical applications in the future [1]. To date the majority of the data on UCNPs toxicity has been obtained with reference to *in vitro* cytotoxic activity [139, 140] and long-term *in vivo* toxicity studies [141-143]. It was reported that after incubation with UCNPs for at least 24 h, the cellular viabilities were estimated to be generally greater than 90% at high doses, signifying the low cytotoxicity of UCNPs [141]. Biodistribution of UCNPs conjugated with folic acid (FA) was tested by Xiong *et al.*, and their study showed that the NPs accumulated mostly in cancer cells as FA guided the UCNPs to FA receptors on the cancer cell

surface [144]. Although the presented results appear to be comprehensive and reliable in assessing the toxicity of UCNPs, however much more complex studies of their potential toxic activities should be carried out.

4.3 Security Applications

Apart from the thermal sensing and biomedical application, the unique optical properties of lanthanide-doped upconversion materials possess relevant features to be used in security applications. Yet, counterfeiters are increasingly successful in mimicking security features based on down-conversion photoluminescent materials. In response, UCNPs, for which long-wavelength excitation produces short-wavelength emission, have been suggested as the basis for the next generation of anti-counterfeiting luminescent inks [1].

Directing a beam of NIR light to the printed area converts the covert inks into a visible pattern [4]. UCNPs and appropriate NIR excitation sources are more difficult to duplicate than standard fluorescent dyes and UV sources. Moreover, the UCNPs can be formulated to produce the correct colour rendering only under specific excitation power densities or temperature, such that a predetermined read condition becomes a security feature itself [1]. Kellar *et al*.[145] presented a work on security printing using UCNPs ink, where high level of security was achieved by printing both green and blue upconverting inks into a single quick response (QR) code. Later, the same group demonstrated an RGB (red, green, and blue) additive colour printing system that produced highly resolved predefined patterns that were invisible under ambient lighting, but viewable as luminescent multi-colour images under NIR excitation. The development of an RGB UC printing system paved the way for an entirely new arena in security printing [22].

The use of UCNPs as anti-counterfeiting markers utilizes the advantages of UCNPs, such as NIR irradiation, invisibility in ambient light, high stability, as well as lack in background scattering [1]. Zang *et al.* reported synthesis method for multicolour-banded UC crystals in gram quantity by varying the composition of the activators, which allows multicolour barcoding for anti-counterfeiting through a single particle [146].

This printing scheme adds another level of security, providing an innovative means for data protection and identification [4]. The multi-colour property of UCNPs is a huge advantage among other anti-counterfeit materials.

Chapter 5. Experimental Part

5.1 Materials

All of the chemicals used in experiments were of analytical grade and used without further purification. Ln oxides (Gd_2O_3, 99.99%, Yb_2O_3, 99.99%, Er_2O_3, 99.99%) were obtained from Treibacher Industries AG (Germany). Oleic acid (OA, 90%) was purchased from Fisher Scientific and 1-octadecene (ODE, 90%) was obtained from Sigma-Aldrich. TWEEN 80 (Polysorbate 80) was purchased from Merck Millipore. Poly(acrylic acid) (PAA, 50 wt% solution in water, M.W. 5000) was purchased from Acros Organics. Other chemicals including hydrochloric acid, sodium hydroxide, ammonium fluoride, methanol, chloroform, ethanol, cyclohexane and acetone were obtained from Reachem Slovakia.

5.2 Synthesis Methods

5.2.1 Synthesis of Hexagonal Phase Core UCNPs

The synthesis of β-$NaGd_{0.8}F_4$:$Yb_{0.18}Er_{0.02}$ and β-$NaGd_{1-x}F_4$:Er_x (x=0.01, 0.03, 0.05 and 0.10 mol%) NPs was developed via a modified literature procedure [147]. Metal chloride precursors were prepared by dissolving 0.80-0.98 mmol Gd_2O_3, (0.18 mmol Yb_2O_3 in the case of β-$NaGd_{0.8}F_4$:$Yb_{0.18}Er_{0.02}$ synthesis) and 0.01–0.10 mmol Er_2O_3 in hydrochloric acid (HCl) and distilled water solution at elevated temperature (~80 °C) until the solution became clear, followed by evaporation and drying at 60 °C overnight. Metal chlorides powder were mixed with 12 mL oleic acid (OA) and 30 mL 1-octadecene (ODE) in three-neck round-bottom flask, then heated to 150 °C for 40 min. under argon atmosphere to form a homogeneous solution and then cooled to room temperature. Thereafter, 10 mL of methanol solution containing NaOH (5 mmol) and NH_4F (8 mmol) was then added and the solution was stirred at 50 °C for 30 min. Further, the temperature was increased to 100 °C and methanol slowly evaporated under vacuum. Then, the solution was heated to 300 °C for 1 h under argon atmosphere and left to cool down to room temperature. The resultant nanoparticles were precipitated by hexane/acetone (1:4 v/v), collected by centrifugation, washed with acetone, ethanol and DI water several times, and finally redispersed in cyclohexane. Synthesis scheme and experimental setup is presented in Fig. 5.1.

5.2.2 Synthesis of Core-shell and Core-shell-shell Nanoparticles

The subsequent deposition of the $NaYbF_4$ and/or $NaGdF_4$ shells followed a similar process for the preparation of core NPs. Metal chloride precursors were prepared by dissolving 0.5 mmol Yb_2O_3 (Gd_2O_3 in the case of $NaGdF_4$ shell deposition) was dissolved in HCl) and distilled water solution at elevated temperature (~80 ^oC) until the solution became clear, followed by evaporation and drying at 60 °C overnight. 1 mmol of as-prepared metal chlorides powder were mixed with 12 mL OA and 30 mL ODE and then heated to 150 ^oC for 40 min. under argon atmosphere to form a homogeneous solution and then cooled to room temperature. 5 mL of cyclohexane solution of 0.33 mmol core or core-shell NPs was added dropwise into the solution. Then 5 mL methanol solution of NaOH (2.5 mmol) and NH_4F (4 mmol) was added and stirred at 50 ^oC for 30 min. The mixture was degassed at 100 ^oC for 10 min. to remove cyclohexane and methanol. After that, the solution was heated to 300 ^oC for 1 h under argon atmosphere. The resultant core-shell (core-shell-shell) nanoparticles were precipitated by hexane/acetone (1:4 v/v), collected by centrifugation, washed with acetone, ethanol and DI water several times, and finally redispersed in cyclohexene. Synthesis scheme and experimental setup is presented in Fig. 5.1.

5.2.3 Synthesis of β-$NaYbF_4$:Er^{3+} Microparticles

The synthesis of *β*-$NaYbF_4$:Er^{3+} UCMPs was done *via* a modified literature procedure [77]. Metal chloride precursors were prepared by dissolving 0.99 mmol Yb_2O_3 and 0.01 mmol Er_2O_3 in 5 mL hydrochloric acid and 5 mL distilled water solution at elevated temperature (~80 °C) until the solution became clear, followed by evaporation and drying at 60 °C overnight. Metal chlorides powder were mixed with 12 mL oleic acid (OA) and 30 mL 1-octadecene (ODE) in a three-neck round-bottom flask, then heated to 150 ^oC for 40 min. under argon atmosphere to form a homogeneous solution and then cooled to room temperature. Thereafter, 10 mL of methanol solution containing NaOH (5 mmol) and NH_4F (8 mmol) was then added and the solution was stirred at 50 °C for 30 min. After methanol was evaporated under vacuum, the solution was heated to 320 °C and stirred for 1 h under argon atmosphere and left to cool down to room temperature. The resultant microparticles were precipitated by hexane/acetone (1:4 v/v), collected by

centrifugation, washed with acetone and ethanol several times, and finally redispersed in toluene. Synthesis scheme and experimental setup is presented in Fig. 5.1.

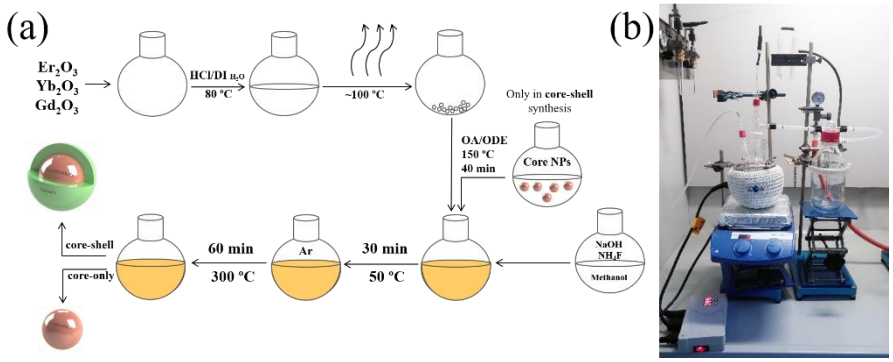

Figure 5.1 (a) Thermal decomposition synthesis scheme of core and core-shell $NaREF_4$ (RE = Gd, Yb) particles. (b) Experimental setup for synthesis of lanthanide-doped particles. The three-neck round bottom flask is set within the heating jacket, on top of the stir-plate. The left neck of the flask is supporting the thermometer sensor, middle neck is used for both the argon line and vacuum.

5.2.4 TWEEN Modification of Oleate-capped NPs

The surface modification of core-shell-shell nanoparticles was carried out following a literature protocol with a slight modifications [148]. In a typical experiment, 400 μL of TWEEN 80 was added into a round-bottom flask containing ≈20 mg of β-$NaGdF_4$:Er@$NaYbF_4$@$NaGdF_4$ and 8 mL of cyclohexene, and the solution was stirred for 1 h at room temperature. 20 mL of deionized water were poured in the flask and the dispersion was kept in a 80 °C water bath for 3 h. During this period, the cyclohexane was evaporated and the hydrophobic UCNPs were gradually converted into hydrophilic ones. The Tween 80 modified UCNPs were obtained by centrifugation. A principle mechanism by which the Tween 80 surfactant stabilizes the UCNPs is shown in Figure 5.2.

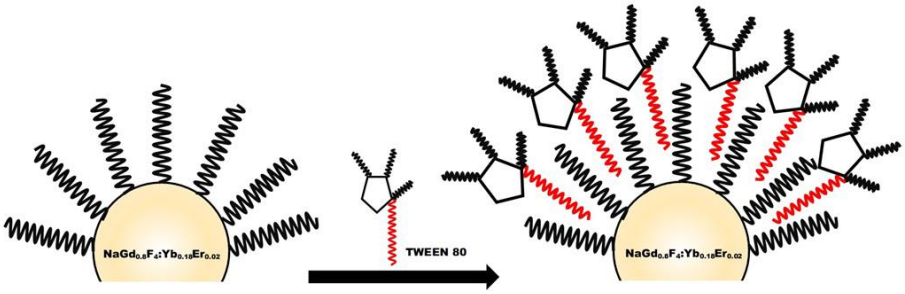

Figure 5.2 Formation of water-soluble core and core–shell UCNPs by coating with Tween 80.

5.2.5 Preparation of UCMPs Ink

The as-prepared oleic acid-capped microparticles (MPs) were dispersed in a mixed solution of ethanol (5 mL) and HCl (0.1 M, 5 mL) to prepare ligand-free particles. The mixture was sonicated for 10 min. and collected *via* centrifugation. The ink was prepared *via* mixing certain amount of as-prepared UCMPs in a solution of PAA and ethanol. Typically, 72.5 µL of PAA was dissolved in 5 mL of ethanol and sonicated for 10 min. Then, 2 mL of ethanol solution containing 15 $mg \cdot mL^{-1}$ β-$NaYbF_4:Er^{3+}$ UCMPs was prepared and added into the above-mentioned solution and stirred overnight to obtain the UCMPs-containing ink. Through using the as-prepared ink, the pattern on the paper was painted by hand. Images of the painted pattern under 980 nm laser excitation were taken with Canon EOS 70D digital camera with 950 nm short-pass filter attached.

5.3 Materials Characterization

5.3.1 Powder X-ray Diffraction Analysis

Powder X-ray diffraction (XRD) analysis has been carried out by employing a Rigaku MiniFlex II diffractometer working in the Bragg–Brentano ($\theta/2\theta$) focusing geometry. The data were collected within a 2θ angle from 10° to 65° at a step of 0.01° and scanning speed of 10 °/min using the Ni-filtered Cu K_α line.

5.3.2 SEM Analysis

The particle morphology was characterized using a field emission scanning electron microscope (SU-70 Hitachi, FE-SEM) at an acceleration voltage of 10-15 kV. The size distributions of the nanoparticles were determined from the acquired SEM images by using „Gwyddion 2.36“ software.

5.3.3 FTIR Measurements

The infrared spectra in the range of 4000–500 cm^{-1} were recorded on PerkinElmer Frontier FT-IR spectrometer.

5.3.4 Dynamic Light Scattering

Dynamic light scattering (DLS) was used to determine the hydrodynamic particle diameter and zeta potential. These experiments were performed with Brookhaven ZetaPALS zeta potential analyzer (Brookhaven Instruments, USA).

5.3.5 Fluorescence Spectroscopy

5.3.5.1 Upconversion Emission Analysis

The UC luminescence spectra were recorded using an Edinburgh Instruments FLS980 spectrometer equipped with a double emission monochromator, a cooled (−20 °C) single-photon counting photomultiplier (Hamamatsu R928), and a 1 W continuous wavelength 980 nm laser diode. The emission spectra were corrected by a correction file obtained from a tungsten incandescent lamp certified by National Physics Laboratory, UK. The measurements were performed in standard 1 cm quartz cuvettes at room temperature.

5.3.5.2 Chromaticity Analysis

Colour coordinates in CIE 1931 colour space diagrams were calculated from emission spectra employing the Edinburgh Instruments F980 software (version 1.3.1).

5.3.5.3 Temperature-dependent Optical Measurements

Temperature-dependent steady-state emission and decay measurements were done using a cryostat "MicrostatN" from the Oxford Instruments. Powder samples were used for these measurements. Liquid nitrogen was used as a cooling agent. The measurements were performed at 77 K and at 100-500 K in 25 K or 50 K intervals. Temperature stabilization time was 120 s, and temperature tolerance was set to ±5 K. During the measurements, dried nitrogen was flushed over the cryostat window to avoid the condensation of water at low temperatures on the surface of the window. The UC photoluminescence decay curves were recorded on the FLS980 spectrometer and emission was monitored at 407, 538.5, 653.5 and 1020 nm. 980 nm pulsed laser was used as an excitation source.

5.4 Biological and Magnetic Resonance Characterization

These measurements were performed by our collaborators – prof. R. Rotomskis research group at *Biomedical Physics Laboratory, National Cancer Institute, Lithuania.*

5.4.1 Cell Culturing

For nanoparticles cytotoxicity and accumulation evaluation two breast cancer cell lines were used: MDA-MB-231 (American Type Culture Collection) and MCF-7 (The European Collection of Cell Cultures). Cells were cultured in cell growth medium (Dulbecco's Modified Eagle Medium – DMEM), supplemented with 10 % (v/v) fetal bovine serum (FBS), 100 U/mL penicillin and 100 mg/mL streptomycin (all from Gibco, US). Cells were maintained at 37 °C in a humidified atmosphere containing 5 % of CO_2. The cells were routinely subcultured 2–3 times a week in 25 cm^2 culture dishes.

5.4.2 Cytotoxicity Assay

Cells were seeded on a 96-wellplate (BD Falcon, USA) at a density of 20000 cells/well. After 24h, old medium was replaced with fresh medium containing 0.01, 0.05, 0.1 mg/mL UCNPs, while media alone without nanoparticles was a control. After 24 h of treatment the old medium with

nanoparticles was aspirated and the cells were washed three times with DPBS. Viability of cells was evaluated using commercially available XTT cell viability assay (Biological Industries, Israel). XTT reaction solution was prepared according manufacturers protocol. 0.1 mL N-methyl dibenzopyrazine methyl sulphate and 5 mL tetrazolium derivative were mixed. 100 μL of fresh media and 50 μL of the reaction solution were added to each well and the plate was incubated for another 4 h in an incubator at 37 °C. After incubation, optical density values at 490 nm were measured using the microplate reader (BioTek, USA). After obtaining values of absorbance, they were recalculated as percentage values of viability. Absorbance value of control group was equated to 100 % and the rest values were calculated proportionally to control. Data are shown as mean ± standard deviation (SD). Statistical significance of differences between studied groups was assessed using a two-tailed independent Student's t-test at the 95 % confidence level. Significance was represented as p-value < 0.05.

5.4.3 Confocal Microscopy Cell Imaging

Cells were seeded in 8-well microscopy plates at density $3 \cdot 10^4$ cells/well. After 24 h, the old medium was replaced with a fresh medium containing 0.1 mg/mL of UCNPs. Cells were treated with UCNPs for the next 24 hours. After incubation with UCNPs, the nuclei of the cells were stained with Hoechst 33258 (Sigma-Aldrich, Germany). Cells were fixed with a 4% paraformaldehyde (PFA, Sigma-Aldrich, Germany) solution and stained with Alexa Fluor 488® phalloidin before imaging. The accumulation of UCNPs in cell monolayers was observed using a confocal Nikon Eclipse Te2000-S C1 Plus Laser scanning microscope (Nikon, Japan) equipped with a diode laser for 405 nm excitation, an argon laser for 488 nm excitation and a diode laser for 980 nm excitation (Nikon, Japan). Imaging was performed using 60x/1.4 NA oil immersion objective (Nikon, Japan). The three-channel RGB detector (band-pass filters 450/17, 545/45 and 688/67 for blue, green and red channels, respectively) was used. Image processing was performed using the Nikon EZ-C1 Bronze version 3.80 and ImageJ 1.46 software.

5.4.4 *In vitro* Magnetic Resonance Imaging

The magnetic resonance (MR) signal enhancement measurements were carried out on a 1.5 T clinical MRI scanner (Achieva, Philips Medical

Systems, Best, The Netherlands) in conjunction with a Sense Flex-M coil (Philips Medical Systems, Best, The Netherlands). Dilutions of core and core–shell UCNPs (0.125, 0.25, 0.5, 1.0 mg/mL) in deionized water were prepared for T1-weighted MR imaging and T1-weighted contrast enhancement. A series of aqueous solutions of UCNPs were placed in an array of 2.0 mL Eppendorf tubes with the order of UCNP concentrations and deionized water (0 mg/mL) was used as the reference. The parameters for T1-weighted MR imaging sequence was set as follows: echo time (TE) = 15.0 ms, repetition time (TR) = 500 ms, number of averages (NSA) = 8, matrix = 1024 × 1024, FOV = 200 × 200 mm, and slice thickness = 1.5 mm. The MR signal intensity (SI) in the tubes was determined by the average intensity in the defined regions of interests (ROIs). The resulting SI values in ROIs were plotted as a ratio of UCNP: water against the concentration of UCNPs.

Chapter 6. Synthesis and Functionalization of Upconversion Core-shell Nanoparticles for Possible Application as Multimodal Contrast Agents

As mentioned in *Chapter 4.2 Biomedical Application*, upconverting nanoparticles are promising, new imaging probes capable of serving as multimodal contrast agents. In present chapter, ultra-small $NaGdF_4$:18%Yb,2%Er core and $NaGdF_4$:18%Yb,2%Er@$NaGdF_4$ core–shell upconversion nanoparticles were synthesized *via* a thermal decomposition method. Hexagonal phase *β*-$NaGdF_4$ was chosen as host lattice for its ability to combine optical and magnetic resonance imaging. The upconversion luminesce intensity enhancement was achieved by employing core-shell structure, where the non-active $NaGdF_4$ shell protected the luminescent rare earth (Yb^{3+} and Er^{3+}) ions in the core from quenching caused by surface defects and organic ligands. In addition, as biomedical application requires nanoparticles to be hydrophilic and biocompatible, the surface modification was performed and the biocompatibility studies were conducted.

6.1 Size, Phase and Morphology

The scanning electron microscopy (SEM) images of the $NaGdF_4$:Yb,Er core and $NaGdF_4$:Yb,Er@$NaGdF_4$ core–shell nanoparticles are shown in Figure 6.1. Core nanoparticles are monodisperse and have a spherical shape with an average diameter of approximately 8 nm. However, the as-synthesized core–shell nanoparticles are polydisperse with an average diameter of 16 nm and 8 nm side core $NaGdF_4$ NPs are present. The polydispersity may have occurred owing to secondary nucleation during the shell growth process. However, an increase of the size suggests that the $NaGdF_4$ has been successfully epitaxially grown on the $NaGdF_4$:Yb,Er core nanoparticles. The diffraction peaks of the $NaGd_{0.8}F_4$:$_{0.18}Yb_{0.02}Er$ core (Figure 6.2 b) and $NaGd_{0.8}F_4$:$_{0.18}Yb_{0.02}Er$@$NaGdF_4$ core–shell (Figure 6.2 c) nanoparticles can be indexed as pure hexagonal β-$NaGdF_4$ phase JCPDS, Card No. 27-0699 (Figure 6.2 a), indicating no change in the crystalline phase during the shell growth.

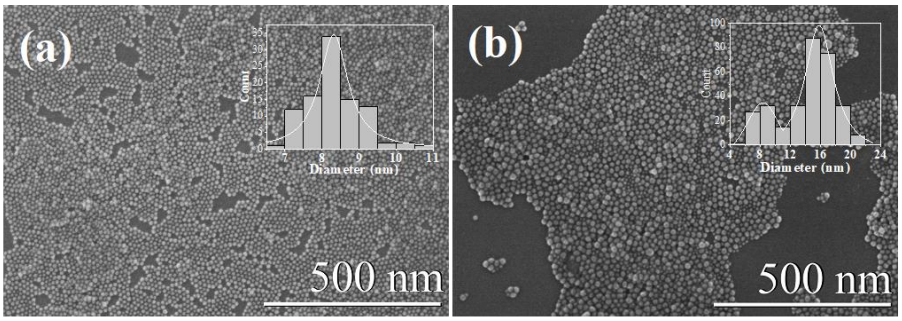

Figure 6.1 SEM images of the core $NaGdF_4$:Yb,Er (a) and core-shell $NaGdF_4$:Yb,Er@$NaGdF_4$ (b) nanoparticles. The insets display the UCNPs diameter distributions.

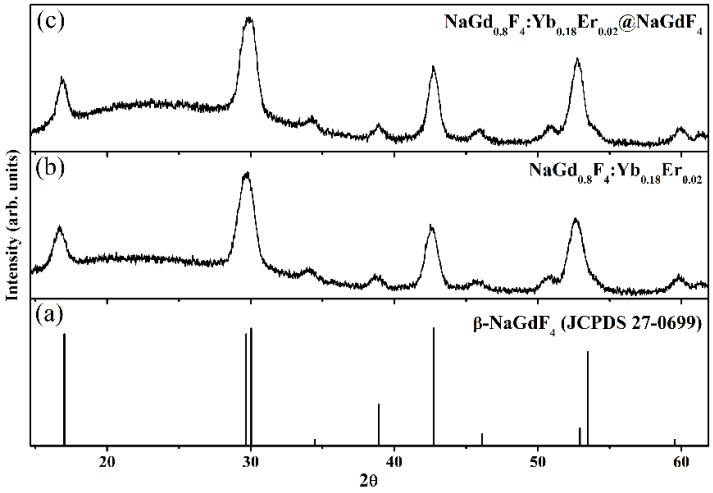

Figure 6.2 XRD patterns of: (a) the standard hexagonal $NaGdF_4$ (JCPDS No. 27-0699); (b) $NaGd_{0.8}F_{4:0.18}Yb_{0.02}Er$ core-only; (c) $NaGd_{0.8}F_{4:0.18}Yb_{0.02}Er$@$NaGdF_4$ core–shell nanoparticles.

6.2 Surface Modification

The as-obtained core and core–shell UCNPs were hydrophobic as they were stabilized by oleic acid molecules. In this work, hydrophobic core and core–shell nanoparticles were converted into hydrophilic ones using a non-ionic surfactant Tween 80. The presence of the Tween 80 coating was verified by comparing its FTIR spectra to that of pure oleic acid, oleate ligands coated

particles, pure Tween 80, and the final coated nanoparticles (Figure 6.3). $NaGdF_4$:Yb,Er UCNPs prepared in the presence of oleic acid shows characteristic absorption peaks of oleate ligands. The absorption peak at 1710 cm^{-1} (Figure 6.3 f) corresponds to the stretching vibration of C=O in pure oleic acid (Figure 6.3 a) which is replaced by two carboxylate stretching bands (1560 and 1447 cm^{-1} in Figure 6.3 e), which indicates oleate ligand adsorption on the UCNP surface.

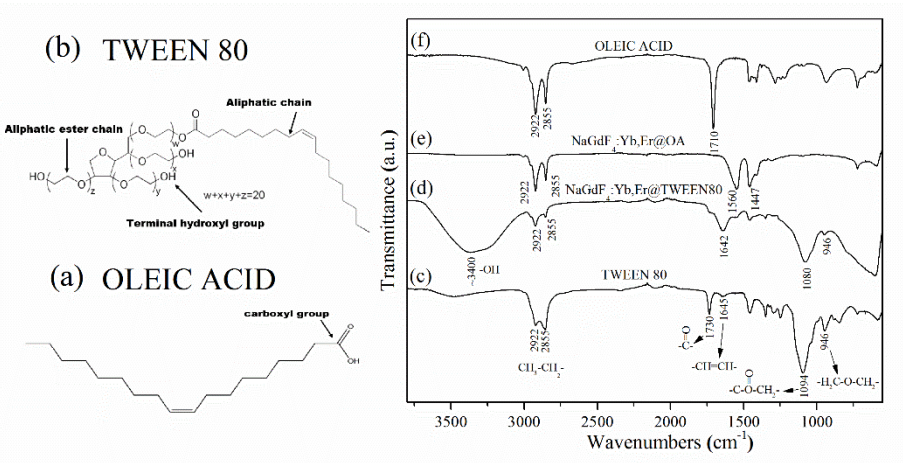

Figure 6.3 The structure of (a) oleic acid (OA) and (b) Tween 80. FTIR spectra of (c) pure Tween 80, (d) $NaGdF_4$:Yb,Er@Tween80, (e) $NaGdF_4$:Yb,Er@OA, and (f) pure OA.

Tween 80 is composed of three building blocks: aliphatic ester chains, three-terminal hydroxyl groups and an aliphatic chain (Figure 6.3 b). The aliphatic chain can be adsorbed on the hydrophobic surface by hydrophobic interactions of UCNPs as synthesized in oleic acid [149]. The strong band around 3400 cm^{-1} can be assigned to the O–H stretching vibrations (Figure 6.3 d) from terminal hydroxyl groups of Tween 80 (Figure 6.3 b) and the remaining moisture in the samples. The bands centred at 2922 and 2855 cm^{-1} are associated with the asymmetric (ν_{as}) and symmetric (ν_s) stretching vibrations of methylene ($–CH_2$), respectively. The adsorption peaks at 1730 and 1094 cm^{-1} are attributed to the ester group stretching. The band at 946 cm^{-1} is present, which corresponds to the ether bond from the aliphatic ester chains (Figure 6.3 c). The FTIR data of UCNPs@Tween80 (Figure 6.3 d) is highly comparable with that of pure Tween 80 (Figure 6.3 c), indicating that

the Tween 80 was successfully coated onto the UCNPs. Additionally, dynamic light scattering (DLS) was employed to measure the hydrodynamic diameter of Tween-coated UCNPs in the cell culture medium as well as their surface zeta potential (Fig. 6.4). The measured mean hydrodynamic diameter of the Tween-coated core $NaGdF_4$:Yb,Er UCNPs was 38 nm and the core–shell $NaGdF_4$:Yb,Er@$NaGdF_4$ particles was 48 nm. The zeta potential of Tween 80-coated core nanoparticles was about 26 mV and for core–shell nanoparticles it was slightly higher at about 33 mV.

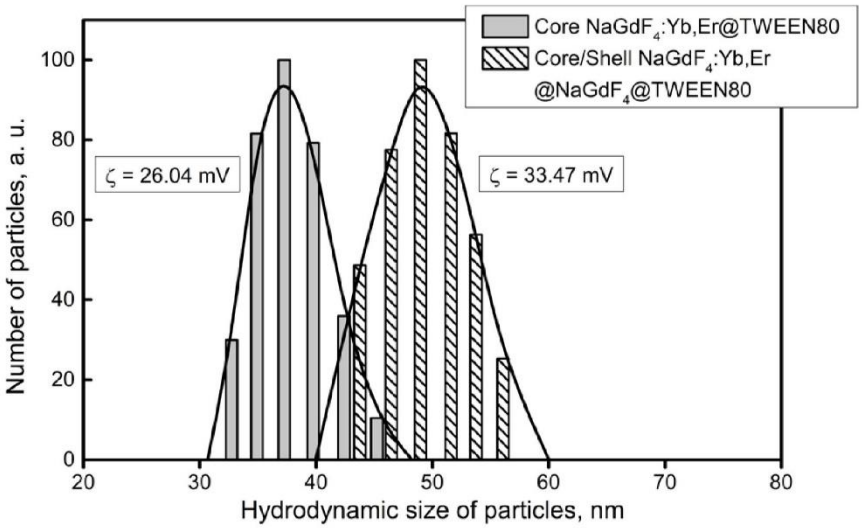

Figure 6.4 Hydrodynamic size distribution of core-only and core-shell UCNPs and their zeta potential in the cell culture medium.

6.3 Optical Properties

The upconversion emission spectra of different $NaGdF_4$:Yb,Er@$NaGdF_4$@Tween80 core–shell and $NaGdF_4$:Yb,Er@Tween80 core nanoparticles dispersed in water are shown in Figure 6.5 a. The major emissions located at 381, 408, 521, 540, 654 and 756 nm can be attributed to radiative transitions from $^4G_{11/2}$, $^2H_{9/2}$, $^2H_{11/2}$, $^4S_{3/2}$, $^4F_{9/2}$ and $^4I_{9/2}$ levels to the $^4I_{15/2}$ level of Er^{3+} (Figure 6.5 b), respectively. The comparison with the core-only nanoparticles showed that coating the $NaGdF_4$:Yb^{3+},Er^{3+} core with a shell that has the same crystal lattice structure reduce the effects of luminescence quenching from the addition of ligands

and/or surface defects and therefore a significant increase in the UCL can be observed. For the core-only nanoparticles, lanthanide dopants are exposed to surface deactivations owing to the high surface-to-volume ratio at the nanometer dimension, thus yielding UCL at low efficiency. The integrated intensity (540 nm) of the core–shell $NaGdF_4$:Yb,Er@$NaGdF_4$ nanoparticles was estimated to be about two magnitudes higher than the core-only $NaGdF_4$:Yb,Er UCNPs. The results indicate that the core–shell structure can effectively spatially isolate lanthanide dopants from being quenched, and also negate the influence of surface defects. The results correlate well with what is presented in the literature. Yi *et al*. reported that the UC emissions of hexagonal phase $NaYF_4$:Yb^{3+},Er^{3+} were enhanced by as much as seven times by growth of a 2 nm layer of $NaYF_4$ [92]. In a later publication, the same conclusion was independently verified in core–shell UCNPs of $NaGdF_4$:Yb^{3+},Tm^{3+}@$NaGdF_4$ and $KGdF_4$:Yb^{3+},Tm^{3+}@$KGdF_4$ when compared to the core under 980 nm excitation [89, 147, 150].

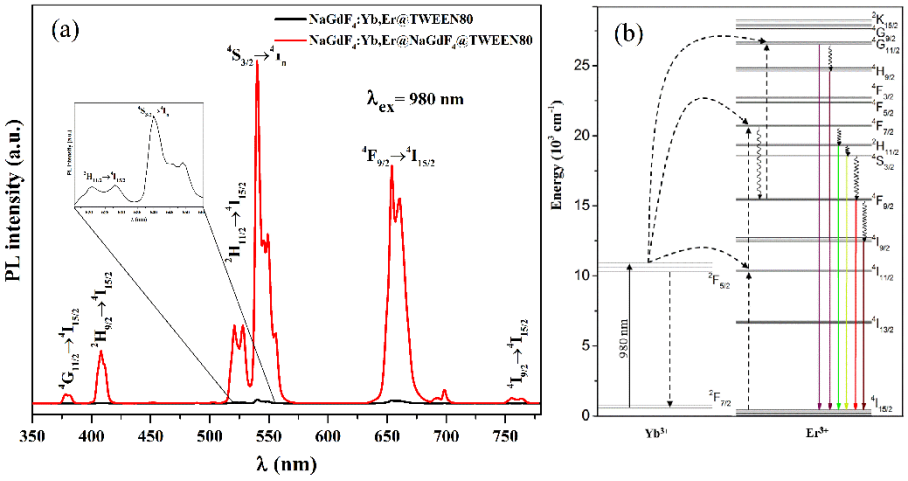

Figure 6.5 (a) Upconversion luminescence spectra of Tween 80-coated UCNPs upon 980 nm excitation and (b) energy level diagram of Yb^{3+} and Er^{3+} ions.

6.4 *In vitro* Magnetic Resonance Imaging

As shown in Figure 6.6 (inset), a positive enhancement for the magnetic resonance (MR) signal was observed for all the UCNPs samples

when compared to water. Moreover, with the increase of the concentration of UCNPs, the T1-weighted MRI signal intensity (SI) continuously increased, resulting in brighter images for both types of UCNPs. The MR SI values of UCNPs are presented in Figure 6.6. The maximum MR signal enhancement was of approximately 3.5-fold compared with the reference. There was no significant difference observed in MR signal enhancement between the core and core–shell UCNPs. Therefore, it can be concluded that the UCNP coating does not affect the favourable MRI properties of UCNPs. That signifies that the Gd^{3+} ions in the shell of the UCNPs are the major contributors toward the relaxation of water protons, and the UCNP core does not show any significant effect towards relaxivity enhancement. However, it has been shown in the literature that reduced water access to the Gd^{3+} ions may yield reduced values for MR signal enhancement [82, 151]. These observations indicate that both core and core–shell UCNPs could be applied as efficient MRI contrast agents as they both present enhanced MR signal intensity.

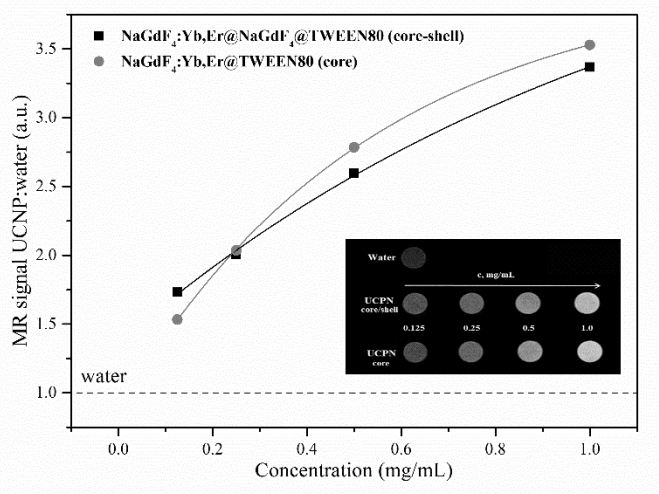

Figure 6.6 Magnetic resonance (MR) signal intensity (SI) plot of core (dots) and core–shell (squares) UCNPs of different concentrations of aqueous solutions. Water SI is marked as a dashed line as a reference; Inset: T1-weighted MR in vitro images of core and core–shell UCNPs at different concentrations of aqueous solutions.

6.5 Biocompatibility Studies

The as-prepared Tween 80-coated core–shell $NaGdF_4$:Yb,Er@$NaGdF_4$ nanoparticles were studied to evaluate their application to biological imaging using MDA-MB-231 breast cancer cells. The confocal image of MDA-MB-231 breast cancer cells after 24 h incubation with UCNPs is shown in Figure 6.7 a. The scatter of excitation light by intracellular cell structures was marked with red colour. This was obtained by excitation at 514 nm and detected at 500–530 nm. Tween 80-coated core–shell UCNPs were marked with green colour (excitation was continuous wave at 980 nm and detection at 500–530 nm). The cell nuclei were labelled with DAPI and imaged using an excitation of 405 nm and detected at using a bandpass filter with a center wavelength of 450 nm and bandwidth of 35 nm. As seen from Figure 6.7 a, the luminescence of the UCNPs came from the intracellular region, suggesting that Tween 80-coated nanoparticles were non-specifically internalized into cells and concentrated within the cytoplasm. The similar localization of Tween 80-coated nanoparticles was observed in MCF-7 cells as well. The same results of endocytic NP accumulation in cells was demonstrated in different studies with UCNPs [152], quantum dots [153], magnetic nanomaterials [154] and noble metal nanoparticles [155]. Cell viability assay XTT was performed to measure the cellular metabolic activity of human breast cancer MCF-7 and MDA-MB- 231 cell lines after 24 h treatment with core–shell Tween 80-coated UCNPs (Figure 6.7 b). Untreated cells were used as a control group. After 24 h of incubation in the UCNP concentration range from 5 to 100 μg/mL, the viability of human breast cancer MCF-7 cells remained over 92–100 % and the viability of MDA-MB-231 cells remained 85–93 %. These results clearly express that core–shell gadolinium-based UCNPs have low cytotoxicity and are in good agreement with previous studies [156, 157].

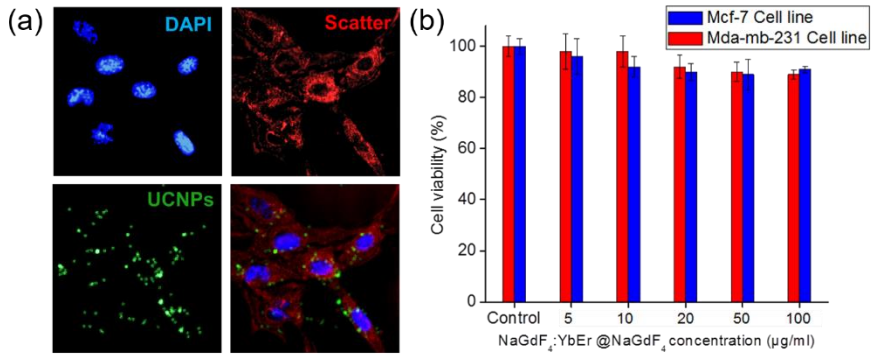

Figure 6.7 (a) Confocal images of MDA-MB-231 cells after 24 h treatment with Tween 80-coated core–shell UCNPs (10 μg/mL); UCNPs are green, DAPI staining is blue, the red colour represents excitation scattering from intracellular structures. Scale bar equals 10 μm. (b) Viability of MCF-7 and MDA-MB-213 cells, treated with different concentrations of UCNPs for 24 h. Toxicity of UCNPs was investigated using XTT cell viability assay.

6.6 Review of the Main Results

In this chapter, the synthesis of ultra-small, monodisperse, hexagonal phase core $NaGdF_4$:18%Yb,2%Er nanoparticles and polydisperse, core–shell $NaGdF_4$:18%Yb,2%Er@$NaGdF_4$ nanoparticles were presented. Oleate-capped core $NaGdF_4$:Yb,Er nanoparticles and core–shell $NaGdF_4$:Yb,Er@$NaGdF_4$ nanoparticles were successfully transferred to aqueous solutions after surface modification with the surfactant Tween 80. The core–shell UCNPs presented enhanced upconversion intensity and MR signal intensity, which indicates that these nanoparticles could be applied as an efficient dual optical, MRI contrast agent. Moreover, an *in vitro* uptake and cytotoxicity evaluation study showed that the UCNPs internalized into breast cancer cell lines and possessed low cytotoxicity and good biocompatibility. All these findings indicate that Tween 80-coated $NaGdF_4$:Yb,Er@$NaGdF_4$ UCNPs are a promising nanomaterial platform for imaging and detection in oncology.

Chapter 7. Optical Properties Study of Core-shell-shell Nanoparticles with Different Er^{3+} Activator Concentration and Their Application for Thermal Sensing and Bioimaging

The development of core-shell structure removes the low upconversion luminescence efficiency associated barrier in the way of upconversion nanoparticles multimodal applications, as mentioned in *Chapter 3.3 Core-shell Concept*. However, there is still plenty of room for further improvement of the upconversion luminescence by optimizing shell growth strategies and the dopant content in the materials. In this chapter, the core-shell-shell nanoparticles with different activator concentrations were synthesized and their upconversion luminescence and corresponding decay dynamics were investigated. In addition, the temperature-sensing properties and cellular metabolic activity as well as the distribution in human breast cancer cells of nanoparticles are discussed.

7.1 Phase and Morphology

The core-shell-shell $NaGdF_4:Er^{3+}@NaYbF_4@NaGdF_4$ UCNPs with different activator concentrations were synthesized *via* modified three-step thermal decomposition method. The core, core-shell and core-shell-shell samples were confirmed to be hexagonal phase by X-ray diffraction (XRD) analysis (Fig. 7.1). It is observed that for core and core-shell-shell nanoparticles the diffraction peaks could be indexed to the pure hexagonal-phased $NaGdF_4$ (JCPDS No. 27-0699), and no trace of the other phase or impurities was detected (Fig. 7.1 b, d). In the case of core-shell NPs (Fig. 7.1 c), the XRD peak split at 30° indicates the formation of $NaYbF_4$ (JCPDS No. 27-1427) shell.

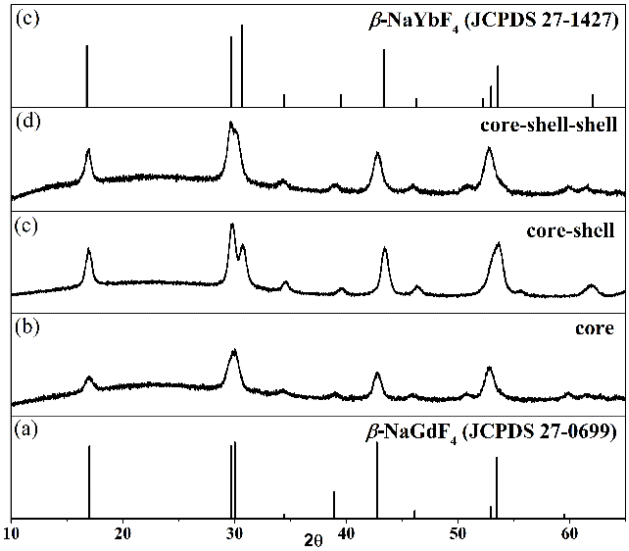

Figure 7.1 XRD patterns of: (a) the standard hexagonal $NaGdF_4$ (JCPDS No. 27-0699); (b) $NaGdF_4$:3%Er^{3+} core-only; (c) $NaGdF_4$:3%Er^{3+}@$NaYbF_4$ core–shell; (d) $NaGdF_4$:3%Er^{3+}@$NaYbF_4$@NaGdF core–shell-shell nanoparticles; and (e) the standard hexagonal $NaYbF_4$ (JCPDS No. 27-1427).

Fig. 7.2 shows the SEM images of the $NaGdF_4$:X%Er^{3+} core nanoparticles with different Er^{3+} activator concentrations (X = 1, 3, 5 and 10 mol%). It can be seen, that some of the samples contain slightly polydisperse nanoparticles. The obtained core nanoparticles are spherical in shape and their average diameter is less than 14 ± 2.1 nm (see Table 7.1). As shown in Fig 7.3, after coating with $NaYbF_4$ shell, particle size has increased. The resulting core-shell nanoparticles are monodisperse and have an average diameter of 20 ± 3.0 nm, indicating that the core nanoparticles are covered with approximately 3 nm shell. In order to protect the optically active core-shell nanoparticles, the third, inert, shell coating was applied. However, the secondary nucleation occurred and resulted in the formation of undoped $NaGdF_4$ nanoparticles (Fig. 7.4). The obtained side core nanoparticles (~ 11 ± 1.3 nm) are smaller than primary core-shell (~ 20 nm) NPs, thus confirming formation of undoped $NaGdF_4$, which has no influence on optical properties. The resulting core–shell–shell β-$NaGd_{1-x}F_4$:Er_x@$NaYbF_4$@$NaGdF_4$ UCNPs have an overall size of around 27 ± 2.6 nm (x = 0.01, 0.03, 0.05 and 0.10) (see Table 7.1).

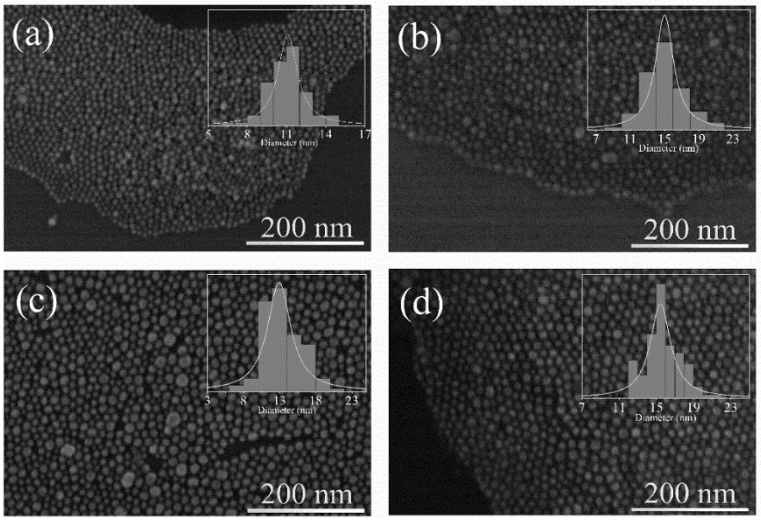

Figure 7.2 SEM images of the as-prepared (a) $NaGdF_4$:1%Er^{3+}, (b) $NaGdF_4$:3%Er^{3+}, (c) $NaGdF_4$:5%Er^{3+} and (d) $NaGdF_4$:10%Er^{3+} core nanoparticles. The insets display the UCNPs diameter distributions.

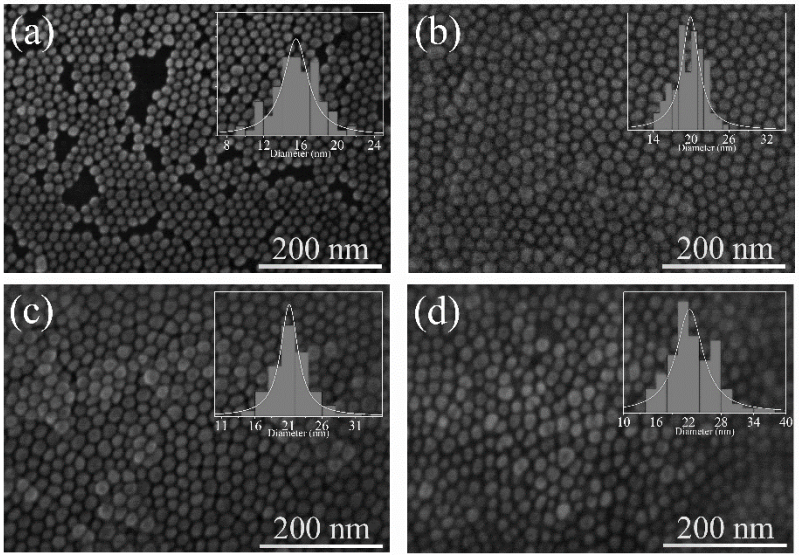

Figure 7.3 SEM images of the as-prepared (a) $NaGdF_4$:1%Er^{3+}@$NaYbF_4$, (b) $NaGdF_4$:3%Er^{3+}@$NaYbF_4$, (c) $NaGdF_4$:5%Er^{3+}@$NaYbF_4$ and (d) $NaGdF_4$:10%Er^{3+}@$NaYbF_4$ core-shell nanoparticles. The insets display the UCNPs diameter distributions.

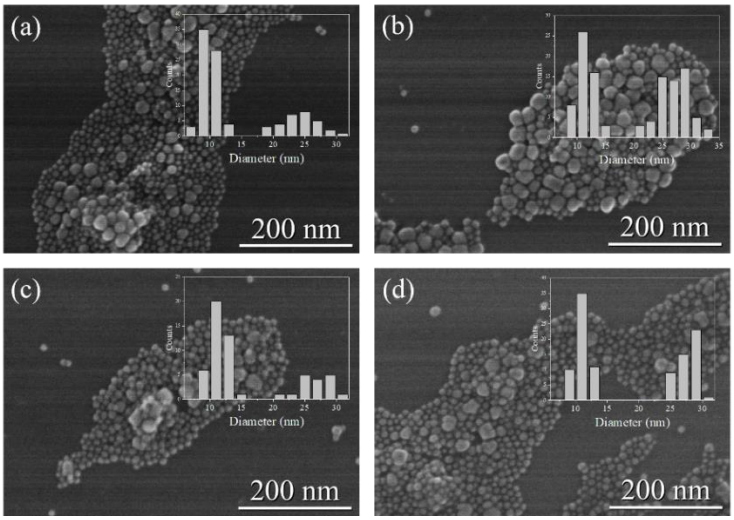

Figure 7.4 SEM images of core-shell-shell nanoparticles containing different Er^{3+} concertation in the core: (a) 1%, (b) 3%, (c) 5 % and (d) 10%. The insets display the UCNPs diameter distributions.

Table 7.1 The UCNPs size and shell thickness of the core nanoparticles doped with different concentrations of Er^{3+} ions, core-shell and core-shell-shell nanoparticles. The values in brackets represents the size of side core nanoparticles in core-shell-shell samples.

Sample	Size (nm)	Shell thickness (nm)
$NaGdF_4$:1%Er	10.2±1.4	
$NaGdF_4$:3%Er	15.1±2.3	
$NaGdF_4$:5%Er	13.4±2.6	
$NaGdF_4$:10%Er	15.8±2.0	
$NaGdF_4$:1%Er@$NaYbF_4$	15.7±2.7	2.8
$NaGdF_4$:3%Er@$NaYbF_4$	19.7±2.4	2.3
$NaGdF_4$:5%Er@$NaYbF_4$	21.4±2.7	4.0
$NaGdF_4$:10%Er@$NaYbF_4$	22.8±4.2	3.5
$NaGdF_4$:1%Er@$NaYbF_4$@$NaGdF_4$	24.2±2.7+(9.9±1.3)	4.3
$NaGdF_4$:3%Er@$NaYbF_4$@$NaGdF_4$	27.0±2.7+(11.6±1.4)	3.7
$NaGdF_4$:5%Er@$NaYbF_4$@$NaGdF_4$	26.8±2.4+(11.4±1.4)	2.7
$NaGdF_4$:10%Er@$NaYbF_4$@$NaGdF_4$	28.0±2.3+(11.2±1.2)	2.6

7.2 Optical Properties

In this study, we fabricated β-$NaGd_{1-x}F_4$:Er_x@$NaYbF_4$@$NaGdF_4$ core-shell-shell UCNPs, in which *β*-$NaGdF_4$:Er core particles were used as emitting center only and the *β*-$NaYbF_4$ shell was further introduced to act as laser energy absorption layer (Fig. 7.5). The Yb^{3+} sensitizer is confined in inner shell layer and spatially isolated from surrounding environment by inert $NaGdF_4$ shell. Such NP design provided a spatial isolation between sensitizer and activator ions. Higher concentrations of Yb^{3+} were introduced to increase absorption cross-section per nanoparticle and enhance energy transfer rates between Yb^{3+} and Er^{3+} ions [60]. However, pure β-$NaYbF_4$ has a tendency to form bigger particles and controllable synthesis of small NPs by a single-stage reaction remains an emerging goal [158]. For this reason, we restrained Yb^{3+} ions in the inner shell of the core-shell-shell system (Fig. 7.5). Growing a passivation layer on Yb^{3+} sub-lattice is a crucial synthesis step in order to eliminate luminescence intensity loss due to surface quenching effects. Figure 7.6 shows upconversion emission spectra of the $NaGdF_4$:3% Er^{3+} core, $NaGdF_4$:3% Er^{3+}@$NaYbF_4$ core-shell and $NaGdF_4$:3% Er^{3+}@$NaYbF_4$@$NaGdF_4$ core-shell-shell UCNPs under excitation at 980 nm. The major emission bands located at 381, 407, 521, 539.5 and 653.5 nm can be attributed to radiative transitions from $^4G_{11/2}$ $^2H_{9/2}$, $^2H_{11/2}$, $^4S_{3/2}$ and $^4F_{9/2}$ levels to the $^4I_{15/2}$ level of Er^{3+}, respectively (Fig. 7.6). Compared with $NaGdF_4$:Er^{3+} core-only NPs, the obtained enhancement factor of total integrated emission intensity was 50 times greater for the core-shell and almost 300 times stronger for core-shell-shell NPs (Figure 7.6). In contrast, when a double ($NaYbF_4$@$NaGdF_4$) shell was grown on $NaGdF_4$:Er to form the core–shell–shell structure, we observed an extraordinary 914-fold red emission (λ_{em} = 653.5 nm) enhancement under 980 nm excitation at room temperature. This enhancement could be attributed to the back-energy-transfer from core Er^{3+} ions to Yb^{3+} ions in the shell [159].

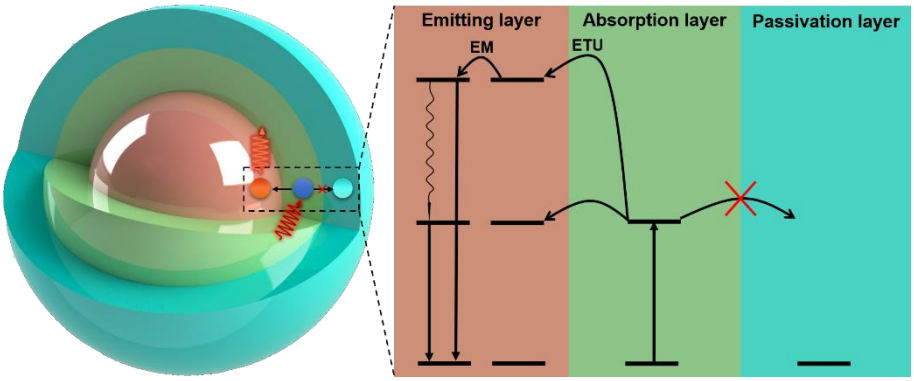

Figure 7.5 Schematic design of the lanthanide-doped core–shell–shell nanostructure for management of energy transitions. The core and shell layers are highlighted with different background colours. ETU – energy transfer upconversion, EM represents energy migration. Photoexcitation takes place in the absorption layer followed by energy transfer to the emitting layer where energy migrates among activators ions leading to higher-energy emissions. The passivation layer acts as inert protection layer.

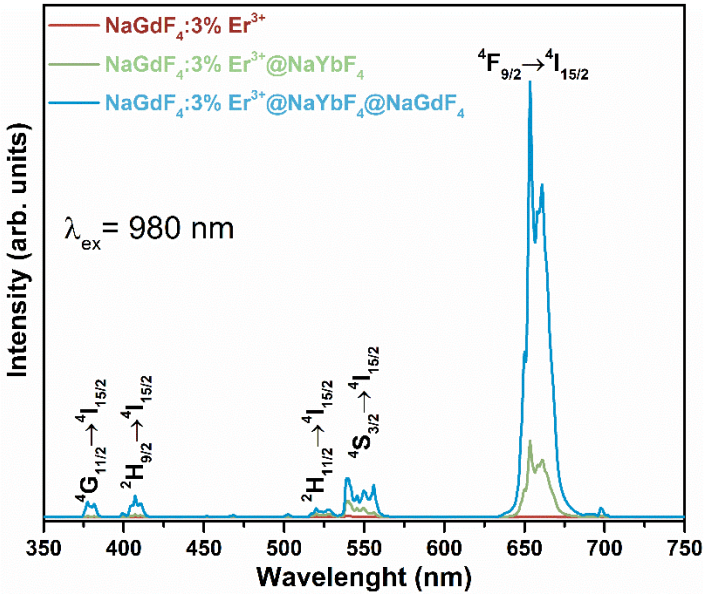

Figure 7.6 UC emission spectra of core $NaGdF_4$:3% Er^{3+}, core-shell $NaGdF_4$:3% Er^{3+}@$NaYbF_4$ and core-shell-shell $NaGdF_4$:3% Er^{3+}@$NaYbF_4$@$NaGdF_4$ UCNPs.

As mentioned before, high Yb^{3+} content can enhance upconversion process due to the capacity of absorption and sustain excitation energy. However, the excitation energy can migrate a long distance through Yb^{3+} sub-lattice especially at high Yb^{3+} content, which leads to a depletion of excitation energy (also known as concentration quenching) [13]. Since concentration and surface quenching would decrease the lifetime of emitting states, we examined the time-resolved population of most intense red emitting ($^4F_{9/2}$) level under 980 nm excitation for the core, core−shell and core−shell−shell nanoparticles (Fig. 7.7). The comparison of decay lifetimes indicates that unprotected core-shell NPs have shorter lifetimes than core and core-shell-shell samples (see Table 7.2). The results suggest that high Yb^{3+} content could decrease the Yb···Yb interatomic distance, and thus, facilitating energy hopping in the Yb^{3+} sub-lattice and excitation energy would be transferred from interior to the peripheral region of the nanoparticle, leading to an enhanced surface-quenching effect [61]. After surface coating with inert $NaGdF_4$ layer, significantly longer decay lifetimes were observed, confirming the role of the protection layer.

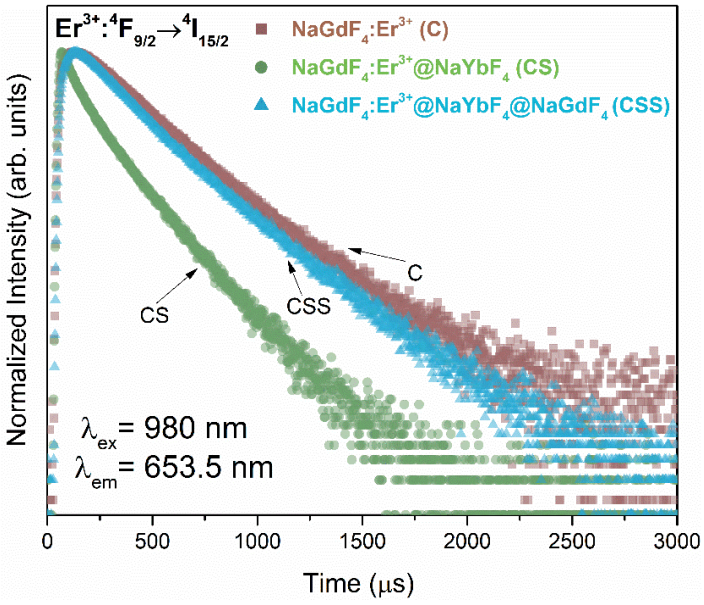

Figure 7.7 Decay kinetics of red emitting state of $^4F_{9/2}$ for core, core-shell and core-shell-shell nanoparticles under 980 nm laser excitation.

Table 7.2 Fitted lifetimes and relative ratio factor (R_i) of the $^4F_{9/2}$ (653.5 nm) level.

	τ_1, µs	R_1, %	τ_2, µs	R_2, %	$\tau_{average}$, µs
Core	255.7	90.6	620.3	9.4	290.0
Core-shell	76.6	25.8	207.3	74.2	173.6
Core-shell-shell	189.3	51.7	335.6	48.3	260.1

In order to study the luminescence kinetics and investigate the effect of different Er^{3+} doping concentration, the decay profiles of emission were measured. Since core sample contains only activators ions and emission intensities are relatively weak, we examined only core-shell and core-shell-shell samples. As seen in Fig. 7.8 and Fig. 7.9, the decay curves were obtained by monitoring the wavelength of 407 nm ($^2H_{9/2}\rightarrow{}^4I_{15/2}$), 539.5 nm ($^4S_{3/2}\rightarrow{}^4I_{15/2}$) and 653.5 nm ($^4F_{9/2}\rightarrow{}^4I_{15/2}$) for Er^{3+} ions. The decay curves are bi-exponential and can be written as:

$$I(t) = I_1 \exp\left(-\frac{t}{\tau_1}\right) + I_2 \exp\left(-\frac{t}{\tau_2}\right) \qquad (Eq.\ 7.1)$$

where τ_1 and τ_2 represent the shorter and longer lifetime constants, respectively, and I_1 and I_2 are the original contribution for the shorter and longer decay times, respectively. The obtained lifetime values were listed in Table 7.3. As shown in Fig. 7.8, the sample, which contains 1% of Er^{3+} concentration in core, shows longest decay lifetimes for all emission bands. The lifetimes of $^2H_{9/2}\rightarrow{}^4I_{15/2}$ and $^4S_{3/2}\rightarrow{}^4I_{15/2}$ transitions are shorter than that of $^4F_{9/2}\rightarrow{}^4I_{15/2}$ and these observations are in good agreement with previous investigation involving high Yb^{3+} concentrations [160]. This could be ascribed to the more relaxation pathways of $^2H_{9/2}$ and $^4S_{3/2}$ states than that of $^4F_{9/2}$ one and could be caused by back-energy transfer (BET) from Er^{3+} to Yb^{3+} ions [61]. The decay lifetimes of core-shell-shell samples are about two times longer than of core-shell ones (Fig. 7.9 and Table 7.3), indicating that the growth of an inert shell on the core-shell NPs can significantly increase the average lifetimes. It was also found, that the emission decay lifetimes at 653.5 nm of core-shell-shell UCNPs show similar decay profiles and was determined to be around 253.3 µs, around 1.4 times longer than the core-shell ones (187.3 µs) (Table 7.3). However, the decay lifetime for the red emitting

state of the $NaGdF_4$:3% Er^{3+}@$NaYbF_4$@$NaGdF_4$ sample shows slightly longer lifetimes (260.1 μs) and for this reason, we choose this sample for further investigation on temperature-dependent measurements and bioimaging studies.

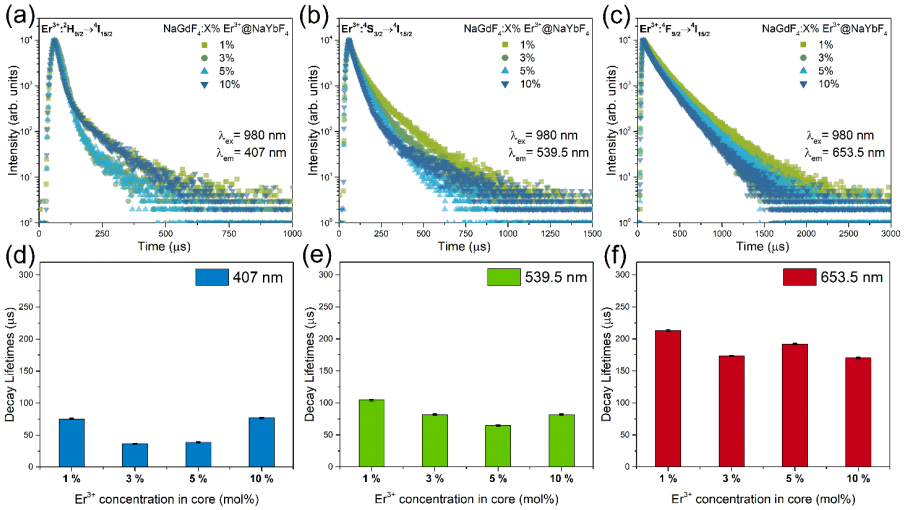

Figure 7.8 Variation of visible UC emission lifetimes in core-shell nanoparticles with different concentration of Er^{3+} ions in core.

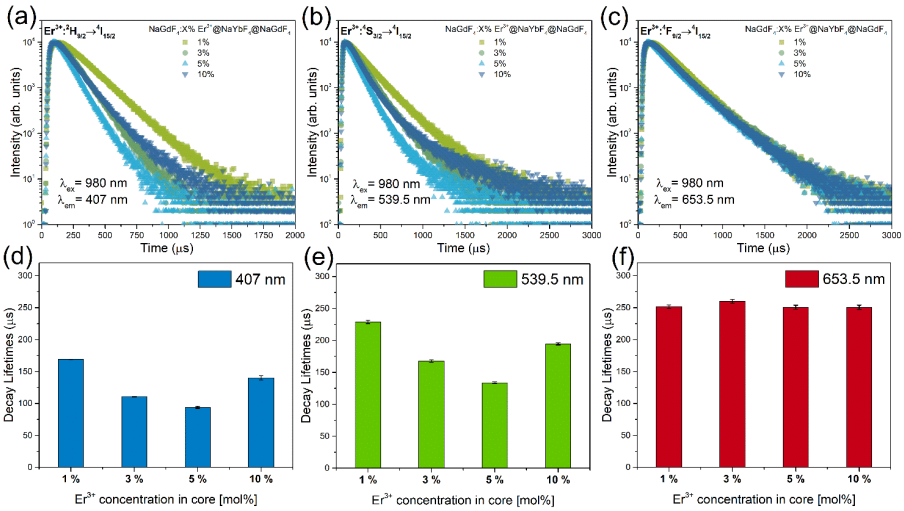

Figure 7.9 Variation of visible UC emission lifetimes in core-shell-shell nanoparticles with different concentration of Er^{3+} ions in core.

Table 7.3 Lifetime values of Er^{3+} ($^2H_{9/2}$, $^4S_{3/2}$, $^4F_{9/2}$) in core-shell and core-shell-shell UCNPs doped with different concentration of Er^{3+} ions in core NPs.

		Core-shell				***Core-shell-shell***			
Er^{3+} in core (X, mol%)		**1**	**3**	**5**	**10**	**1**	**3**	**5**	**10**
$^2H_{9/2} \rightarrow {}^4I_{15/2}$ (407 nm)	**τ_1, µs**	21.1	17.5	17.1	22.2	169.3	110.7	86.4	105.7
	R_1, %	40.2	82.5	71.8	38.4	100.0	100.0	92.7	68.7
	τ_2, µs	111.3	124.0	93.7	110.6	-	-	188.5	215.9
	R_2, %	59.8	17.5	28.2	61.6	-	-	7.3	31.3
	$\tau_{avg.}$, µs	**75.0**	**36.1**	**38.7**	**76.6**	**169.3**	**110.7**	**93.9**	**140.2**
$^4S_{3/2} \rightarrow {}^4I_{15/2}$ (539.5 nm)	**τ_1, µs**	56.0	47.9	47.4	38.9	197.7	143.0	110.4	128.7
	R_1, %	52.8	63.7	76.1	76.4	83.3	86.1	88.5	78.3
	τ_2, µs	158.8	141.1	119.8	221.1	386.0	318.6	313.8	431.7
	R_2, %	47.2	36.3	23.9	23.6	16.7	14.0	11.5	21.7
	$\tau_{avg.}$, µs	**104.5**	**81.8**	**64.7**	**81.9**	**229.1**	**167.5**	**133.8**	**194.5**
$^4F_{9/2} \rightarrow {}^4I_{15/2}$ (653.5 nm)	**τ_1, µs**	134.0	76.6	84.7	87.7	238.8	189.3	161.4	198.0
	R_1, %	50.0	25.8	22.5	30.6	94.8	51.7	38.2	62.8
	τ_2, µs	292.7	207.3	223.2	206.8	478.2	335.6	305.9	339.3
	R_2, %	50.0	74.2	77.5	69.4	5.2	48.3	61.8	37.2
	$\tau_{avg.}$, µs	**213.3**	**173.6**	**192.1**	**170.4**	**251.4**	**260.1**	**250.8**	**250.6**

7.3 Temperature-Dependent Upconversion Luminescence Properties

As reported, the temperature-induced processes of energy migration from activators to surface defects contribute to the increased UC emission intensity of lanthanide-doped fluoride NPs [160, 161]. The UCL properties of $NaGdF_4$:3% Er^{3+}@$NaYbF_4$@$NaGdF_4$ nanoparticles were investigated by temperature-dependent steady-state PL spectroscopy under a 980 nm continuous-wave (CW) laser excitation. The spectra show systematic changes as the temperature increases from 77 to 500 K (Fig. 7.10). As shown in Fig. 7.10 a, b, the UCL intensity of red ($^4F_{9/2} \rightarrow {}^4I_{15/2}$) emission does not remain constant as the temperature changes. At cryogenic temperatures (77<T<250) emission remains stable until the temperature reaches 250 K. With increasing the temperature from 250 K to 400 K, the integrated UCL emission intensity increases by ~8.6 times and decreases with further rising the temperature to 500 K. This enhancement may be associated with negative thermal quenching effect [162], which was proposed by several groups in their recent works [162-165] and ascribed to the reduced energy migration-mediated surface quenching, enabled by high Yb^{3+} concentrations. These findings imply that high Yb^{3+} doping concentration may intensify the local energy supply to the activator ions and thus promote upconversion emission.

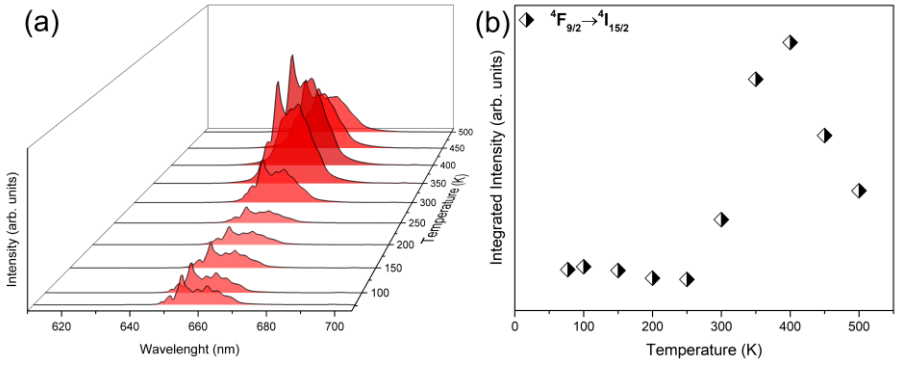

Figure 7.10 (a) Steady-state UCL spectra at different temperatures (77-500 K) of $NaGdF_4$:3% Er^{3+}@$NaYbF_4$@$NaGdF_4$ nanoparticles under a 980 nm laser irradiation; (b) Temperature dependent integrated UCL intensity values of the emission peak at 653.5 nm.

The two 4f levels of Er^{3+}: $^2H_{11/2}$ and $^4S_{3/2}$ exhibit distinguishable difference in temperature dependent variations, which has been widely applied in fluorescence intensity ratio (FIR)-based temperature sensing [116, 166]. The electrons of the $^4S_{3/2}$ state could easily thermally populate the $^2H_{11/2}$ state, resulting in the emission intensity variation as a function of temperature. The relative FIR versus absolute temperature could be well fitted with an exponential function [17]:

$$\mathrm{FIR} = \frac{I_H}{I_S} = C \exp\left(-\frac{\Delta E}{k_B T}\right) \qquad (Eq.\ 7.2)$$

where I_H and I_S are the fluorescence intensities for the emissions from the higher ($^2H_{11/2}$) and lower ($^4S_{3/2}$) thermally coupled levels, respectively, C is a temperature-independent constant, ΔE is the energy gap between the two excited states ($^2H_{11/2}$ and $^4S_{3/2}$), k_B is the Boltzmann constant, and T is the absolute temperature. As shown in Fig. 7.11, the green UC emission (522 nm) intensity enhances evidently with normalizing the intensity to 539.5 nm. The dependence of FIR on the absolute temperature for $NaGdF_4$:3% Er^{3+}@$NaYbF_4$@$NaGdF_4$ sample, which is shown in Fig. 7.11 b, can be well fitted with an exponential function:

$$Ln(FIR) = 1.78 - \frac{894.9}{T} \qquad (Eq.\ 7.3)$$

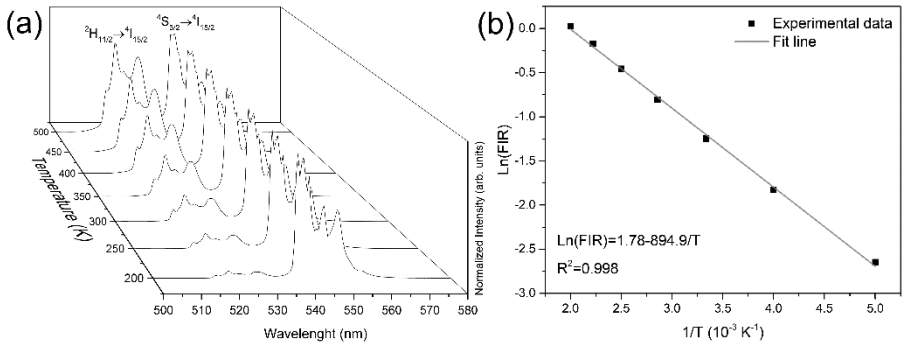

Figure 7.11 (a) $NaGdF_4$:3% Er^{3+}@$NaYbF_4$@$NaGdF_4$ temperature-dependent green UC luminescence spectra normalized to 539.5 nm, under 980 nm laser excitation; (b) FIR data versus absolute temperature.

The effective energy difference (ΔE) obtained from the fitting is 622 cm^{-1}, which is close the splitting of ~700 cm^{-1} between $^2H_{11/2}$ and $^4S_{3/2}$ multiplets. One of the most important parameters describing luminescent thermometers is their relative sensitivity (S_R) to temperature changes, which is mathematically expressed as [109]:

$$S_R = \frac{d(FIR)}{dT} \times \frac{1}{FIR} = \frac{\Delta E}{k_B T^2} \qquad (Eq.\ 7.4)$$

As shown in Fig. 7.12, in the examined temperature range (200-500 K) the S_R value decreases from 2.24 to 0.36 $\%\cdot K^{-1}$ (S_R=895/T^2) and in the physiological temperature range S_R value is around 0.99 $\%\cdot K^{-1}$. These results imply that the core-shell-shell nanoparticles are comparable to most of the reported Er^{3+}-based nano-systems [167, 168].

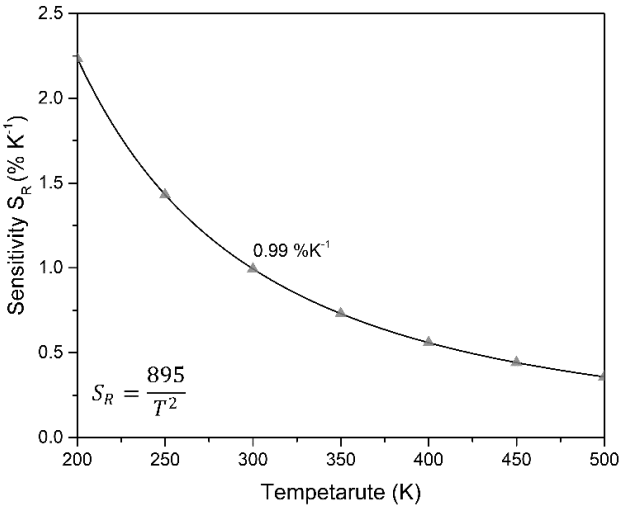

Figure 7.12 Plot of the relative sensitivity S_R as a function of temperature in the range of 200-500 K for $NaGdF_4$:3% Er^{3+}@$NaYbF_4$@$NaGdF_4$ nanoparticles.

7.4 Biocompatibility Studies

Furthermore, cell viability assay XTT was performed to measure cellular metabolic activity after 24 hours treatment with different concentrations of $NaGdF_4$:3%Er^{3+}@$NaYbF_4$@$NaGdF_4$ nanoparticles (Fig. 7.13). Nanoparticles have no influence on viability of both MDA-MB-231 MCF-7 cells after

incubation with 0.01 mg/mL $NaGdF_4$:3% Er^{3+}@$NaYbF_4$@$NaGdF_4$ UCNPs solutions. After incubation with 0.05 mg/mL solution, there was not any significant influence on viability of MCF-7 cells, but viability of MDA-MB-231 slightly decreased (88±5 %). However, a decrease of viability was observed after incubation with 0.1 mg/mL $NaGdF_4$:3% Er^{3+}@$NaYbF_4$@$NaGdF_4$ UCNPs solution for both MDA-MB-231 and MCF-7 cells, viability decreased to 76±8 % and 78±3 % respectively. Though, 0.1 mg/mL concentration is extremely high and for biological application lower concentrations, such as 0.01 mg/mL should be more than sufficient.

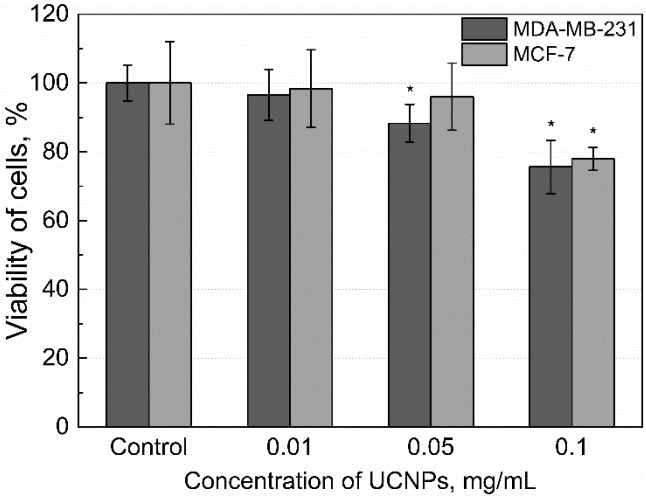

Figure 7.13 Viability of MDA-MB-231 and MCF-7 breast cancer cells incubated at different concentrations (0.01; 0.05; 0.1 mg/mL) of $NaGdF_4$:3% Er^{3+}@$NaYbF_4$@$NaGdF_4$ UCNPs for 24 h. Toxicity of nanoparticles was investigated using XTT cell viability assay. Error bars show the standard deviations. * indicates significant differences compared to the non-treated cells (Control) ($p \leq 0.05$).

$NaGdF_4$:3%Er^{3+}@$NaYbF_4$@$NaGdF_4$ UCNPs accumulation in MDA-MB-231 and MCF-7 cells was investigated with confocal microscopy. Nanoparticles uptake studies revealed that $NaGdF_4$:3%Er^{3+}@$NaYbF_4$@$NaGdF_4$ UCNPs had penetrated into both cell lines (Fig. 7.14). Higher UC emission was collected from MDA-MB-231 cells, implying that MDA-MB-231 accumulates UCNPs better that MCF-7 cells. The same difference of nanoparticles accumulation in this two cell lines

was demonstrated in previous publication [10]. In MDA-MB-231 cells UCNPs were clearly localized in the perinuclear region (Fig 7.14 a–c), whereas distribution of UCNPs in MCF-7 is not so accurate: UCNPs were mostly localized near nucleus, but there were nanoparticles localized in cytoplasm near plasma membrane (Fig. 7.14 e–f). In both cell lines no UCNPs were detected in nuclei, indicating that UCNPs could not penetrate trough nuclear envelope.

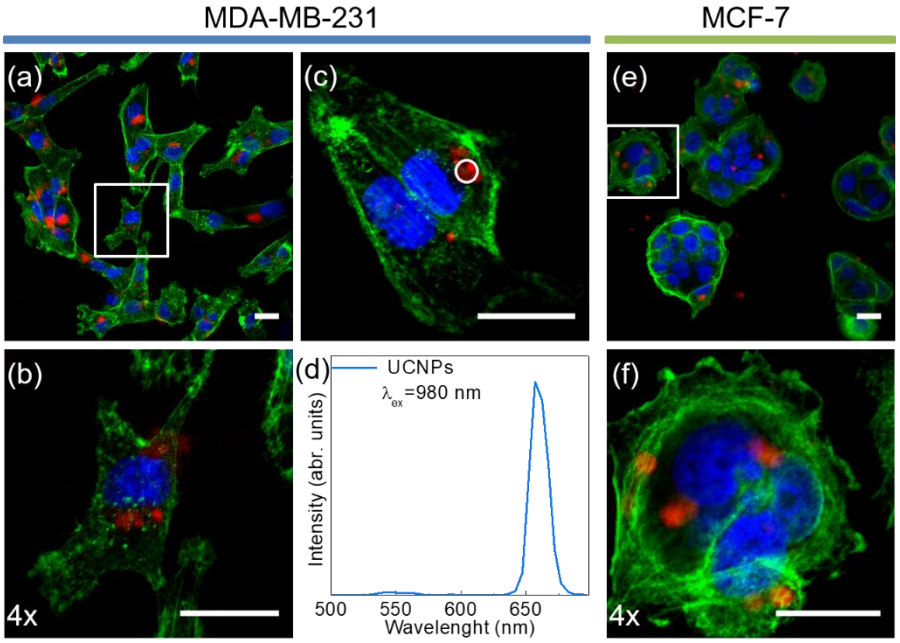

Figure 7.14 Accumulation of $NaGdF_4$:3% Er^{3+}@$NaYbF_4$@$NaGdF_4$ UCNPs (red colour) (λ_{ex}=980 nm) in MDA-MB-231(a-c) and MCF-7 (e-f) breast cancer cells after 24 h of incubation with nanoparticles. (a) – distribution of UCNPs in MDA-MB-231 cells; (b) - enlarged area of the region highlighted by the white box in a; (c) –intracellular accumulation of UCNPs in MDA-MB-231 cells; (d) – measured spectrum of UCNPs inside cell (area marked with white circle); (e) – distribution of UCNPs in MCF-7 cells; (f) - enlarged area of the region highlighted by the white box in e. Cell nuclei stained with Hoechst 33258 (blue colour) (λ_{ex}=404 nm). Filamentous actin of cells stained with Alexa Fluor 488® phalloidin (λ_{ex}=488 nm). Scale bars in all images correspond to 20 µm.

7.5 Review of the Main results

In this chapter, the series of $NaGdF_4$:Er@$NaYbF_4$@$NaGdF_4$ core-shell-shell UCNPs with different Er^{3+} doping concentration were prepared *via* thermal decomposition synthesis method. The enhancement degree of the integral UC emission intensity increases with double shell coating and significant red emission enhancement were observed in core-shell-shell NPs. The luminescence decay properties of samples containing different Er^{3+} doping concentration were analysed and the best results were obtained from 3% containing core-shell-shell. In addition, based on the different temperature dependent UC emission intensity variation of the two thermally states of Er^{3+}:$^2H_{11/2}$ and $^4S_{3/2}$, the maximum relative temperature sensitivity (S_R) of $0.99\%\cdot K^{-1}$ at 300 K is achieved. Moreover, as prepared UCNPs are stable in higher temperatures and also shows good biocompatibilities.

Chapter 8. Synthesis of Er^{3+}-activated $NaYbF_4$ Upconverting Microparticles for Optical Temperature Sensing

The temperature-dependent photoluminescence is of a great importance for both science and technology fields as discussed in *Chapter 4.1 Thermal Sensing*. Therefore, it is important to choose an appropriate thermally stable host material, which provides efficient fluorescence signal for successful practical applications using fluorescence intensity ratio technique. In this chapter the detailed analysis of the optical properties of Er^{3+}-activated $NaYbF_4$ microparticles is presented. In addition, the temperature sensing capabilities as well as possible application as anti-counterfeiting pigments are evaluated.

8.1 Phase, Size and Morphology

Fig. 8.1 a show the XRD pattern of $NaYbF_4$:Er^{3+} microparticles synthesized *via* the thermal decomposition method. The XRD pattern reveals that the diffraction peaks of the sample coincide with the standard data of $NaYbF_4$ from Joint Committee on Powder Diffraction Standard (JCPDS No. 27-1427) and no extra peaks of impurities are seen, which indicates that the Er^{3+} dopants uniformly enter the lattice of $NaYbF_4$. The crystal structure is hexagonal (β) phase with space group *P6* (#168). The scanning electron microscopy (SEM) image of the as-synthesized sample is shown in Fig. 8.1 b. The morphology of synthesized β-$NaYbF_4$:Er^{3+} particles is hexagonal microplates with average diameter of ~360 nm and height up to ~130 nm. The diameter and height size distribution histograms of microplates are shown in Fig. 8.1 c-d.

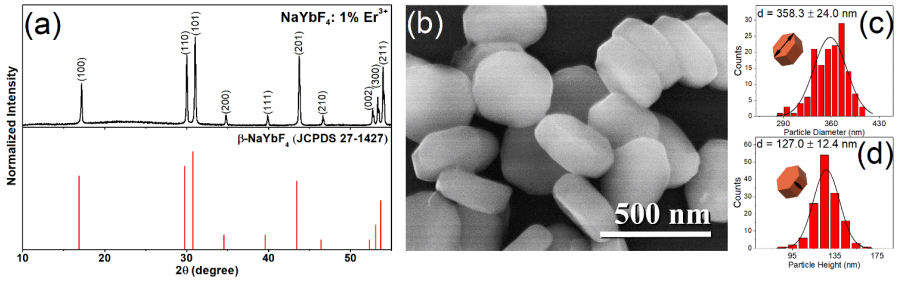

Figure 8.1 (a) XRD pattern, compared to the standard hexagonal $NaYbF_4$ (JCPDS No.27-1427); (b) SEM image; histogram of diameter (c) and height (d) size distribution of the $NaYbF_4:Er^{3+}$ microplates.

8.2 Upconversion Emission Properties

Under the excitation of 980 nm laser radiation, the room-temperature UC performance of the $NaYbF_4:1\%Er^{3+}$ microparticles was studied. As presented in Fig. 8.2, the UC spectrum was dominated by a red UC emission at 653.5 nm corresponding to the $^4F_{9/2} \rightarrow {}^4I_{15/2}$ transition of Er^{3+} ions. Meanwhile, a relatively weak near-infrared, two green, and blue UC emissions at ca. 810, 538.5, 519.5 and 407 nm are attributed to the $^4I_{9/2} \rightarrow {}^4I_{15/2}$, $^4S_{3/2} \rightarrow {}^4I_{15/2}$, $^2H_{11/2} \rightarrow {}^4I_{15/2}$ and $^2H_{9/2} \rightarrow {}^4I_{15/2}$ transitions, respectively. Since the red UC emission intensity was much higher than the rest, the synthesized microparticles can emit eye-visible red emission under 980 nm excitation, as shown in the inset of Fig. 8.2.

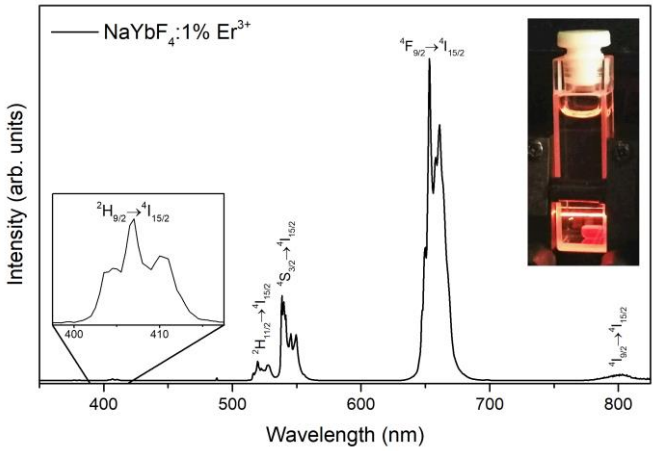

Figure 8.2 Room-temperature UC emission spectrum of the Er^{3+}-activated $NaYbF_4$ microparticles excited at 980 nm. Inset on the right shows the cuvette with $NaYbF_4$:Er^{3+} MPs under the 980 nm laser irradiation, and inset on the left shows the close-up of blue emission.

8.3 Temperature-Dependent Upconversion Luminescence Properties

The UCL properties of $NaYbF_4$:Er^{3+} were investigated by temperature-dependent steady-state PL spectroscopy under a 980 nm continuous-wave (CW) laser excitation. The spectra show systematic changes as the temperature increases from 77 to 500 K (Fig. 8.3). As shown in Fig. 8.4 a, the UCL intensities of red, green and blue emission do not remain constant as the temperature changes. At cryogenic temperatures (77<T<250) red and green emission shows a maximum intensity point at ~150 K and then decreases until the temperature reaches 250 K, because of the excitation energy dissipation processes. Enhancement at low temperatures could be attributed to the increased probabilities of the energy transfer upconversion (ETU) processes by thermal activation (Fig. 8.4 b). The ETU processes result from interactions within different energy levels of Yb^{3+} and Er^{3+} with temperature change. Moreover, the cross-relaxation (CR) processes can be significantly enhanced at higher temperatures (Fig. 8.4 b), which could alter the emission intensity. Intriguingly, another UCL enhancement is recorded at 325 K, which may be associated with negative thermal quenching effect [162]. This phenomenon was proposed by several groups in their recent works [162-165], which is

ascribed to the reduced energy transfer possibility from activators to surface defects at elevated temperatures. These findings imply that at different temperature upconversion process may possess different energy relaxation mechanisms. The overall effect is a result of the competition of different non-linear optical processes and it can be observed that total luminescence emission intensities decrease as temperature increases.

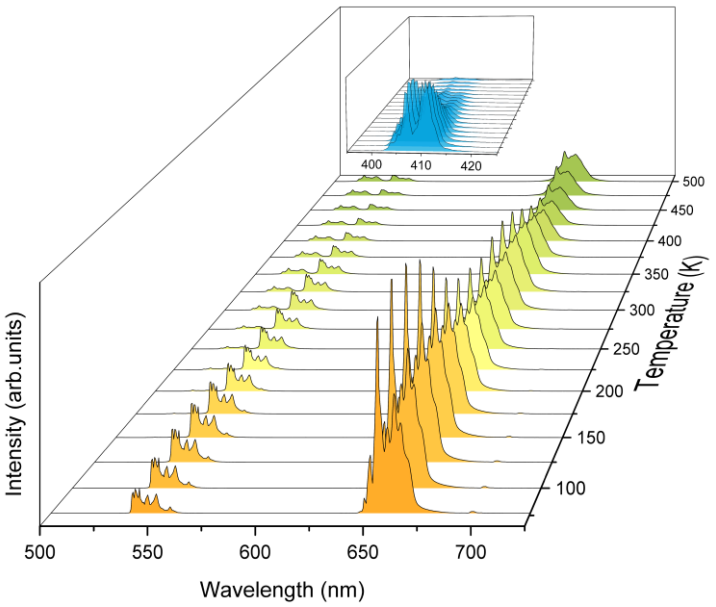

Figure 8.3 Steady-state UCL spectra at different temperatures (77-500 K) of $NaYbF_4$:1%Er^{3+} microparticles under a 980 nm laser irradiation. Inset illustrate the blue emission UCL spectra.

In order to further understand temperature effect on UCL processes, the blue, green and red UC emission dynamic curves of $^2H_{9/2} \rightarrow {}^4I_{15/2}$ (407 nm), $^4S_{3/2} \rightarrow {}^4I_{15/2}$ (538.5 nm), and $^4F_{9/2} \rightarrow {}^4I_{15/2}$ (653.5 nm) transitions were measured under 980 nm pulsed laser excitation as shown in Fig. 8.5. Each decay curve can be fitted with a single-exponential equation, as follows:

$$I_t = I_0 exp\left(\frac{-t}{\tau}\right) \qquad (Eq.\ 8.1)$$

where I_t is the luminescence intensity at a given time, I_0 is the initial emission intensity at $t = 0$ and τ is the lifetime.

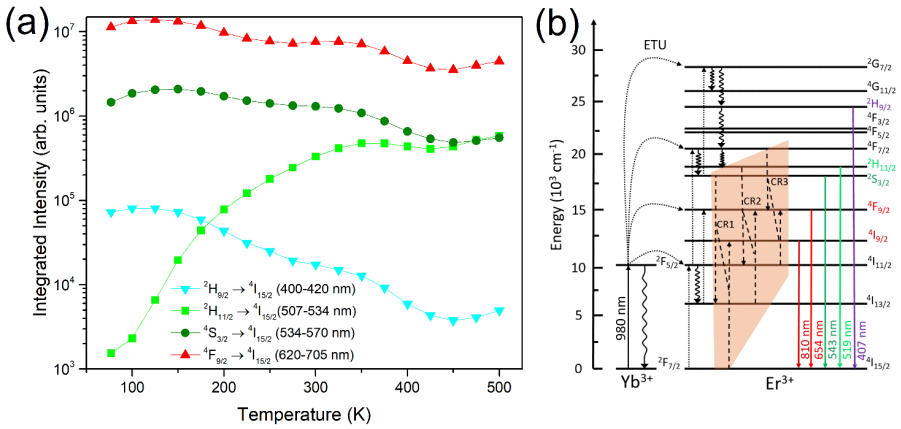

Figure 8.4 (a) Temperature dependent integrated UCL intensity plots of the emission peaks at 407, 519.5, 538.5 nm and 653.5 nm; (b) Energy scheme of Er^{3+} co-doped $NaYbF_4$; ETU: energy transfer upconversion and CR: cross relaxation at higher temperatures.

Table 8.1 shows the calculated luminescence lifetimes of the sample under 980 nm excitation according to Eq. (8.1). At low temperatures, predictable decline in luminescence lifetime was observed, but an unexpected rise for all the emission bands (407, 538.5, and 653.5 nm) was noticed with increasing the temperature. This abnormal thermal enhancement was detected at various temperatures for different emission bands. As shown in Fig. 8.5 b, e, the lifetime of Er^{3+} $^4S_{3/2}$ excited state exhibits a significant increase from 79 to 204 µs as the temperature goes from 250 to 500 K, which could be associated with a growing thermal suppression of non-radiative relaxation process. Similar behaviour was recognized for blue emission band ($^2H_{9/2}$) as shown in Fig. 8.5 a, d. Furthermore, the lifetime of the $^4F_{9/2}$ excited state (Fig. 8.5 c, f) increases gradually with a rise from 281 to 442 µs, in temperature interval from 400 to 500 K, which might be due to the negative thermal quenching effect [162-164].

Table 8.1 Fitted lifetimes and coefficient values (χ^2) of the $^2H_{9/2}$ (407 nm), $^4S_{3/2}$ (538.5 nm), and $^4F_{9/2}$ (653.5 nm) levels at different temperatures (77-500 K).

Temperature	407 nm		538.5 nm		653.5 nm	
	τ, μs	χ^2	τ, μs	χ^2	τ, μs	χ^2
77 K	90.56	1.258	110.68	1.216	710.73	1.314
100 K	84.55	1.283	106.90	1.382	710.65	1.217
150 K	76.55	1.119	96.82	1.166	682.93	1.274
200 K	67.27	1.125	85.84	1.216	627.32	1.088
250 K	61.80	1.083	78.47	1.148	546.93	1.112
300 K	69.09	1.256	83.14	1.010	449.68	1.003
350 K	79.31	1.104	105.07	1.039	352.10	1.170
400 K	87.01	1.176	114.66	1.000	281.69	1.235
450 K	-	-	135.96	1.021	305.15	1.341
500 K	-	-	204.34	1.238	442.54	1.339

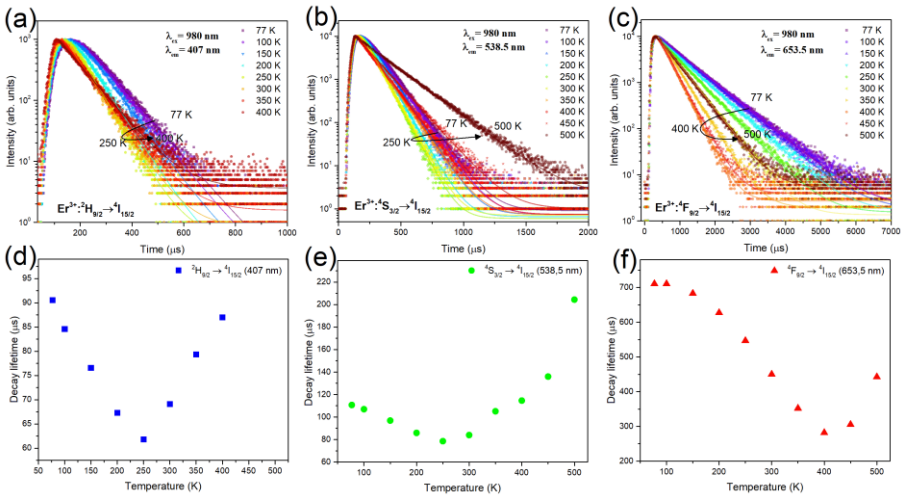

Figure 8.5 Temperature dependence of the kinetic decay curves and calculated lifetimes of the $^2H_{9/2} \rightarrow {}^4I_{15/2}$ (407 nm) (a, d), $^4S_{3/2} \rightarrow {}^4I_{15/2}$ (538.5 nm) (b, e), and $^4F_{9/2} \rightarrow {}^4I_{15/2}$ (653.5 nm) (c, f) transitions in the 77-500 K temperature range of $NaYbF_4$:1%Er^{3+} microparticles.

To fully investigate this unique UC luminescence prolonged lifetimes, temperature-dependent down-conversion luminescence (DCL) decay curves of $NaYbF_4:Er^{3+}$ were also investigated upon excitation at 980 nm (Fig. 8.6).

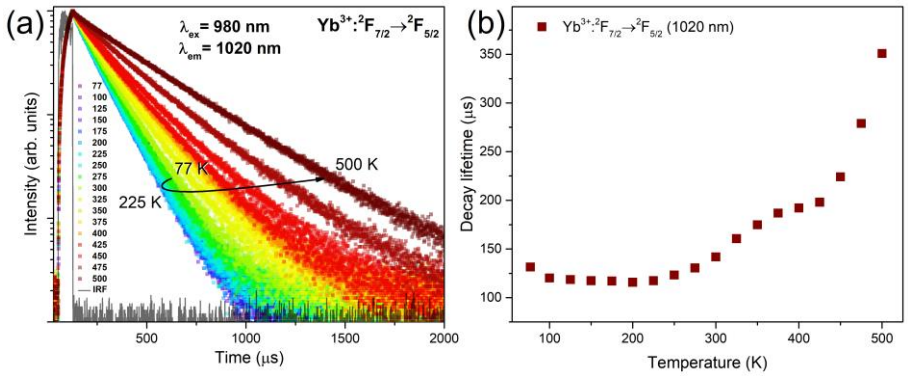

Figure 8.6 (a) Temperature-dependent down-conversion luminescence (DCL) decay curves of Yb^{3+}: $^2F_{5/2}$ excited state (λ_{em} = 1020 nm) and (b) calculated average lifetimes of $NaYbF_4:Er^{3+}$ microparticles.

The Yb^{3+} DCL lifetimes at 1020 nm in $NaYbF_4:Er^{3+}$ UCMPs increase gradually with raising the temperature from 225 to 500 K (Fig. 8.6 a). Contrarily to previously obtained Er^{3+} kinetic curves, the decays of Yb^{3+} were fitted with a bi-exponential equation (*Eq. 7.1*). The reasonable explanation could be that the appearance of bi-exponential decay profile comes from the emission of the Yb^{3+} ions at different local environments. The shorter decay component (τ_1) is usually assigned to the Yb^{3+} atoms located closer to the surface of the $NaYbF_4:Er^{3+}$ microparticles and thus it follows a faster decay process due to the surface induced quenching (i.e. solvent, defects). The longer decay component (τ_2) is attributed to the emission of Yb^{3+} ions located in the bulk phase of the microparticles [101]. As shown in Fig. 8.6 b, the lifetime of Yb^{3+} excited state $^2F_{5/2}$ exhibits a significant increase from 116 to 343 μs as temperature goes from 225 to 500 K. The detailed calculations of the lifetimes are given in Table 8.2, where the average lifetime value (τ_{avg}) is calculated by following equation:

$$\tau_{average} = \tau_1 \times R_1 + \tau_2 \times R_2 \qquad (Eq.\ 8.2)$$

The prolonging of Yb^{3+} lifetimes could be associated with thermal alleviation of energy migration-mediated surface quenching as described in Ji *et al.* work [169]. Commonly, the higher temperature induces increase of the non-radiative multi-phonon relaxation, leading to a reduced excited state lifetime [170], which is controversial to our measurements. However, satisfactory explanation of this controversy requires a more detailed experimental data.

Table 8.2 Fitted lifetimes τ_i, relative ratio factor R_i and coefficient values (χ^2) of the $^2F_{5/2}$ (λ_{em} = 1020 nm) level of Yb^{3+} at different temperatures (77-500 K).

Temperature, K	1020 nm					
	τ_1, µs	R_1	τ_2, µs	R_2	χ^2	τ_{avg}, µs
77	73.37	0.145	141.31	0.855	1.063	131.48
100	73.87	0.202	131.96	0.798	1.109	120.21
125	72.50	0.200	130.09	0.780	1.033	118.55
150	66.13	0.158	127.10	0.842	1.021	117.48
175	70.38	0.182	127.35	0.818	1.048	116.96
200	66.57	0.164	125.44	0.836	1.034	115.82
225	72.88	0.195	128.23	0.805	1.048	117.43
250	72.31	0.169	133.62	0.831	1.001	123.26
275	76.70	0.162	140.91	0.838	1.021	130.53
300	85.05	0.207	156.76	0.793	1.037	141.90
325	91.33	0.187	176.58	0.813	1.017	160.68
350	99.67	0.221	196.26	0.779	0.998	174.91
375	98.98	0.183	206.52	0.817	0.996	186.84
400	105.36	0.207	214.69	0.793	1.001	192.09
425	108.81	0.221	223.35	0.779	1.004	198.04
450	128.72	0.248	255.57	0.752	1.075	224.10
475	170.81	0.231	311.37	0.769	1.006	278.94
500	201.26	0.095	366.62	0.905	1.038	350.89

8.4 Influence of Input Excitation Power on Upconversion Dynamics

In order to understand the mechanisms involved in the UC process, the pump power-dependent UC emission spectra were recorded. It reveals that the UC luminescence intensity decreases with the pump power, as depicted in Fig. 8.7. As known, for an unsaturated UC process, the relation between the UC emission intensity and the laser pump power can be written as [171]:

$$I_{UP} \infty P^n \qquad (Eq.\ 8.3)$$

In this expression, I_{UC} is the UC emission intensity, P is the laser pump power and n is the number of photons that are required to populate the upper excited state level. According to the fitting results (Fig. 8.7 inset), the n values for the $^2H_{11/2} \rightarrow {}^4I_{15/2}$, $^4S_{3/2} \rightarrow {}^4I_{15/2}$ and $^4F_{9/2} \rightarrow {}^4I_{15/2}$ transitions were determined to be 1.33, 1.35 and 1.34, respectively. The obtained n values reveal that both green and red UC emission is a result of more than one-photon absorption process.

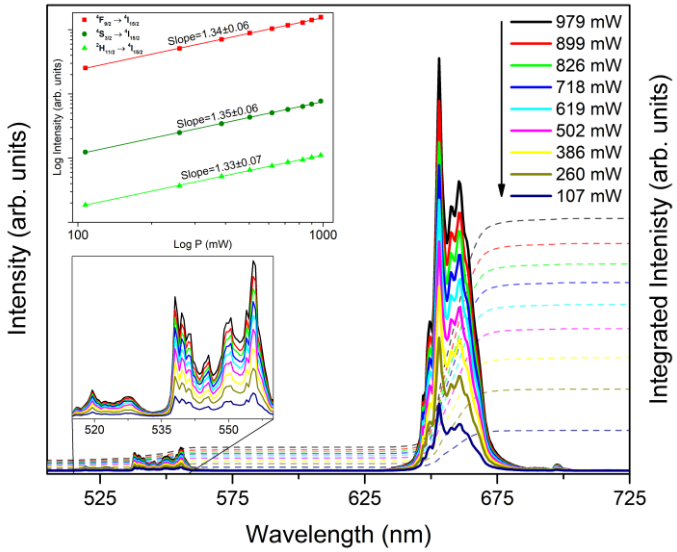

Figure 8.7 Room temperature UC emission spectra of $NaYbF_4:Er^{3+}$ as a function of pump power. Inset on the left top represents the dependence of two green and red UC emission intensities on pump power; inset on the left bottom shows a close-up of green UC emission.

8.5 Chromaticity of $NaYbF_4:Er^{3+}$

From the recorded upconversion spectra of the $NaYbF_4:Er^{3+}$ (Fig. 8.3) we calculated the Commission International de I′Eclairage (CIE) coordinates as a function of temperature. The exact calculated values are given in Table 8.3. As shown in Fig. 8.8, an orange colour perception with coordinates of (0.516, 0.472) was obtained at a low temperature (77 K), and the colour coordinates moved toward the pure green region (0.420, 0.554) following elevating the temperature to 500 K. The results demonstrate that the output colour of $NaYbF_4:Er^{3+}$ can be adjusted by the temperature.

Table 8.3 Chromaticity coordinates (*x*, *y*) of the $NaYbF_4:Er^{3+}$ microparticles under 980 nm laser excitation at different temperatures.

Temperature, K	Chromaticity coordinate (*x*)	Chromaticity coordinate (*y*)
77	0.516	0.472
100	0.509	0.481
125	0.501	0.489
150	0.494	0.496
175	0.485	0.505
200	0.475	0.515
225	0.466	0.523
250	0.460	0.528
275	0.452	0.535
300	0.454	0.533
325	0.453	0.533
350	0.449	0.535
375	0.440	0.541
400	0.431	0.549
425	0.422	0.556
450	0.419	0.558
475	0.421	0.554
500	0.420	0.554

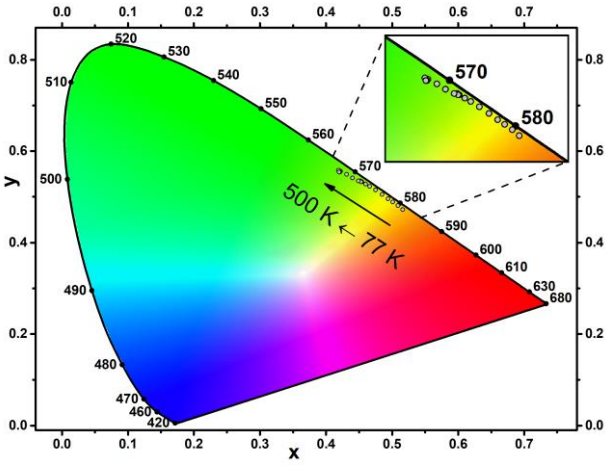

Figure 8.8 CIE 1931 colour space diagram with colour coordinates of $NaYbF_4:Er^{3+}$ microparticles at different temperatures. Inset shows a close-up of output colour shift area.

8.6 UC Luminescence for Temperature Sensing

Temperature-dependent optical properties have potential in applications for temperature sensing and anti-counterfeiting [16, 17]. Er^{3+} ions possess relatively narrow (~700 cm^{-1}) energy gap between the $^2H_{11/2}$ and $^4S_{3/2}$ levels, thus the lower energy $^4S_{3/2}$ state could easily thermally populate the higher $^2H_{11/2}$ state. Therefore, both excited states are in thermal equilibrium and the relative population follows the Boltzmann distribution, as emission intensities will vary as a function of temperature. The potential for thermometry applications is associated with fluorescence intensity ratio (FIR) and can be evaluated using the equation (*Eq. 7.2*). Fig. 8.9 a present normalized green upconversion emission spectra measured in the temperature range from 175 to 475 K under 980 nm laser excitation. The fluorescence intensities of $^2H_{11/2} \rightarrow {}^4I_{15/2}$ and $^4S_{3/2} \rightarrow {}^4I_{15/2}$ transitions were integrated from 505.0 nm to 534.0 nm and from 534.0 nm to 570.0 nm, respectively. The dependence of FIR on absolute temperature for $NaYbF_4$:1%Er^{3+} sample, which is shown in Fig. 8.9 b, can be well fitted with an exponential function:

$$Ln(FIR) = 2.21 - \frac{1059.69}{T} \qquad (Eq.\ 8.4)$$

The effective energy difference (ΔE) obtained from the fitting is 736 cm^{-1}, which matches the splitting of 700–800 cm^{-1} between $^2H_{11/2}$ and $^4S_{3/2}$ multiplets. The relative temperature sensitivity (S_R) is described as relative change of the FIR value with respect to temperature variation and is commonly used as a parameter for direct comparison of different FIR-based optical temperature sensors [109]. S_R can be mathematically expressed as (*Eq. 7.4*). As shown in Fig. 8.10, in the examined temperature range the S_R value decreases from 3.46 to 0.5 $\%\cdot K^{-1}$ (S_R=1060/T^2), which is rather promising in comparison with other Er^{3+} doped materials presented in similar studies (Table 8.4). These results imply that the UCMPs could be employed as highly sensitive temperature sensors based on the FIR technique.

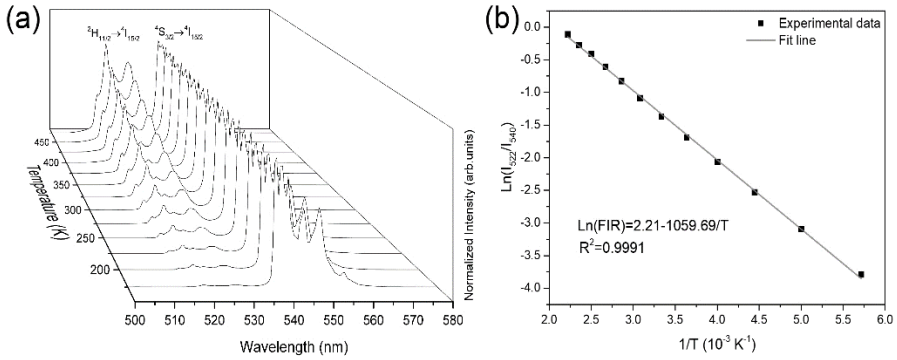

Figure 8.9 (a) $NaYbF_4$:1%Er^{3+} temperature-dependent green UC luminescence spectra normalized to 538.5 nm, under 980 nm laser excitation; (b) FIR data versus absolute temperature.

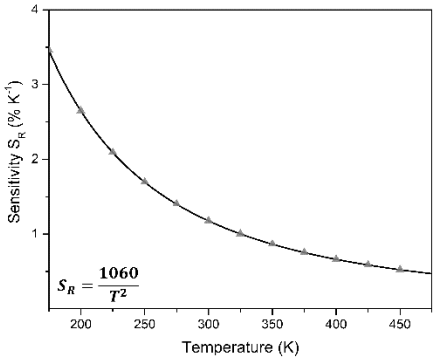

Figure 8.10 Plot of the relative sensitivity S_R as a function of temperature in the range of 175-475 K for $NaYbF_4$:1%Er^{3+} microparticles.

Table 8.4 Sensing materials, temperature range, maximum S_R value and corresponding temperature T (K) of several typical FIR-based optical temperature sensors based on upconversion emission from $^2H_{11/2}$ and $^4S_{3/2}$ levels of Er^{3+} ion.

Sensing materials	**Temperature range (K)**	S_R **(%K^{-1})**	T **(K)**	**Ref.**
$NaYF_4$:Yb^{3+},Er^{3+} *MPs*	75-600	0.48	515	[172]
$NaBiF_4$:Yb^{3+},Er^{3+} *NPs*	303-483	1.24	303	[173]
KYb_2F_7:Er^{3+} *glass ceramics*	300-480	0.45	590	[174]
$NaYF_4$:Yb^{3+},Er^{3+} *NPs*	288-328	1.37	288	[168]
$NaErF_4$@$NaYF_4$@$NaYbF_4$:Tm@$NaYF_4$ *NPs*	293-413	0.71	315	[167]
$NaYF_4$:Yb^{3+},Er^{3+}@$NaYF_4$:Yb^{3+},Nd^{3+} *NPs*	200-450	2.00	200	[175]
$NaYF_4$:Er^{3+},Yb^{3+} *NPs*	173-350	3.58	173	[176]
$LiLaP_4O_{12}$:Yb^{3+},Er^{3+} *NPs*	173-350	1.80	200	[176]
$NaYbF_4$:Er^{3+} *MPs*	175-475	3.46	175	This work

8.7 UCMPs Printing

The thermochromic features might significantly contribute to the properties of security markers [177]. Upconversion luminescence temperature-responsive colour shifting could be achieved by excitation with 980 nm laser. As shown in Fig. 8.11, the symbol “Er” painted on paper exhibits orange emission at room temperature (Fig. 8.11 b), and output colour shifts to green upon increasing the temperature to ~400 K (Fig. 8.11 c). Multicolour shifting of Er^{3+}-activated UCMPs could be simply achieved by exposing them to commercially available laser and colour response can be easily recognized by naked eye for visual authentication. Temperature-responsive luminescent marker with properties mentioned above may provide strengthened security for anti-counterfeiting applications.

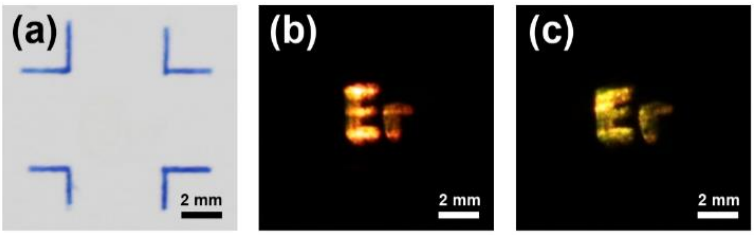

Figure 8.11 Digital photographs of painted symbol "Er" with colourless $NaYbF_4:Er^{3+}$ UCMPs ink: (a) without artificial irradiation, (b) at room temperature and (c) at higher temperature (~400 K) under 980 nm laser excitation.

8.8 Review of the Main Results

In this chapter, the hexagonal phase Er^{3+}-activated $NaYbF_4$ microparticles were synthesized *via* thermal decomposition method. The temperature-dependent UC luminescence and dynamics properties were investigated. Following the increase of temperature, the integrated UC emission intensity decreased, but an unexpected enhancement of luminescence lifetimes for all the emission bands was observed. Moreover, the temperature sensing properties based on the FIR technique from the thermally coupled $^2H_{11/2}$ and $^4S_{3/2}$ levels of Er^{3+} ions were studied. It was found that $NaYbF_4$:1%Er^{3+} microparticles can be operated in the temperature range of 175-475 K with a maximum relative sensor sensitivity of 3.46 %·K^{-1} at 175 K. These findings have great potential in developing luminescent materials with unique temperature-related performance, such as temperature sensing and anti-counterfeiting applications.

Chapter 9. Conclusions

1. The thermal decomposition method was adapted for synthesis of $NaGdF_4$:Yb,Er, $NaGdF_4$:Er, $NaYbF_4$, $NaGdF_4$:Yb,Er@$NaGdF_4$, $NaGdF_4$:Er@$NaYbF_4$, and $NaGdF_4$:Er@$NaYbF_4$@$NaGdF_4$ particles. The SEM analysis showed that the obtained nanoparticles were spherical in shape with average diameter of approximately 10 nm, 20 nm and 27 nm for core, core-shell and core-shell-shell samples, respectively. In the case of $NaYbF_4$:Er synthesis, the as-prepared particles were hexagonal microplates with average diameter of ~360 nm and height up to 130 nm.
2. The hydrophobic core and core–shell, as well as core-shell-shell nanoparticles were converted into hydrophilic ones using a non-ionic surfactant Tween 80. The FTIR data of UCNPs@Tween80 was highly comparable with that of pure Tween 80, indicating that the Tween 80 has successfully coated the UCNPs surface.
3. It was determined that the integrated emission intensity of $^4S_{3/2} \rightarrow {}^4I_{15/2}$ transition (λ_{em} = 540 nm) of the core–shell $NaGdF_4$:Yb,Er@$NaGdF_4$ nanoparticles is two magnitudes higher than the core-only $NaGdF_4$:Yb,Er UCNPs.
4. It was observed that the T1-weighted magnetic resonance (MR) imaging signal intensity has enhanced approximately 3.5-fold for $NaGdF_4$:Yb,Er and $NaGdF_4$:Yb,Er@$NaGdF_4$ UCNPs samples when compared to the water.
5. The influence of separation of activator and sensitizer in different layers and inert-shell coating on optical properties was investigated. It was found that $NaGdF_4$:Er@$NaYbF_4$ core-shell NPs have shorter lifetime value (173.6 μs) than $NaGdF_4$:Er core-only (290.0 μs) and $NaGdF_4$:Er@$NaYbF_4$@$NaGdF_4$ core-shell-shell (260.1 μs) samples. The observed prolonged decay lifetimes of core-shell-shell samples are compared to those of core-shell indicate that growing an inert shell on the core-shell NPs significantly increases the average lifetimes. Also, it was determined that the optimal Er^{3+} concentration in the core of $NaGdF_4$:Er@$NaYbF_4$@$NaGdF_4$ NPs is 3 %.
6. It was observed that the double shell coating greatly enhances the upconversion luminesce. In comparison with $NaGdF_4$:Er^{3+} core-only NPs, the obtained enhancement factor of total integrated emission

intensity is ~300 times stronger for core-shell-shell NPs. Moreover, an extraordinary 914-fold red emission (λ_{em} = 653.5 nm) enhancement in $NaGdF_4$:Er@$NaYbF_4$@$NaGdF_4$ NPs was obtained.

7. The temperature-dependent upconversion luminescence and corresponding decay dynamics of $NaYbF_4$:1%Er^{3+} microparticles were systematically investigated. Following the increase of temperature, the integrated UC emission intensity decreased, but an unexpected enhancement of luminescence lifetimes for all the emission bands was observed.
8. The temperature-sensing properties based on fluorescence intensity ratio technique of $NaGdF_4$:3%Er@$NaYbF_4$@$NaGdF_4$ core-shell-shell NPs and $NaYbF_4$:1%Er^{3+} MPs were determined. In the case of core-shell-shell NPs, the results showed that in the physiological temperature range (~ 300 K) relative temperature sensitivity (S_R) has a promising value of 0.99 %·K^{-1}. Also, it was demonstrated that the $NaYbF_4$:1%Er^{3+} microparticles can be operated as ratiometric fluorescence thermometers in the temperature range of 175-475 K with a maximum relative sensitivity of 3.46 %·K^{-1} at 175 K.
9. Upconversion luminescence temperature-responsive colour shifting of $NaYbF_4$:Er^{3+} microparticles containing ink was observed under the excitation with 980 nm laser. It was showed that the symbol painted on paper with UCMPs ink exhibited orange emission at room temperature and output colour shifted to green upon increasing the temperature to ~400 K.
10. The *in vitro* uptake and cytotoxicity evaluation study showed that the core-shell and core-shell-shell UCNPs internalized into breast cancer cell lines and possessed low cytotoxicity and good biocompatibility. All these findings indicate that Tween 80-coated UCNPs are a promising nanomaterial platform for imaging and detection in oncology.

Chapter 10. List of Publications and Conference Participation

10.1 Publications Included in the Thesis

10.1.1 Articles in Journals

1. **D. Baziulyte-Paulaviciene**, V. Karabanovas, M. Stasys, G. Jarockyte, V. Poderys, S. Sakirzanovas and R. Rotomskis. "*Synthesis and functionalization of $NaGdF_4$:Yb,Er@$NaGdF_4$ core–shell nanoparticles for possible application as multimodal contrast agents*". Beilstein J. Nanotechnol. 2017, 8, 1815–1824. DOI: 10.3762/bjnano.8.183
2. **D. Baziulyte-Paulaviciene**, N. Traskina, R. Vargalis, A. Katelnikovas, S. Sakirzanovas. "*Thermal decomposition synthesis of Er^{3+}-activated $NaYbF_4$ upconverting microparticles for optical temperature sensing*". J. Luminescence, 2019, 215, 116672. DOI: 10.1016/j.jlumin.2019.116672
3. **D. Baziulyte-Paulaviciene**, N. Traskina, R. Vargalis, A. Katelnikovas, G. Jarockyte, V. Karabanovas, R. Rotomskis, S. Sakirzanovas. "*Optical properties study of core-shell-shell nanoparticles with different Er^{3+} activator concentration and their application for thermal sensing and bioimaging*". Beilstein J. Nanotechnol. 2019 (submitted manuscript).

10.2 Attended Conferences

10.2.1 Oral Presentations

1. **D. Baziulyte**, V. Karabanovas, I. Jurčiukonis, S. Šakirzanovas. Upconversion Core-shell Nanoparticles with Enhanced Photoluminescence for Application in Bioimaging and Cancer Therapy. Open Readings, 2016, Vilnius, Lithuania.

10.2.2 Poster Presentations

2. **D. Baziulyte**, S. Šakirzanovas. Surface modification and characterization of $NaGdF_4$:Yb,Er upconverting nanoparticles. Current Trends of Cancer Theranostics, 2015, Jena, Germany.
3. **D. Baziulyte**, R. Rotomskis, S. Sakirzanovas. Surface modification and characterization of $NaGdF_4$:Yb,Er upconverting nanoparticles.. Advanced materials and technologies, 2015, Palanga, Lithuania.
4. **D. Baziulytė**, V. Karabanovas, I. Jurčiukonis, S. Šakirzanovas. Synthesis and Characterization of Surfactant-stabilized $NaGdF_4$:Yb,Er@$NaGdF_4$ Core-shell Upconversion Nanoparticles. Nanochemistry and Nanomaterials, 2015, Vilnius, Lithuania.
5. **D. Baziulyte**, M. Stasys, V. Karabanovas, R. Rotomskis, S. Sakirzanovas. Enhanced Red Emission in Water Soluble $NaGdF_4$:Yb,Er@$NaYbF_4$@$NaGdF_4$ Core-shell-shell Upconverting Nanoparticles. Advanced materials and technologies, 2016, Palanga, Lithuania.
6. **D. Baziulytė**, V. Karabanovas, M. Stalnionis, I. Jurčiukonis, S. Šakirzanovas. Upconvertion Core-shell Nanoparticles with Enhanced Photoluminescence for Application in Bioimaging and Cancer Therapy. Chemistry&Chemical Technology, 2016, Vilnius, Lithuania.
7. **D. Baziulyte**, M. Stasys, V. Karabanovas, R. Rotomskis, S. Sakirzanovas. Synthesis and Surface Modification of $NaGdF_4$:Yb,Er@$NaYbF_4$@$NaGdF_4$ Core–Shell–Shell Upconverting Nanoparticles. Current Trends of Cancer Theranostics, 2016, Druskininkai, Lithuania. (***Gold poster award***)
8. L. Karpus, **D. Baziulyte**, I. Mikalauskaite, M. Stalnionis, G. Jarockyte, V. Poderys, S. Sakirzanovas, A. Beganskiene, G. Streckyte, R. Rotomskis, V. Karabanovas. Water-soluble multimodal core/shell $NaGdF_4$:Yb,Er@$NaGdF_4$ upconverting nanoparticles for cancer diagnostics. Nanotechnology in Biology & Medicine, 2016, Krems, Austria.
9. L. Karpus, **D. Baziulytė**, S. Šakirzanovas, V. Karabanovas, R. Rotomskis. Optical Properties of $NaGdF_4$:Yb,Er@$NaGdF_4$

Upconverting Nanoparticles and Their Application in Cancer Diagnosis. Open readings, 2016, Vilnius, Lithuania.

10. E. Daugėlaitė, M. Stašys, **D. Baziulytė**, R. Rotomskis. Upconvertion Nanoparticles in Magnetic Resonance Imaging. Open readings, 2016, Vilnius, Lithuania.
11. **D. Baziulyte-Paulaviciene**, R. Rotomskis, V. Karabanovas, S. Sakirzanovas. Upconverting Nanoparticles for Theranostic. Open Readings, 2017, Vilnius, Lithuania.
12. A. Vilkas, **D. Baziulyte-Paulaviciene**, S. Sakirzanovas, V. Karabanovas, R. Rotomskis. Upconverting nanoparticles optical properties dependence on size and shell. Open Readings, 2017, Vilnius, Lithuania.
13. **D. Baziulyte-Paulaviciene**, G. Jarockyte, V. Karabanovas, R. Rotomskis, S. Sakirzanovas. Synthesis and upconversion luminescence properties of biocompatible core/shell/shell nanoparticles with enhanced red emission for application in bioimaging. Current Trends of Cancer Theranostics, 2017, Pakruojis, Lithuania.
14. **D. Baziulyte-Paulaviciene**, G. Jarockyte, R. Rotomskis, V. Karabanovas, S. Sakirzanovas. Biocompatible upconverting core/shell/shell nanoparticles with enhanced red emission for application in bioimaging and cancer therapy. Nanomedicine and Nanobiotechnology, 2017, Barcelona, Spain.
15. A. Vilkas, **D. Baziulyte-Paulaviciene**, S. Sakirzanovas, V. Karabanovas, R. Rotomskis. Investigations of $NaGdF_4:Yb^{3+}$, Er^{3+} nanoparticles excited state lifetimes dependence on particles core size and shell thickness. Lietuvos Nacionalinė Fizikų Konferencija, 2017, Vilnius, Lithuania.
16. S. Varapnickas, **D. Baziulytė-Paulavičienė**, S. Šakirzanovas, M. Malinauskas. $NaYbF_4:Er^{3+}$ as luminescent temperature probes for local heating imaging during direct laser writing nanolithography. Lietuvos Nacionalinė Fizikų Konferencija, 2017, Vilnius, Lithuania.
17. S. Varapnickas, **D. Baziulyte-Paulaviciene**, S. Šakirzanovas, M. Malinauskas. Upconverting nanocrystals as luminescent temperature probes for local-heating imaging during direct laser writing 3D nanolithography. SPIE Nanophotonics Australasia, 2017, Melbourne, Australia.

18. S. Varapnickas, **D. Baziulyte-Paulaviciene**, L. Jonušauskas, S. Sakirzanovas, M. Malinauskas. Local temperature measurement during ultrafast laser 3D nanolithography writing. SPIE LASE, 2018, San Francisco, California, United States.
19. **D. Baziulyte-Paulaviciene**, G. Jarockyte, R. Rotomskis, V. Karabanovas, S. Varapnickas, M. Malinauskas, S. Sakirzanovas. Synthesis of core-shell upconverting nanoparticles, their characterization and application. Open readings, 2018, Vilnius, Lithuania.
20. **D. Baziulyte-Paulaviciene**, G. Jarockyte, R. Rotomskis, V. Karabanovas, S. Varapnickas, M. Malinauskas, S. Sakirzanovas. Core-shell Upconverting Nanoparticles: Synthesis, characterization and application. UPCON18: 2nd Conference and Spring School on Properties, Design and Applications of Upconversion Nanomaterials, 2018, Valencia, Spain.
21. K. Kristinaityte, S. Dragunas, S. Sakirzanovas, **D. Baziulyte-Paulaviciene**, L. Dagys, R. Rotomskis, N. Valeviciene, V. Balevicius. NMR relaxation rates and diffusion processes in aqueous solutions of Gd (III) ion doped upconversion nanoparticles. European Magnetic Resonance Meeting EUROMAR, 2018, Nantes, France.
22. **D. Baziulyte-Paulaviciene**, G. Jarockyte, R. Rotomskis, V. Karabanovas, S. Sakirzanovas. Multifunctional Inorganic Fluoride Core-shell Upconverting Nanoparticles as Theranostic Agent. Current Trends of Cancer Theranostics, 2018, Trakai, Lithuania.
23. S. Varapnickas, J. B. Queiroz, **D. Baziulytė-Paulavičienė**, S. Šakirzanovas, M. Malinauskas. In-situ Optical Temperature Measurement in Micro-Scale during Ultrafast Laser 3D Nanolithography. CLEO/Europe-EQEC, 2019, Munich, Germany.

10.3 Publications Not Included in the Thesis

10.3.1 Articles in Journals

1. K. Kristinaityte, T. Zalewski, M. Kempka, S, Sakirzanovas, **D. Baziulyte-Paulaviciene**, S. Jurga, R. Rotomskis, N. R. Valeviciene. “Spin–Lattice Relaxation and Diffusion Processes in Aqueous Solutions of Gadolinium-Based Upconverting Nanoparticles at Different Magnetic Fields”. Appl. Magn. Resonance, 2019, 50: 553.

10.3.2 Conference Proceedings

1. S. Varapnickas, **D. Baziulyte-Paulaviciene**, S. Šakirzanovas, M. Malinauskas. “Upconverting nanocrystals as luminescent temperature probes for local-heating imaging during direct laser writing 3D nanolithography“, Proc. SPIE 10456, Nanophotonics Australasia (2018).
2. S. Varapnickas, **D. Baziulyte-Paulaviciene**, L. Jonušauskas, S. Sakirzanovas, M. Malinauskas. "Local temperature measurement during ultrafast laser 3D nanolithography writing", Proc. SPIE 10520, Laser-based Micro- and Nanoprocessing XII (2018).

REFERENCES

[1] F. Zhang, Photon Upconversion Nanomaterials, Springer, Berlin, Heidelberg, 2015.
[2] M. Haase, H. Schäfer, Upconverting Nanoparticles, Angew. Chem., Int. Ed., 50 (2011) 5808-5829.
[3] M. Pollnau, D.R. Gamelin, S.R. Lüthi, H.U. Güdel, M.P. Hehlen, Power dependence of upconversion luminescence in lanthanide and transition-metal-ion systems, Phys. Rev. B, 61 (2000) 3337-3346.
[4] B. Zhou, B. Shi, D. Jin, X. Liu, Controlling upconversion nanocrystals for emerging applications, Nat. Nanotechnol., 10 (2015) 924.
[5] H.S. Mader, P. Kele, S.M. Saleh, O.S. Wolfbeis, Upconverting luminescent nanoparticles for use in bioconjugation and bioimaging, Curr. Opin. Chem. Biol., 14 (2010) 582-596.
[6] E. Hemmer, P. Acosta-Mora, J. Méndez-Ramos, S. Fischer, Optical nanoprobes for biomedical applications: shining a light on upconverting and near-infrared emitting nanoparticles for imaging, thermal sensing, and photodynamic therapy, J. Mater. Chem. B, 5 (2017) 4365-4392.
[7] J. Zhou, Z. Liu, F. Li, Upconversion nanophosphors for small-animal imaging, Chem. Soc. Rev., 41 (2012) 1323-1349.
[8] B. del Rosal, D. Jaque, Upconversion nanoparticles for in vivo applications: limitations and future perspectives, Methods Appl. Fluoresc., 7 (2019) 022001.
[9] G. Chen, H. Qiu, P.N. Prasad, X. Chen, Upconversion Nanoparticles: Design, Nanochemistry, and Applications in Theranostics, Chem. Rev., 114 (2014) 5161-5214.
[10] A. Skripka, V. Karabanovas, G. Jarockyte, R. Marin, V. Tam, M. Cerruti, R. Rotomskis, F. Vetrone, Decoupling Theranostics with Rare Earth Doped Nanoparticles, Adv. Funct. Mater., 29 (2019) 1807105.
[11] X. Chen, D. Peng, Q. Ju, F. Wang, Photon upconversion in core–shell nanoparticles, Chem. Soc. Rev., 44 (2015) 1318-1330.
[12] S. He, N.J.J. Johnson, V.A. Nguyen Huu, E. Cory, Y. Huang, R.L. Sah, J.V. Jokerst, A. Almutairi, Simultaneous Enhancement of Photoluminescence, MRI Relaxivity, and CT Contrast by Tuning the Interfacial Layer of Lanthanide Heteroepitaxial Nanoparticles, Nano Lett., 17 (2017) 4873-4880.
[13] N.J.J. Johnson, S. He, S. Diao, E.M. Chan, H. Dai, A. Almutairi, Direct Evidence for Coupled Surface and Concentration Quenching Dynamics in Lanthanide-Doped Nanocrystals, J. Am. Chem. Soc., 139 (2017) 3275-3282.
[14] S. Wen, J. Zhou, K. Zheng, A. Bednarkiewicz, X. Liu, D. Jin, Advances in highly doped upconversion nanoparticles, Nat. Commun., 9 (2018) 2415.
[15] Y. Fan, L. Liu, F. Zhang, Exploiting lanthanide-doped upconversion nanoparticles with core/shell structures, Nano Today, 25 (2019) 68-84.

[16] P. Kumar, S. Singh, B.K. Gupta, Future prospects of luminescent nanomaterial based security inks: from synthesis to anti-counterfeiting applications, Nanoscale, 8 (2016) 14297-14340.
[17] C.D.S. Brites, S. Balabhadra, L.D. Carlos, Lanthanide-Based Thermometers: At the Cutting-Edge of Luminescence Thermometry, Adv. Opt. Mater., 7 (2019) 1801239.
[18] F. Wang, Y. Han, C.S. Lim, Y. Lu, J. Wang, J. Xu, H. Chen, C. Zhang, M. Hong, X. Liu, Simultaneous phase and size control of upconversion nanocrystals through lanthanide doping, Nature, 463 (2010) 1061.
[19] L.H. Fischer, G.S. Harms, O.S. Wolfbeis, Upconverting Nanoparticles for Nanoscale Thermometry, Angew. Chem., Int. Ed., 50 (2011) 4546-4551.
[20] C.D.S. Brites, P.P. Lima, N.J.O. Silva, A. Millán, V.S. Amaral, F. Palacio, L.D. Carlos, Thermometry at the nanoscale, Nanoscale, 4 (2012) 4799-4829.
[21] D. Jaque, F. Vetrone, Luminescence nanothermometry, Nanoscale, 4 (2012) 4301-4326.
[22] J.M. Meruga, A. Baride, W. Cross, J.J. Kellar, P.S. May, Red-green-blue printing using luminescence-upconversion inks, J. Mater. Chem. C, 2 (2014) 2221-2227.
[23] N. Bloembergen, Solid State Infrared Quantum Counters, Phys. Rev. Lett., 2 (1959) 84-85.
[24] F. Auzel, C. R. Acad. Sci. Paris, B262 (1966) 1016-1019.
[25] F. Wang, X. Liu, Recent advances in the chemistry of lanthanide-doped upconversion nanocrystals, Chem. Soc. Rev., 38 (2009) 976-989.
[26] H. Dong, L.-D. Sun, C.-H. Yan, Energy transfer in lanthanide upconversion studies for extended optical applications, Chem. Soc. Rev., 44 (2015) 1608-1634.
[27] Z. Wang, A. Meijerink, Concentration Quenching in Upconversion Nanocrystals, J. Phys. Chem. C, 122 (2018) 26298-26306.
[28] J. Zhou, Q. Liu, W. Feng, Y. Sun, F. Li, Upconversion Luminescent Materials: Advances and Applications, Chem. Rev., 115 (2015) 395-465.
[29] G. Tessitore, G.A. Mandl, M.G. Brik, W. Park, J.A. Capobianco, Recent insights into upconverting nanoparticles: spectroscopy, modeling, and routes to improved luminescence, Nanoscale, 11 (2019) 12015-12029.
[30] Z. Zhang, S. Shikha, J. Liu, J. Zhang, Q. Mei, Y. Zhang, Upconversion Nanoprobes: Recent Advances in Sensing Applications, Anal. Chem., 91 (2019) 548-568.
[31] D. Vennerberg, Z. Lin, Upconversion Nanocrystals: Synthesis, Properties, Assembly and Applications, Sci. Adv. Mat., 3 (2011) 26-40.
[32] S. Fischer, R.D. Mehlenbacher, A. Lay, C. Siefe, A.P. Alivisatos, J.A. Dionne, Small Alkaline-Earth-based Core/Shell Nanoparticles for Efficient Upconversion, Nano Lett., 19 (2019) 3878-3885.

[33] M. Kaiser, C. Würth, M. Kraft, T. Soukka, U. Resch-Genger, Explaining the influence of dopant concentration and excitation power density on the luminescence and brightness of β-NaYF4:Yb3+,Er3+ nanoparticles: Measurements and simulations, Nano Res., 12 (2019) 1871-1879.
[34] S. Wilhelm, Perspectives for Upconverting Nanoparticles, ACS Nano, 11 (2017) 10644-10653.
[35] C. Würth, M. Kaiser, S. Wilhelm, B. Grauel, T. Hirsch, U. Resch-Genger, Excitation power dependent population pathways and absolute quantum yields of upconversion nanoparticles in different solvents, Nanoscale, 9 (2017) 4283-4294.
[36] S. Wilhelm, M. Kaiser, C. Würth, J. Heiland, C. Carrillo-Carrion, V. Muhr, O.S. Wolfbeis, W.J. Parak, U. Resch-Genger, T. Hirsch, Water dispersible upconverting nanoparticles: effects of surface modification on their luminescence and colloidal stability, Nanoscale, 7 (2015) 1403-1410.
[37] C. Homann, L. Krukewitt, F. Frenzel, B. Grauel, C. Würth, U. Resch-Genger, M. Haase, NaYF4:Yb,Er/NaYF4 Core/Shell Nanocrystals with High Upconversion Luminescence Quantum Yield, Angew. Chem., Int. Ed., 57 (2018) 8765-8769.
[38] J. Zhao, D. Jin, E.P. Schartner, Y. Lu, Y. Liu, A.V. Zvyagin, L. Zhang, J.M. Dawes, P. Xi, J.A. Piper, E.M. Goldys, T.M. Monro, Single-nanocrystal sensitivity achieved by enhanced upconversion luminescence, Nat. Nanotechnol., 8 (2013) 729.
[39] M.D. Wisser, S. Fischer, C. Siefe, A.P. Alivisatos, A. Salleo, J.A. Dionne, Improving Quantum Yield of Upconverting Nanoparticles in Aqueous Media via Emission Sensitization, Nano Lett., 18 (2018) 2689-2695.
[40] J.-C.G. Bünzli, C. Piguet, Taking advantage of luminescent lanthanide ions, Chem. Soc. Rev., 34 (2005) 1048-1077.
[41] H. Liu, K. Huang, R.R. Valiev, Q. Zhan, Y. Zhang, H. Ågren, Photon Upconversion Kinetic Nanosystems and Their Optical Response, Laser Photonics Rev., 12 (2018) 1700144.
[42] J. Bergstrand, Q. Liu, B. Huang, X. Peng, C. Würth, U. Resch-Genger, Q. Zhan, J. Widengren, H. Ågren, H. Liu, On the decay time of upconversion luminescence, Nanoscale, 11 (2019) 4959-4969.
[43] H. Liu, M.K.G. Jayakumar, K. Huang, Z. Wang, X. Zheng, H. Ågren, Y. Zhang, Phase angle encoded upconversion luminescent nanocrystals for multiplexing applications, Nanoscale, 9 (2017) 1676-1686.
[44] J. Shan, M. Uddi, R. Wei, N. Yao, Y. Ju, The Hidden Effects of Particle Shape and Criteria for Evaluating the Upconversion Luminescence of the Lanthanide Doped Nanophosphors, J. Phys. Chem. C, 114 (2010) 2452-2461.
[45] J. Zhao, Z. Lu, Y. Yin, C. McRae, J.A. Piper, J.M. Dawes, D. Jin, E.M. Goldys, Upconversion luminescence with tunable lifetime in NaYF4:Yb,Er nanocrystals: role of nanocrystal size, Nanoscale, 5 (2013) 944-952.

[46] M. Kraft, C. Würth, V. Muhr, T. Hirsch, U. Resch-Genger, Particle-size-dependent upconversion luminescence of NaYF4: Yb, Er nanoparticles in organic solvents and water at different excitation power densities, Nano Res., 11 (2018) 6360-6374.
[47] C. Würth, S. Fischer, B. Grauel, A.P. Alivisatos, U. Resch-Genger, Quantum Yields, Surface Quenching, and Passivation Efficiency for Ultrasmall Core/Shell Upconverting Nanoparticles, J. Am. Chem. Soc., 140 (2018) 4922-4928.
[48] Y. Lu, J. Zhao, R. Zhang, Y. Liu, D. Liu, E.M. Goldys, X. Yang, P. Xi, A. Sunna, J. Lu, Y. Shi, R.C. Leif, Y. Huo, J. Shen, J.A. Piper, J.P. Robinson, D. Jin, Tunable lifetime multiplexing using luminescent nanocrystals, Nat. Photonics, 8 (2013) 32.
[49] L. Tu, J. Zuo, H. Zhang, Revisit of energy transfer upconversion luminescence dynamics—the role of energy migration, Sci. China Technol. Sci., 61 (2018) 1301-1308.
[50] M. Wang, G. Abbineni, A. Clevenger, C. Mao, S. Xu, Upconversion nanoparticles: synthesis, surface modification and biological applications, Nanomedicine, 7 (2011) 710-729.
[51] A. Aebischer, M. Hostettler, J. Hauser, K. Krämer, T. Weber, H.U. Güdel, H.-B. Bürgi, Structural and Spectroscopic Characterization of Active Sites in a Family of Light-Emitting Sodium Lanthanide Tetrafluorides, Angew. Chem., Int. Ed., 45 (2006) 2802-2806.
[52] J.F. Suyver, J. Grimm, K.W. Krämer, H.U. Güdel, Highly efficient near-infrared to visible up-conversion process in NaYF4:Er3+,Yb3+, J. Lumin., 114 (2005) 53-59.
[53] J.-C. Boyer, F. Vetrone, L.A. Cuccia, J.A. Capobianco, Synthesis of Colloidal Upconverting $NaYF_4$ Nanocrystals Doped with Er^{3+}, Yb^{3+} and Tm^{3+}, Yb^{3+} via Thermal Decomposition of Lanthanide Trifluoroacetate Precursors, J. Am. Chem. Soc., 128 (2006) 7444-7445.
[54] H.-X. Mai, Y.-W. Zhang, L.-D. Sun, C.-H. Yan, Size- and Phase-Controlled Synthesis of Monodisperse $NaYF_4$:Yb,Er Nanocrystals from a Unique Delayed Nucleation Pathway Monitored with Upconversion Spectroscopy, J. Phys. Chem. C, 111 (2007) 13730-13739.
[55] S. Heer, K. Kömpe, H.U. Güdel, M. Haase, Highly Efficient Multicolour Upconversion Emission in Transparent Colloids of Lanthanide-Doped NaYF4 Nanocrystals, Adv. Mater., 16 (2004) 2102-2105.
[56] A. Nadort, J. Zhao, E.M. Goldys, Lanthanide upconversion luminescence at the nanoscale: fundamentals and optical properties, Nanoscale, 8 (2016) 13099-13130.
[57] R. Withnall, J. Silver, Physics of Light Emission from Rare-Earth Doped Phosphors, in: J. Chen, W. Cranton, M. Fihn (Eds.) Handbook of Visual Display Technology, Springer Berlin Heidelberg, Berlin, Heidelberg, 2012, pp. 1019-1028.

[58] A. Yin, Y. Zhang, L. Sun, C. Yan, Colloidal synthesis and blue based multicolor upconversion emissions of size and composition controlled monodisperse hexagonal NaYF4 : Yb,Tm nanocrystals, Nanoscale, 2 (2010) 953-959.
[59] X. Peng, B. Huang, R. Pu, H. Liu, T. Zhang, J. Widengren, Q. Zhan, H. Ågren, Fast upconversion super-resolution microscopy with 10 μs per pixel dwell times, Nanoscale, 11 (2019) 1563-1569.
[60] X. Chen, L. Jin, W. Kong, T. Sun, W. Zhang, X. Liu, J. Fan, S.F. Yu, F. Wang, Confining energy migration in upconversion nanoparticles towards deep ultraviolet lasing, Nat. Commun., 7 (2016) 10304.
[61] T. Sun, R. Ma, X. Qiao, X. Fan, F. Wang, Shielding Upconversion by Surface Coating: A Study of the Emission Enhancement Factor, ChemPhysChem, 17 (2016) 766-770.
[62] H.J.M.A.A. Zijlmans, J. Bonnet, J. Burton, K. Kardos, T. Vail, R.S. Niedbala, H.J. Tanke, Detection of Cell and Tissue Surface Antigens Using Up-Converting Phosphors: A New Reporter Technology, Anal. Biochem., 267 (1999) 30-36.
[63] G. Yi, H. Lu, S. Zhao, Y. Ge, W. Yang, D. Chen, L.-H. Guo, Synthesis, Characterization, and Biological Application of Size-Controlled Nanocrystalline NaYF4:Yb,Er Infrared-to-Visible Up-Conversion Phosphors, Nano Lett., 4 (2004) 2191-2196.
[64] F. Zhang, Y. Wan, T. Yu, F. Zhang, Y. Shi, S. Xie, Y. Li, L. Xu, B. Tu, D. Zhao, Uniform Nanostructured Arrays of Sodium Rare-Earth Fluorides for Highly Efficient Multicolor Upconversion Luminescence, Angew. Chem., Int. Ed., 46 (2007) 7976-7979.
[65] N. Panov, R. Marin, E. Hemmer, Microwave-Assisted Solvothermal Synthesis of Upconverting and Downshifting Rare-Earth-Doped LiYF4 Microparticles, Inorg. Chem., 57 (2018) 14920-14929.
[66] F. Liu, X. He, L. Liu, H. You, H. Zhang, Z. Wang, Conjugation of NaGdF4 upconverting nanoparticles on silica nanospheres as contrast agents for multi-modality imaging, Biomaterials, 34 (2013) 5218-5225.
[67] T. Cao, T. Yang, Y. Gao, Y. Yang, H. Hu, F. Li, Water-soluble NaYF4:Yb/Er upconversion nanophosphors: Synthesis, characteristics and application in bioimaging, Inorg. Chem. Commun., 13 (2010) 392-394.
[68] Z. Chen, H. Chen, H. Hu, M. Yu, F. Li, Q. Zhang, Z. Zhou, T. Yi, C. Huang, Versatile Synthesis Strategy for Carboxylic Acid−functionalized Upconverting Nanophosphors as Biological Labels, J. Am. Chem. Soc., 130 (2008) 3023-3029.
[69] N. Bogdan, F. Vetrone, G.A. Ozin, J.A. Capobianco, Synthesis of Ligand-Free Colloidally Stable Water Dispersible Brightly Luminescent Lanthanide-Doped Upconverting Nanoparticles, Nano Lett., 11 (2011) 835-840.

[70] L. Cheng, K. Yang, S. Zhang, M. Shao, S. Lee, Z. Liu, Highly-sensitive multiplexed in vivo imaging using pegylated upconversion nanoparticles, Nano Res., 3 (2010) 722-732.
[71] L.Y. Ang, M.E. Lim, L.C. Ong, Y. Zhang, Applications of upconversion nanoparticles in imaging, detection and therapy, Nanomedicine, 6 (2011) 1273-1288.
[72] M.V. DaCosta, S. Doughan, Y. Han, U.J. Krull, Lanthanide upconversion nanoparticles and applications in bioassays and bioimaging: A review, Anal. Chim. Acta, 832 (2014) 1-33.
[73] Y.-W. Zhang, X. Sun, R. Si, L.-P. You, C.-H. Yan, Single-Crystalline and Monodisperse LaF_3 Triangular Nanoplates from a Single-Source Precursor, J. Am. Chem. Soc., 127 (2005) 3260-3261.
[74] P. Ramasamy, P. Manivasakan, J. Kim, Upconversion nanophosphors for solar cell applications, RSC Advances, 4 (2014) 34873-34895.
[75] C. Liu, H. Wang, X. Zhang, D. Chen, Morphology- and phase-controlled synthesis of monodisperse lanthanide-doped NaGdF4nanocrystals with multicolor photoluminescence, J. Mater. Chem., 19 (2009) 489-496.
[76] C. Liu, H. Wang, X. Li, D. Chen, Monodisperse, size-tunable and highly efficient β-NaYF4:Yb,Er(Tm) up-conversion luminescent nanospheres: controllable synthesis and their surface modifications, J. Mater. Chem., 19 (2009) 3546-3553.
[77] Z. Li, Y. Zhang, An efficient and user-friendly method for the synthesis of hexagonal-phase $NaYF_4$:Yb, Er/Tm nanocrystals with controllable shape and upconversion fluorescence, Nanotechnology, 19 (2008) 345606.
[78] H.S. Qian, H.C. Guo, P.C.-L. Ho, R. Mahendran, Y. Zhang, Mesoporous-Silica-Coated Up-Conversion Fluorescent Nanoparticles for Photodynamic Therapy, Small, 5 (2009) 2285-2290.
[79] H.-S. Qian, Y. Zhang, Synthesis of Hexagonal-Phase Core−Shell NaYF4 Nanocrystals with Tunable Upconversion Fluorescence, Langmuir, 24 (2008) 12123-12125.
[80] H.-X. Mai, Y.-W. Zhang, R. Si, Z.-G. Yan, L.-d. Sun, L.-P. You, C.-H. Yan, High-Quality Sodium Rare-Earth Fluoride Nanocrystals: Controlled Synthesis and Optical Properties, J. Am. Chem. Soc., 128 (2006) 6426-6436.
[81] L. Zi, D. Zhang, G. De, Self-assembly NaGdF4nanoparticles: phase controlled synthesis, morphology evolution, and upconversion luminescence properties, Mater. Res. Express, 3 (2016) 025009.
[82] N.J.J. Johnson, W. Oakden, G.J. Stanisz, R. Scott Prosser, F.C.J.M. van Veggel, Size-Tunable, Ultrasmall $NaGdF_4$ Nanoparticles: Insights into Their T1 MRI Contrast Enhancement, Chem. Mater., 23 (2011) 3714-3722.
[83] B. Zhou, L. Tao, Y.H. Tsang, W. Jin, Core–shell nanoarchitecture: a strategy to significantly enhance white-light upconversion of lanthanide-doped nanoparticles, J. Mater. Chem. C, 1 (2013) 4313-4318.

[84] M.M. Lezhnina, T. Jüstel, H. Kätker, D.U. Wiechert, U.H. Kynast, Efficient Luminescence from Rare-Earth Fluoride Nanoparticles with Optically Functional Shells, Adv. Funct. Mater., 16 (2006) 935-942.
[85] S. Fischer, J.K. Swabeck, A.P. Alivisatos, Controlled Isotropic and Anisotropic Shell Growth in β-NaLnF4 Nanocrystals Induced by Precursor Injection Rate, J. Am. Chem. Soc., 139 (2017) 12325-12332.
[86] X. Li, D. Shen, J. Yang, C. Yao, R. Che, F. Zhang, D. Zhao, Successive Layer-by-Layer Strategy for Multi-Shell Epitaxial Growth: Shell Thickness and Doping Position Dependence in Upconverting Optical Properties, Chem. Mater., 25 (2013) 106-112.
[87] F. Zhang, R. Che, X. Li, C. Yao, J. Yang, D. Shen, P. Hu, W. Li, D. Zhao, Direct Imaging the Upconversion Nanocrystal Core/Shell Structure at the Subnanometer Level: Shell Thickness Dependence in Upconverting Optical Properties, Nano Lett., 12 (2012) 2852-2858.
[88] F. Wang, R. Deng, X. Liu, Preparation of core-shell NaGdF4 nanoparticles doped with luminescent lanthanide ions to be used as upconversion-based probes, Nat. Protoc., 9 (2014) 1634.
[89] F. Wang, J. Wang, X. Liu, Direct Evidence of a Surface Quenching Effect on Size-Dependent Luminescence of Upconversion Nanoparticles, Angew. Chem., Int. Ed., 49 (2010) 7456-7460.
[90] H. Dong, L.-D. Sun, Y.-F. Wang, J. Ke, R. Si, J.-W. Xiao, G.-M. Lyu, S. Shi, C.-H. Yan, Efficient Tailoring of Upconversion Selectivity by Engineering Local Structure of Lanthanides in NaxREF3+x Nanocrystals, J. Am. Chem. Soc., 137 (2015) 6569-6576.
[91] F. Wang, R. Deng, J. Wang, Q. Wang, Y. Han, H. Zhu, X. Chen, X. Liu, Tuning upconversion through energy migration in core–shell nanoparticles, Nat. Mater., 10 (2011) 968.
[92] G.-S. Yi, G.-M. Chow, Water-Soluble NaYF4:Yb,Er(Tm)/NaYF4/Polymer Core/Shell/Shell Nanoparticles with Significant Enhancement of Upconversion Fluorescence, Chem. Mater., 19 (2007) 341-343.
[93] J.-C. Boyer, F.C.J.M. van Veggel, Absolute quantum yield measurements of colloidal NaYF4: Er3+, Yb3+ upconverting nanoparticles, Nanoscale, 2 (2010) 1417-1419.
[94] G. Chen, J. Shen, T.Y. Ohulchanskyy, N.J. Patel, A. Kutikov, Z. Li, J. Song, R.K. Pandey, H. Ågren, P.N. Prasad, G. Han, (α-NaYbF4:Tm3+)/CaF2 Core/Shell Nanoparticles with Efficient Near-Infrared to Near-Infrared Upconversion for High-Contrast Deep Tissue Bioimaging, ACS Nano, 6 (2012) 8280-8287.
[95] A. Punjabi, X. Wu, A. Tokatli-Apollon, M. El-Rifai, H. Lee, Y. Zhang, C. Wang, Z. Liu, E.M. Chan, C. Duan, G. Han, Amplifying the Red-Emission of Upconverting Nanoparticles for Biocompatible Clinically Used Prodrug-Induced Photodynamic Therapy, ACS Nano, 8 (2014) 10621-10630.

[96] J. Shen, G. Chen, T.Y. Ohulchanskyy, S.J. Kesseli, S. Buchholz, Z. Li, P.N. Prasad, G. Han, Tunable Near Infrared to Ultraviolet Upconversion Luminescence Enhancement in (α-NaYF4:Yb,Tm)/CaF2 Core/Shell Nanoparticles for In situ Real-time Recorded Biocompatible Photoactivation, Small, 9 (2013) 3213-3217.
[97] B. Shen, S. Cheng, Y. Gu, D. Ni, Y. Gao, Q. Su, W. Feng, F. Li, Revisiting the optimized doping ratio in core/shell nanostructured upconversion particles, Nanoscale, 9 (2017) 1964-1971.
[98] H. Qiu, C. Yang, W. Shao, J. Damasco, X. Wang, H. Ågren, P.N. Prasad, G. Chen, Enhanced Upconversion Luminescence in Yb3+/Tm3+-Codoped Fluoride Active Core/Active Shell/Inert Shell Nanoparticles through Directed Energy Migration, Nanomaterials, 4 (2014) 55-68.
[99] H. Guo, Z. Li, H. Qian, Y. Hu, I.N. Muhammad, Seed-mediated synthesis of NaY F4:Y b, Er/NaGdF4nanocrystals with improved upconversion fluorescence and MR relaxivity, Nanotechnology, 21 (2010) 125602.
[100] C. Dong, A. Korinek, B. Blasiak, B. Tomanek, F.C.J.M. van Veggel, Cation Exchange: A Facile Method To Make NaYF4:Yb,Tm-NaGdF4 Core–Shell Nanoparticles with a Thin, Tunable, and Uniform Shell, Chem. Mater., 24 (2012) 1297-1305.
[101] G. Chen, T.Y. Ohulchanskyy, W.C. Law, H. Ågren, P.N. Prasad, Monodisperse NaYbF4 : Tm3+/NaGdF4 core/shell nanocrystals with near-infrared to near-infrared upconversion photoluminescence and magnetic resonance properties, Nanoscale, 3 (2011) 2003-2008.
[102] G. Chen, H. Ågren, T.Y. Ohulchanskyy, P.N. Prasad, Light upconverting core–shell nanostructures: nanophotonic control for emerging applications, Chem. Soc. Rev., 44 (2015) 1680-1713.
[103] H. Liu, J. Xu, H. Wang, Y. Liu, Q. Ruan, Y. Wu, X. Liu, J.K.W. Yang, Tunable Resonator-Upconverted Emission (TRUE) Color Printing and Applications in Optical Security, Adv. Mater., 31 (2019) 1807900.
[104] B.J. Park, A.R. Hong, S. Park, K.-U. Kyung, K. Lee, H. Seong Jang, Flexible transparent displays based on core/shell upconversion nanophosphor-incorporated polymer waveguides, Sci. Reports, 7 (2017) 45659.
[105] R. Deng, F. Qin, R. Chen, W. Huang, M. Hong, X. Liu, Temporal full-colour tuning through non-steady-state upconversion, Nat. Nanotechnol., 10 (2015) 237.
[106] Y. Shang, S. Hao, C. Yang, G. Chen, Enhancing Solar Cell Efficiency Using Photon Upconversion Materials, Nanomaterials, 5 (2015) 1782-1809.
[107] G. Lee, Y.I. Park, Lanthanide-Doped Upconversion Nanocarriers for Drug and Gene Delivery, Nanomaterials, 8 (2018) 511.
[108] D.E. Achatz, R.J. Meier, L.H. Fischer, O.S. Wolfbeis, Luminescent Sensing of Oxygen Using a Quenchable Probe and Upconverting Nanoparticles, Angew. Chem., Int. Ed., 50 (2011) 260-263.

[109] C.D.S. Brites, P.P. Lima, N.J.O. Silva, A. Millán, V.S. Amaral, F. Palacio, L.D. Carlos, Lanthanide-based luminescent molecular thermometers, New J. Chem., 35 (2011) 1177-1183.
[110] F. Vetrone, R. Naccache, A. Zamarrón, A. Juarranz de la Fuente, F. Sanz-Rodríguez, L. Martinez Maestro, E. Martín Rodriguez, D. Jaque, J. García Solé, J.A. Capobianco, Temperature Sensing Using Fluorescent Nanothermometers, ACS Nano, 4 (2010) 3254-3258.
[111] D. Jaque, C. Richard, B. Viana, K. Soga, X. Liu, J. García Solé, Inorganic nanoparticles for optical bioimaging, Adv. Opt. Photon., 8 (2016) 1-103.
[112] D.K. Chatterjee, A.J. Rufaihah, Y. Zhang, Upconversion fluorescence imaging of cells and small animals using lanthanide doped nanocrystals, Biomaterials, 29 (2008) 937-943.
[113] L. Prodi, E. Rampazzo, F. Rastrelli, A. Speghini, N. Zaccheroni, Imaging agents based on lanthanide doped nanoparticles, Chem. Soc. Rev., 44 (2015) 4922-4952.
[114] G. Jalani, R. Naccache, D.H. Rosenzweig, L. Haglund, F. Vetrone, M. Cerruti, Photocleavable Hydrogel-Coated Upconverting Nanoparticles: A Multifunctional Theranostic Platform for NIR Imaging and On-Demand Macromolecular Delivery, J. Am. Chem. Soc., 138 (2016) 1078-1083.
[115] A. Baride, J.M. Meruga, C. Douma, D. Langerman, G. Crawford, J.J. Kellar, W.M. Cross, P.S. May, A NIR-to-NIR upconversion luminescence system for security printing applications, RSC Advances, 5 (2015) 101338-101346.
[116] Y. Huang, A. Skripka, L. Labrador-Páez, F. Sanz-Rodríguez, P. Haro-González, D. Jaque, F. Rosei, F. Vetrone, Upconverting nanocomposites with combined photothermal and photodynamic effects, Nanoscale, 10 (2018) 791-799.
[117] O.A. Savchuk, J.J. Carvajal, C. Cascales, J. Massons, M. Aguiló, F. Díaz, Thermochromic upconversion nanoparticles for visual temperature sensors with high thermal, spatial and temporal resolution, J. Mater. Chem. C, 4 (2016) 6602-6613.
[118] A. Skripka, A. Benayas, R. Marin, P. Canton, E. Hemmer, F. Vetrone, Double rare-earth nanothermometer in aqueous media: opening the third optical transparency window to temperature sensing, Nanoscale, 9 (2017) 3079-3085.
[119] S.A. Wade, S.F. Collins, G.W. Baxter, Fluorescence intensity ratio technique for optical fiber point temperature sensing, J. Appl. Phys., 94 (2003) 4743-4756.
[120] M. Runowski, A. Bartkowiak, M. Majewska, I.R. Martín, S. Lis, Upconverting lanthanide doped fluoride $NaLuF_4$:Yb^{3+}-Er^{3+}-Ho^{3+} - optical sensor for multi-range fluorescence intensity ratio (FIR) thermometry in visible and NIR regions, J. Lumin., 201 (2018) 104-109.

[121] L. Feng, B. Lai, J. Wang, G. Du, Q. Su, Spectroscopic properties of Er^{3+} in a oxyfluoride glass and upconversion and temperature sensor behaviour of Er^{3+}/Yb^{3+}-codoped oxyfluoride glass, J. Lumin., 130 (2010) 2418-2423.
[122] S.F. León-Luis, V. Monteseguro, U.R. Rodríguez-Mendoza, I.R. Martín, D. Alonso, J.M. Cáceres, V. Lavín, $2CaO{\cdot}Al_2O_3{:}Er^{3+}$ glass: An efficient optical temperature sensor, J. Lumin., 179 (2016) 272-279.
[123] P. Cortelletti, A. Skripka, C. Facciotti, M. Pedroni, G. Caputo, N. Pinna, M. Quintanilla, A. Benayas, F. Vetrone, A. Speghini, Tuning the sensitivity of lanthanide-activated NIR nanothermometers in the biological windows, Nanoscale, 10 (2018) 2568-2576.
[124] S. Zhou, K. Deng, X. Wei, G. Jiang, C. Duan, Y. Chen, M. Yin, Upconversion luminescence of NaYF4: Yb3+, Er3+ for temperature sensing, Optics Communications, 291 (2013) 138-142.
[125] E.D. Martínez, C.D.S. Brites, L.D. Carlos, R.R. Urbano, C. Rettori, Upconversion Nanocomposite Materials With Designed Thermal Response for Optoelectronic Devices, Front. Chem., 7 (2019).
[126] A. Sedlmeier, D.E. Achatz, L.H. Fischer, H.H. Gorris, O.S. Wolfbeis, Photon upconverting nanoparticles for luminescent sensing of temperature, Nanoscale, 4 (2012) 7090-7096.
[127] C.D.S. Brites, E.D. Martínez, R.R. Urbano, C. Rettori, L.D. Carlos, Self-Calibrated Double Luminescent Thermometers Through Upconverting Nanoparticles, Front. Chem., 7 (2019).
[128] J. Xu, A. Gulzar, P. Yang, H. Bi, D. Yang, S. Gai, F. He, J. Lin, B. Xing, D. Jin, Recent advances in near-infrared emitting lanthanide-doped nanoconstructs: Mechanism, design and application for bioimaging, Coord. Chem. Rev., 381 (2019) 104-134.
[129] B. del Rosal, I. Villa, D. Jaque, F. Sanz-Rodríguez, In vivo autofluorescence in the biological windows: the role of pigmentation, J. Biophotonics, 9 (2016) 1059-1067.
[130] B. del Rosal, B. Jia, D. Jaque, Beyond Phototherapy: Recent Advances in Multifunctional Fluorescent Nanoparticles for Light-Triggered Tumor Theranostics, Adv. Funct. Mater., 28 (2018) 1803733.
[131] M. Nyk, R. Kumar, T.Y. Ohulchanskyy, E.J. Bergey, P.N. Prasad, High Contrast in Vitro and in Vivo Photoluminescence Bioimaging Using Near Infrared to Near Infrared Up-Conversion in Tm3+ and Yb3+ Doped Fluoride Nanophosphors, Nano Lett., 8 (2008) 3834-3838.
[132] D. Ni, J. Zhang, W. Bu, H. Xing, F. Han, Q. Xiao, Z. Yao, F. Chen, Q. He, J. Liu, S. Zhang, W. Fan, L. Zhou, W. Peng, J. Shi, Dual-Targeting Upconversion Nanoprobes across the Blood–Brain Barrier for Magnetic Resonance/Fluorescence Imaging of Intracranial Glioblastoma, ACS Nano, 8 (2014) 1231-1242.
[133] J. Xu, F. He, Z. Cheng, R. Lv, Y. Dai, A. Gulzar, B. Liu, H. Bi, D. Yang, S. Gai, P. Yang, J. Lin, Yolk-Structured Upconversion Nanoparticles with

Biodegradable Silica Shell for FRET Sensing of Drug Release and Imaging-Guided Chemotherapy, Chem. Mater., 29 (2017) 7615-7628.
[134] Y.-F. Wang, G.-Y. Liu, L.-D. Sun, J.-W. Xiao, J.-C. Zhou, C.-H. Yan, Nd3+-Sensitized Upconversion Nanophosphors: Efficient In Vivo Bioimaging Probes with Minimized Heating Effect, ACS Nano, 7 (2013) 7200-7206.
[135] R. Kumar, M. Nyk, T.Y. Ohulchanskyy, C.A. Flask, P.N. Prasad, Combined Optical and MR Bioimaging Using Rare Earth Ion Doped NaYF4 Nanocrystals, Adv. Funct. Mater., 19 (2009) 853-859.
[136] J. Zhou, M. Yu, Y. Sun, X. Zhang, X. Zhu, Z. Wu, D. Wu, F. Li, Fluorine-18-labeled Gd3+/Yb3+/Er3+ co-doped NaYF4 nanophosphors for multimodality PET/MR/UCL imaging, Biomaterials, 32 (2011) 1148-1156.
[137] F. Chen, W. Bu, S. Zhang, X. Liu, J. Liu, H. Xing, Q. Xiao, L. Zhou, W. Peng, L. Wang, J. Shi, Positive and Negative Lattice Shielding Effects Co-existing in Gd (III) Ion Doped Bifunctional Upconversion Nanoprobes, Adv. Funct. Mater., 21 (2011) 4285-4294.
[138] Y. Sun, X. Zhu, J. Peng, F. Li, Core–Shell Lanthanide Upconversion Nanophosphors as Four-Modal Probes for Tumor Angiogenesis Imaging, ACS Nano, 7 (2013) 11290-11300.
[139] H.-T. Wong, M.-K. Tsang, C.-F. Chan, K.-L. Wong, B. Fei, J. Hao, In vitro cell imaging using multifunctional small sized KGdF4:Yb3+,Er3+ upconverting nanoparticles synthesized by a one-pot solvothermal process, Nanoscale, 5 (2013) 3465-3473.
[140] X. Yang, Q. Xiao, C. Niu, N. Jin, J. Ouyang, X. Xiao, D. He, Multifunctional core–shell upconversion nanoparticles for targeted tumor cells induced by near-infrared light, J. Mater. Chem. B, 1 (2013) 2757-2763.
[141] L. Xiong, T. Yang, Y. Yang, C. Xu, F. Li, Long-term in vivo biodistribution imaging and toxicity of polyacrylic acid-coated upconversion nanophosphors, Biomaterials, 31 (2010) 7078-7085.
[142] A. Gnach, T. Lipinski, A. Bednarkiewicz, J. Rybka, J.A. Capobianco, Upconverting nanoparticles: assessing the toxicity, Chem. Soc. Rev., 44 (2015) 1561-1584.
[143] L. Cheng, K. Yang, M. Shao, X. Lu, Z. Liu, In vivo pharmacokinetics, long-term biodistribution and toxicology study of functionalized upconversion nanoparticles in mice, Nanomedicine, 6 (2011) 1327-1340.
[144] L.-Q. Xiong, Z.-G. Chen, M.-X. Yu, F.-Y. Li, C. Liu, C.-H. Huang, Synthesis, characterization, and in vivo targeted imaging of amine-functionalized rare-earth up-converting nanophosphors, Biomaterials, 30 (2009) 5592-5600.
[145] J.M. Meruga, W.M. Cross, P. Stanley May, Q. Luu, G.A. Crawford, J.J. Kellar, Security printing of covert quick response codes using upconverting nanoparticle inks, Nanotechnology, 23 (2012) 395201.

[146] Y. Zhang, L. Zhang, R. Deng, J. Tian, Y. Zong, D. Jin, X. Liu, Multicolor Barcoding in a Single Upconversion Crystal, J. Am. Chem. Soc., 136 (2014) 4893-4896.
[147] Y. Liu, D. Tu, H. Zhu, R. Li, W. Luo, X. Chen, A Strategy to Achieve Efficient Dual-Mode Luminescence of Eu3+ in Lanthanides Doped Multifunctional NaGdF4 Nanocrystals, Adv. Mater., 22 (2010) 3266-3271.
[148] W. Ren, G. Tian, S. Jian, Z. Gu, L. Zhou, L. Yan, S. Jin, W. Yin, Y. Zhao, TWEEN coated NaYF4:Yb,Er/NaYF4 core/shell upconversion nanoparticles for bioimaging and drug delivery, RSC Advances, 2 (2012) 7037-7041.
[149] S. Park, N. Mohanty, J.W. Suk, A. Nagaraja, J. An, R.D. Piner, W. Cai, D.R. Dreyer, V. Berry, R.S. Ruoff, Biocompatible, Robust Free-Standing Paper Composed of a TWEEN/Graphene Composite, Adv. Mater., 22 (2010) 1736-1740.
[150] H.-T. Wong, F. Vetrone, R. Naccache, H.L.W. Chan, J. Hao, J.A. Capobianco, Water dispersible ultra-small multifunctional KGdF4:Tm3+, Yb3+ nanoparticles with near-infrared to near-infrared upconversion, J. Mater. Chem., 21 (2011) 16589-16596.
[151] Y. Hou, R. Qiao, F. Fang, X. Wang, C. Dong, K. Liu, C. Liu, Z. Liu, H. Lei, F. Wang, M. Gao, $NaGdF_4$ Nanoparticle-Based Molecular Probes for Magnetic Resonance Imaging of Intraperitoneal Tumor Xenografts in Vivo, ACS Nano, 7 (2013) 330-338.
[152] F. Vetrone, R. Naccache, A. Juarranz de la Fuente, F. Sanz-Rodríguez, A. Blazquez-Castro, E.M. Rodriguez, D. Jaque, J.G. Solé, J.A. Capobianco, Intracellular imaging of HeLa cells by non-functionalized NaYF4 : Er3+, Yb3+ upconverting nanoparticles, Nanoscale, 2 (2010) 495-498.
[153] V. Karabanovas, Z. Zitkus, D. Kuciauskas, R. Rotomskis, M. Valius, Surface Properties of Quantum Dots Define Their Cellular Endocytic Routes, Mitogenic Stimulation and Suppression of Cell Migration, J. Biomed. Nanotechnol., 10 (2014) 775-786.
[154] O. Osman, L.F. Zanini, M. Frénéa-Robin, F. Dumas-Bouchiat, N.M. Dempsey, G. Reyne, F. Buret, N. Haddour, Monitoring the endocytosis of magnetic nanoparticles by cells using permanent micro-flux sources, Biomed. Microdevices, 14 (2012) 947-954.
[155] S.-H. Wang, C.-W. Lee, A. Chiou, P.-K. Wei, Size-dependent endocytosis of gold nanoparticles studied by three-dimensional mapping of plasmonic scattering images, J. Nanobiotechnol., 8 (2010) 33.
[156] A. Woźniak, A. Noculak, J. Gapiński, D. Kociolek, A. Boś-Liedke, T. Zalewski, B.F. Grześkowiak, A. Kołodziejczak, S. Jurga, M. Banski, J. Misiewicz, A. Podhorodecki, Cytotoxicity and imaging studies of β-NaGdF4:Yb3+Er3+@PEG-Mo nanorods, RSC Advances, 6 (2016) 95633-95643.

[157] A.E. Guller, A.N. Generalova, E.V. Petersen, A.V. Nechaev, I.A. Trusova, N.N. Landyshev, A. Nadort, E.A. Grebenik, S.M. Deyev, A.B. Shekhter, A.V. Zvyagin, Cytotoxicity and non-specific cellular uptake of bare and surface-modified upconversion nanoparticles in human skin cells, Nano Res., 8 (2015) 1546-1562.
[158] J.A. Damasco, G. Chen, W. Shao, H. Ågren, H. Huang, W. Song, J.F. Lovell, P.N. Prasad, Size-Tunable and Monodisperse Tm3+/Gd3+-Doped Hexagonal NaYbF4 Nanoparticles with Engineered Efficient Near Infrared-to-Near Infrared Upconversion for In Vivo Imaging, ACS Appl. Mater. Interfaces, 6 (2014) 13884-13893.
[159] Z. Meng, S. Wu, S. Zhang, External current-controlled dynamic display by integrating upconversion micro-disks with power density-dependent color into NIR luminescent diodes, J. Mater. Chem. C, 6 (2018) 13101-13107.
[160] J. Xia, L. Lei, H. Xia, S. Xu, Improved negative thermal quenching effect via high sensitizer doping content in NaGdF4 based active-core/active-shell architecture, Opt. Commun., 444 (2019) 131-136.
[161] X. Dai, L. Lei, J. Xia, X. Han, Y. Hua, S. Xu, Effect of Yb^{3+} concentration and location on the thermally enhanced upconversion emission intensity of Yb/Ho: Na_3ZrF_7 nanocrystals, J. Alloys Compd., 766 (2018) 261-265.
[162] L. Lei, D. Chen, C. Li, F. Huang, J. Zhang, S. Xu, Inverse thermal quenching effect in lanthanide-doped upconversion nanocrystals for anti-counterfeiting, J. Mater. Chem. C, 6 (2018) 5427-5433.
[163] X. Cui, Y. Cheng, H. Lin, F. Huang, Q. Wu, Y. Wang, Size-dependent abnormal thermo-enhanced luminescence of ytterbium-doped nanoparticles, Nanoscale, 9 (2017) 13794-13799.
[164] L. Lei, J. Xia, Y. Cheng, Y. Wang, G. Bai, H. Xia, S. Xu, Enhancing negative thermal quenching effect via low-valence doping in two-dimensional confined core–shell upconversion nanocrystals, J. Mater. Chem. C, 6 (2018) 11587-11592.
[165] J. Zhou, S. Wen, J. Liao, C. Clarke, S.A. Tawfik, W. Ren, C. Mi, F. Wang, D. Jin, Activation of the surface dark-layer to enhance upconversion in a thermal field, Nat. Photonics, 12 (2018) 154-158.
[166] E. Hemmer, M. Quintanilla, F. Légaré, F. Vetrone, Temperature-Induced Energy Transfer in Dye-Conjugated Upconverting Nanoparticles: A New Candidate for Nanothermometry, Chem. Mater., 27 (2015) 235-244.
[167] L. Lei, X. Dai, Y. Cheng, Y. Wang, Z. Xiao, S. Xu, Dual-mode color tuning based on upconversion core/triple-shell nanostructure, J. Mater. Chem. C, 7 (2019) 3342-3350.
[168] D.T. Klier, M.U. Kumke, Upconversion $NaYF_4$:Yb:Er nanoparticles co-doped with Gd^{3+} and Nd^{3+} for thermometry on the nanoscale, RSC Advances, 5 (2015) 67149-67156.

[169] Z. Ji, Y. Cheng, X. Cui, H. Lin, J. Xu, Y. Wang, Heating-induced abnormal increase in Yb^{3+} excited state lifetime and its potential application in lifetime luminescence nanothermometry, Inorg. Chem. Front., 6 (2019) 110-116.
[170] L. Li, N. Zhao, L. Fu, J. Zhou, X. Ai, J. Zhang, Temperature modulation of concentration quenching in lanthanide-doped nanoparticles for enhanced upconversion luminescence, Nano Res., 11 (2018) 2104-2115.
[171] J.F. Suyver, J. Grimm, M.K. van Veen, D. Biner, K.W. Krämer, H.U. Güdel, Upconversion spectroscopy and properties of NaYF4 doped with Er3+, Tm3+ and/or Yb3+, Journal of Luminescence, 117 (2006) 1-12.
[172] L. Tong, X. Li, R. Hua, X. Li, H. Zheng, J. Sun, J. Zhang, L. Cheng, B. Chen, Comparative study on upconversion luminescence and temperature sensing of α- and β-$NaYF_4$:Yb^{3+}/Er^{3+} nano-/micro-crystals derived from a microwave-assisted hydrothermal route, J. Lumin., 167 (2015) 386-390.
[173] P. Du, L. Luo, X. Huang, J.S. Yu, Ultrafast synthesis of bifunctional Er^{3+}/Yb^{3+}-codoped $NaBiF_4$ upconverting nanoparticles for nanothermometer and optical heater, J. Colloid Interface Sci., 514 (2018) 172-181.
[174] J. Cao, F. Hu, L. Chen, H. Guo, C. Duan, M. Yin, Optical thermometry based on up-conversion luminescence behavior of Er3+-doped KYb2F7 nano-crystals in bulk glass ceramics, Journal of Alloys and Compounds, 693 (2017) 326-331.
[175] L. Marciniak, K. Prorok, L. Francés-Soriano, J. Pérez-Prieto, A. Bednarkiewicz, A broadening temperature sensitivity range with a core–shell YbEr@YbNd double ratiometric optical nanothermometer, Nanoscale, 8 (2016) 5037-5042.
[176] L. Marciniak, K. Prorok, A. Bednarkiewicz, Size dependent sensitivity of Yb^{3+},Er^{3+} up-converting luminescent nano-thermometers, J. Mater. Chem. C, 5 (2017) 7890-7897.
[177] Q. Shao, G. Zhang, L. Ouyang, Y. Hu, Y. Dong, J. Jiang, Emission color tuning of core/shell upconversion nanoparticles through modulation of laser power or temperature, Nanoscale, 9 (2017) 12132-12141.

ACKNOWLEDGEMENTS

First of all, I would like to express my deepest gratitude to my supervisor, Professor Simas Šakirzanovas, who was my mentor throughout this journey. I still remember how "green" I was when I started working in his lab, but thanks to him, now I feel much more confident in scientific research. His guidance and encouragement have been indispensable. Thank you for encouraging me to pursue my own ideas, as well as for the illuminating discussions, especially when I was confused and frustrated. Your support will never be forgotten.

I would like to express my thanks to Professor Ričardas Rotomskis, who suggested my thesis topic seven years ago. I am grateful for giving me the opportunity to start working in this fantastic field of luminescent materials, as well as your support and rewarding discussions throughout the period of this research.

Moreover, I would like to thank Professor Artūras Katelnikovas for assistance and guidance in luminescence measurements, as well as his help with writing manuscripts and data interpretation.

Also, I am grateful to all the group members from my lab for their help throughout the work. Especially I am sincere grateful to my dear friend Nadežda Traškina for her great support, motivation and most important for the help with the English language. Also, I want to thank Danas Sakalauskas and Rokas Vargalis, for their assistance with SEM measurements, as well as for fruitful discussions.

I would like to extend my gratitude to our various collaborators. I would like to acknowledge Dr. Vitalijus Karobanovas and Greta Jarockytė at Biomedical Physics Laboratory, National Cancer Institute for cellular measurements and contribution in writing manuscripts. Also, I would like to acknowledge Simonas Varapnickas and Dr. Mangirdas Malinauskas at faculty of Physics, Vilnius University for extending possibility to apply upconverting nanoparticles in 3D nanolithography.

I also thankful to the administrative staffs at CHGF. They are very helpful.

Finally, I would like to express my deepest gratitude to my beloved family and friends for their support and encouragement, and also for making life colourful and enjoyable. I wish to thank to my beloved husband, Giedrius Paulavičius, for your unconditional support, patience and love throughout this time.

NOTES

NOTES

NOTES

Vilniaus universiteto leidykla
Saulėtekio al. 9, LT-10222 Vilnius
El. p. info@leidykla.vu.lt,
www.leidykla.vu.lt
Tiražas 20 egz.